12-2018

Applications of Pionless EFT in Atomic and Nuclear Theory

Samuel Bryan Emmons
University of Tennessee, semmons@vols.utk.edu

To the Graduate Council:

I am submitting herewith a dissertation written by Samuel Bryan Emmons entitled "Applications of Pionless EFT in Atomic and Nuclear Theory." I have examined the final electronic copy of this dissertation for form and content and recommend that it be accepted in partial fulfillment of the requirements for the degree of Doctor of Philosophy, with a major in Physics.

Lucas Platter, Major Professor

We have read this dissertation and recommend its acceptance:

Katherine Grzywacz-Jones, Lawrence Heilbronn, Thomas Papenbrock

Accepted for the Council:

Dixie L. Thompson

Vice Provost and Dean of the Graduate School

(Original signatures are on file with official student records.)

Applications of Pionless EFT in Atomic and Nuclear Theory

A Dissertation Presented for the

Doctor of Philosophy

Degree

The University of Tennessee, Knoxville

Samuel Bryan Emmons

December 2018

Acknowledgments

First, thank you to my wife Sarah for your help and support throughout my time as a Ph. D. student. I also thank Dr. Daekyoung Kang for his friendship and his extensive participation and knowledge for the completion of the first two projects presented in this dissertation. It was truly a pleasure to have his collaboration. Dr. Bijaya Acharya was also instrumental in the completion of the second project and in the writing of the paper on that subject. Additionally, I would like to thank my advisor, Dr. Lucas Platter, for his assistance and guidance in all of the work presented in this dissertation. Further, the work on heteronuclear three-body recombination would have been much less interesting if Ruth Bloom had not provided us with her recombination data for the ^{40}K-^{87}Rb system.

Abstract

Effective Field Theory (EFT) is a useful approach in situations where the physical system in question exhibits a separation of scales that can be used to form a perturbative expansion in a ratio of elementary parameters of the system. In a low-energy EFT such as the so-called *pionless* EFT, such an expansion may be carried out in the ratio of the effective range to the scattering length. It is referred to as pionless EFT because of its origins in nuclear physics, where it is used to describe nuclear interactions with effective degrees of freedom without explicitly including the strong nuclear force, which is mediated by pion exchange. However, it may also be referred to as *short-range* EFT in non-nuclear contexts. In atomic physics, this theory is applicable when the scattering length between atoms is much larger than the underlying range of the interaction, such as in a cold atomic gas of ^{4}He. Nuclear physics applications range from describing the properties of weakly bound nuclei like deuterium to halo nuclei such as ^{11}Be. In this dissertation, we have applied pionless EFT to a homogeneous, balanced fermionic gas to determine universal relations that describe various parameters for any such system regardless of the short-range details of the underlying interaction. Additionally, we have studied a heteronuclear cold-atomic mixture and the interesting phenomena that occur when the interspecies scattering length is large compared to either the short range interaction distance, or any intraspecies scattering lengths. We calculated three-body recombination and relaxation rates at finite temperatures and compared our results with available experimental data. In nuclear physics, we have calculated the polarization corrections to the Lamb shift in muonic deuterium to next-to-leading order in the deuteron effective range, ρ_d. These examples comprise a small sample of the possible range of applications of pionless EFT, and another goal of this dissertation is to make accessible the basic principles of the theory for its further use.

Table of Contents

List of Tables

List of Figures

Chapter 1

Background

This document is intended to detail the work that I have completed as a Ph. D. student at the University of Tennessee, Knoxville, and it is also intended as a helpful tool for those interested in these topics and in the further use of the field theoretical methods explained herein. We have applied the pionless effective field theory ($\not\pi$EFT) to a selection of problems in low-energy atomic and nuclear physics.

1.1 Universality and Low Energy Scattering

In low-energy scattering processes, the quantum mechanical scattering length a is a fundamental parameter. It is the location at which a line matching the slope of the radial wavefunction of the scattered particle at the boundary of the interaction potential first crosses the r-axis in a plot of the radial wavefunction $\phi(r)$. This relates it to the scattering phase-shift, or the phase-angle by which the scattered wavefunction is shifted from a free wavefunction emanating from the origin. At very low energies, the two-body scattering amplitude is directly proportional to a, which means that the scattering cross section is proportional to πa^2. So, the scattering length may roughly be understood as the size of one particle from the perspective of another one incident upon it. This scattering length is often on the order of the interaction length scale ℓ. However, when $|a| \gg \ell$, the observable properties of the system at hand display behavior that is independent of the interaction potential [1]. This is described as universality since the formulas that describe one system

apply equally well to others that have a large scattering length. The deeper reasons why such a large scattering length arises are irrelevant for the purposes of calculating observables. Universality and its ramifications in two- and three-body physics phenomena have been described at length, for example, in Ref. [2].

Universality occurs in both the two- and three-body scattering and bound state sectors. In the two-body system, parameters such as the atom-atom scattering cross section may be expressed as a function of two-body energy E and a. Additionally, if $a > 0$, a shallow two-body bound state exists with binding energy $B = \hbar^2/ma^2$, and all other low-energy observables similarly depend only upon a. In the three-body scattering sector Vitaly Efimov discovered that there are unique universal properties when the two-body scattering length is large [3]. If $\ell \ll |a|$, these properties can be expressed in terms of a and one additional parameter. Determining this parameter requires the use of one three-body observable. The beauty of universality in three-body physics is that once one has determined the necessary parameter, one may use it to predict all other low-energy three-body observables [1].

Further, Efimov discovered [3] that when the two-body scattering length between any two of the three particles is larger than the length scale of the underlying interaction potential, there is a geometric sequence of three-body bound states that are shallowly bound compared to $\hbar^2/m\ell^2$. It is important to note that not all three-body systems meet such criterion. In the universal, or *unitary*, limit, where $a \to \pm\infty$, the sequence is infinite, and there are infinitely many three-body bound states to be found as you approach the three-particle threshold from below. The exact ratio, or scaling factor (squared scaling factor by convention), between these states changes depending on if the system is composed of identical bosons, fermions in three distinguishable states, or a heteronuclear system consisting of more than one particle species [4, 5]. One specific example of a system exhibiting universality in its observables is a gas of ^{4}He. The ^{4}He system is interesting because it is a case provided by nature wherein the scattering length is much larger than the underlying range of the interaction [1].

Additionally, if one includes a finite effective range in the problem, it is possible to introduce systematic corrections to universal results, as shown in Ref. [6]. The effective range is introduced in the low-energy expansion of $k \cot \delta$ in the two-body scattering amplitude and can be included perturbatively in an Effective Field Theory (EFT) approach. Additional

corrections can arise in heteronuclear systems in which both inter- and intraspecies scattering lengths are large. If the intraspecies scattering length, or the scattering length for two identical atoms in the heteronuclear mixture, is not too large it can be included perturbatively [7].

1.2 Pionless Effective Field Theory

Effective quantum field theories have become a standard tool for the description of the physics of strongly interacting systems in a nonperturbative regime. For such a theory, the most general possible Lagrangian consistent with the underlying physical symmetries is developed using quantum fields that create or annihilate the relevant degrees of freedom under consideration, such as quarks or atoms. These theories gain predictive power when they are expanded such that only a finite number of interaction terms is needed to aptly describe the physical system. In $\not\pi$EFT, an expansion in terms of $\ell/|a|$ serves this purpose [8, 9]. Each higher order in such an expansion contributes a portion to the total result of a given calculation that is smaller than the previous order's contribution by a factor of $\ell/|a|$. It is this EFT that we use throughout this work, and the degrees of freedom, or particles, allowed in the theory are numerous. When we apply $\not\pi$EFT to cold atomic physics, the quantum fields correspond to entire atoms, and individual electrons and nuclei do not enter the picture explicitly. In nuclear systems, we apply the theory to cases such as the deuteron, in which it is unnecessary to consider pion-exchange between nucleons. Instead, the physics is dominated by the nucleon-nucleon (NN) scattering length, which is several times larger than the range of the nuclear interaction potential. In this case, the quantum fields correspond to individual nucleons.

Pionless EFT is very general and, broadly speaking, allows for the calculation of various amplitudes for low-energy processes in which pions are not a necessary degree of freedom in the description of the physics. We prefer it for the systems considered here because the development of Feynman diagrams renders this approach visually and mathematically simpler than a purely quantum mechanical method, and external currents are straightforward to include. Additionally, the number of free parameters that must be fit to experimental data

is small at low orders in the EFT expansion, and the uncertainty of a calculation decreases as higher orders in the expansion are included. Beyond the applications of the theory we consider, it is widely applicable to systems consisting of bosons and/or fermions, so long as they fit the criterion already outlined above for physics at or near the universal limit. For example, in addition to atoms and light nuclei, $\not\pi$EFT has been applied to halo nuclei, in which the weakly bound nucleon and the core to which it is bound are the effective degrees of freedom with corresponding fields in the theory [10].

One issue from quantum field theory (QFT) that is also present in the EFT formalism we consider is that divergences arise in loop integrals over intermediate states. These divergences must be rendered finite to obtain physical results, and this is done via regularization of the integrals. Once the integrals are regulated, or made finite, a process known as renormalization [11] is carried out to match the theory onto a particular observable. It is at this point where the theory gains predictive power for other properties of whatever system is being considered. The most relevant regularization and renormalization methods for the work that follows utilize a finite momentum space cutoff (often denoted Λ in loop integrals) or dimensional regularization with either minimal subtraction a partial divergence subtraction (PDS) scheme [12]. In the two-body sector, when the scattering length is large compared to the range of the interaction, the EFT contact interaction becomes non-perturbative, and an ultraviolet divergence arises in the integral over the intermediate states. But, this cutoff dependence can be absorbed into the leading-order interaction coefficients themselves. The lack of detail about the short-distance physics in this low-energy theory is folded into these coefficients, or low-energy constants (LECs) [13].

1.3 Cold Fermionic Gases

Systems of strongly-interacting ultracold two-component fermions have been studied for many years. An example from nuclear physics is an ultracold gas of neutrons. In atomic physics, such a system is very interesting because as one crosses the unitary limit from large positive scattering lengths to large negative scattering lengths, the system transitions from a Bose-Einstein condensate (BEC) to a system displaying Bardeen-Cooper-Schrieffer (BCS)

superfluidity. Such systems in the unitary limit in particular have received a large amount of attention from the cold-atom physics community [14]. In this limit, one may apply the zero-range model, in which the range of the atom-atom interaction is taken to zero while the two-body binding energy is kept constant by adjustment of the coupling strength. The first topic we explore in this work applies ∉EFT in a cold atomic setting, specifically to a balanced, homogeneous gas of fermions in two spin states interacting strongly through a large scattering length.

Perhaps the most interesting theoretical development in recent years applicable to the cold-fermionic systems we consider was the introduction of universal relations by Shina Tan [15, 16, 17]. The expressions he first developed are remarkable in that they parameterize many of the bulk properties of the system in terms of the scattering length and a factor C referred to as the *contact*, which is a system-dependent measure of the average number of fermions that may be found at large momentum if the momentum distribution of the gas is measured. The methods used by Tan in his pioneering works involved rather complicated mathematical techniques in a quantum-mechanical framework.

We find that ∉EFT is very useful in this system, as is a field-theoretical tool called the *operator product expansion* (OPE). This field theory is useful because it is fully renormalizable when the effective range is zero, and order by order renormalizable when the range is included perturbatively. This makes it adept at handling the strongly interacting system of fermions with a large scattering length we consider and allows us to obtain physical results. And even with its own challenges, this field-theoretical approach is simpler than the methods used by Shina Tan in his 2008 works. The OPE, developed for the purpose of describing strongly interacting systems during the late 1960's by both Kenneth Wilson and Leo Kadanoff [18, 19], is the tool we use to develop the universal relations of Tan from a field theoretical perspective. It enables us to write the universal relations in terms of expectation values of interaction terms from the field-theoretical Lagrangian. The first work examining such systems using this approach is found in Refs. [20, 21]. These studies utilized the zero-range model as well as the *resonance model* [21], of which the *effective range model* is a special case. In each of these studies, including the work presented here, bulk properties of the gas

were derived from two-body interaction physics. This allows one to describe these cold-atomic many-body systems in a simpler manner than traditional many-body approaches. We have introduced corrections to universal relations describing a homogeneous, balanced gas of fermions in two spin states due to a finite effective range r_s in our work in Ref. [22], and the results are presented in this dissertation in Ch. 2.

1.4 The Efimov Effect in Heteronuclear Three-body Systems

When the scattering length between two particles is large, interesting physics is not confined to the two-body sector. For the system of two-component fermions interacting through a large scattering length considered above, two-body physics effects were dominant, and three-body interactions were not considered because of the Pauli exclusion principle. However, low-energy systems need not have this exclusive composition. Several types of systems displaying universal physics in the three-body scattering and bound-state sectors must also be considered, such as identical bosons, fermions in three distinguishable spin states, or heteronuclear mixtures of various bosonic and/or fermionic species. In ^{4}He, the scattering length is by nature much larger than the effective range r_s, and two universal three-body bound states are present [1]. But for systems with a still larger value of $|a|$, more trimers are allowed. The volume of the associated trimers is proportional to a^3, and the two bound state binding energies are separated by a factor which is the same for all systems of identical bosons displaying such universality.

In some cold-atomic systems that do not have a naturally small value of r_s/a, such as a gas of ^{87}Rb, the scattering length between two particles may be made large by tuning the magnetic field the gas resides in to a Feshbach resonance. These resonances are defined as the location of the magnetic field at which the magnitude of the scattering length diverges. Some literature demonstrating these resonances in systems of identical bosons is found in Refs. [23, 24, 25]. With a large two-body scattering length present in the three-body system, discrete scaling arises in which features in three-body observables take on a log-periodicity.

Bosonic systems all have the same value of the *scaling factor* associated with this discrete scaling, which we label λ. This number is a separation factor between universal features in various three-body observables, and the value is $\lambda_{\rm B} \approx 22.694$ for identical bosons.

One specific way of defining the scaling factor λ is as a spacing factor between binding-momentum values of universal three-body bound states. For example,

$$E^{(n)} = -\lambda^{2(n_*-n)} \frac{\kappa_*^2}{m}, \qquad n = n_*,\, n_* \pm 1,\, n_* \pm 2 \ldots . \tag{1.1}$$

Here, m has dimensions of mass and κ_* is a system-dependent three-body parameter which we obtain in our work from either experiments or ab-initio calculations. The three-body parameter in Eq. (1.1) is the binding momentum of a selected three-body bound state, but there are other parameters that may be used and fulfill the same purpose of matching our results onto results known from experiments.

The size of the scaling factor for identical bosons, $\lambda_{\rm B} \approx 22.694$, turns out to make it challenging to observe multiple Efimov features because of the change required in the external magnetic field the atoms are immersed in to alter the scattering length by this magnitude. This makes it difficult to test Efimov universality in an experimental system. Because of this, many have turned to heteronuclear mixtures consisting of two or more atomic species to study universal three-body physics. This is because in a gas with two distinguishable atomic species, the possibility still exists to make the interspecies scattering length large via a Feshbach resonance while keeping the intraspecies scattering length small, and the scaling factor is dependent upon the mass ratio of the two atomic species. This means that you can drive the scaling factor λ away from the bosonic scaling factor $\lambda_{\rm B} \approx 22.694$ and towards a smaller value which allows for the experimental viewing of additional Efimov features. A smaller scaling factor is nice because only a small change in the magnetic field is required to observe additional universal features in scattering-length-dependent observables.

One such interesting feature in systems which exhibit universal behavior is that, in the case of ultracold atomic gases, atoms are found to leave the trap through a process called three-body recombination. Experiments have confirmed this in systems of identical bosons [26, 27, 28, 29], and experiments and theory have also confirmed this in three distinguishable

states of fermionic ^{6}Li [30, 31, 32, 33, 34, 35, 36, 37]. This effect and the related event known as atom-dimer relaxation have also been looked for in heteronuclear systems [38], and this is the case which we study.

This dissertation contains an effective-field-theory analysis of the heteronuclear atomic system at finite temperature with an interspecies scattering length that is positive and large compared to all other length scales in the system. For the light atom we choose a fermionic species that has been prepared in one spin state, and the heavy species is bosonic. Experiments in a variety of systems demonstrate the applicability of these working assumptions. We explore the contributions from the first several higher-partial-wave (in orbital angular momentum) scattering channels to the three-body recombination rate and atom-dimer relaxation rate at finite temperatures for several systems.

One of the main messages from this work on universal physics in heteronuclear mixtures [5] was that, while highly mass-imbalanced systems have advantageously small scaling factors for the purposes of observing universal physics features, finite temperature effects largely obscure the otherwise more accessible universal physics, rendering these systems less desirable for the study of Efimov physics than previously thought. Much of the theoretical work our study is based on is contained in a 2008 paper by Eric Braaten, Hans-Werner Hammer, Daekyoung Kang, and Lucas Platter describing three-body physics in identical bosons [39]. It very much informed the approach taken here, in addition to papers by Helfrich, Hammer, and Petrov [40, 41].

1.5 Nuclear Polarization Corrections in Muonic Deuterium

As an electron or muon orbits a nucleus, it can excite the nucleus, and these excited nuclear states in turn affect the atomic states of the lepton-nucleus system. The resulting nuclear polarization corrections to the Lamb shift can be large and very difficult to calculate accurately. In this work, we have begun calculating these corrections in muonic deuterium in order to address their important impact on the measured finite size of the deuteron, which is

relevant to the *proton radius puzzle* and a range of measurements taken at institutions such as the Paul Scherrer Institute (PSI). The proton radius puzzle is highlighted in Ref. [42] and consists of the fact that, at present, disagreement larger than experimental uncertainties exists in the value of the proton radius extracted from experiments using electronic hydrogen versus the radius value taken from muonic hydrogen experiments. No satisfactory answer has been found to date that resolves this puzzle, though the proton radius calculated from a 2S-4P spectroscopic measurement in regular hydrogen by Axel Beyer *et al.* in Ref. [43] was found to be in agreement with the smaller value obtained from μ-p experiments. Yet, this does not fully resolve the puzzles, and more experimental and theoretical work is necessary to fully understand where the discrepancy arises in the bulk of other experimental data. Nuclei of larger atomic mass number have been examined to determine if the radius puzzle has any mass-number dependence. In the deuteron, the radius extracted from the 2S-2P Lamb shift in μ-D differs from that extracted in e-D by an amount larger than 2σ. One of the most recent experimental determinations of the deuteron charge radius was obtained by Randolph Pohl *et al.* from electronic deuterium spectroscopy in Ref. [44] is 3.5σ larger than the radius obtained with μ-D. This is an improvement over previous results in that the difference between muonic and electronic results is closer to being within 2σ. This discrepancy is referred to as the *deuteron radius puzzle* and is currently unresolved [45].

One of the most significant sources of theoretical uncertainty relevant to the extraction of the deuteron charge radius comes from the contribution due to two-photon exchange (TPE) between the orbiting lepton and the nucleus. This is the so-called *nuclear polarization correction* to the Lamb shift. This TPE energy correction is one component of the 2S-2P Lamb shift and must be derived from theory, since it is not separable from the other components of the energy shift in the experiments used to determine the Lamb shift. Other contributions to the Lamb shift come from quantum-electrodynamic (QED) effects and from the finite radius of the deuteron ground state. Thus, once the TPE and QED contributions to the Lamb shift are known from theoretical calculations, the deuteron charge radius may be extracted from the experimental data for the Lamb shift.

To approach the problem, we again utilize $\not$EFT, while including finite deuteron-effective-range corrections up to next-to-leading order. Within the theory, we include electromagnetic

interactions through minimal coupling in the Lagrangian density. Muonic deuterium lends itself well to this approach because the muon wave function does not change much across the physical volume of the nucleus and is approximately free. This enables the calculation of the polarization correction to the Lamb shift using the forward virtual Compton amplitude, which we then relate to the shift of the 2S energy state due to two-photon-exchange (TPE) between the muon and the nucleus. In the calculation of the forward virtual Compton amplitude, we follow the method of Refs. [46, 47] and replace it with the inelastic deuteron structure function. Further, we extract the component of the TPE energy shift due to inelastic electric dipole excitation of the nucleus, and the results compare favorably to those of Friar in Ref. [48]. This work is contained in Ch. 4.

1.6 Organization of this Work

Chapter 2 contains a detailed description of the work describing finite-effective-range-corrected universal relations in an ultracold two-component Fermi gas. Chapter 3 presents the details of our study about three-body recombination processes in heteronuclear atomic mixtures at finite temperatures. After this, Ch. 4 spells out progress made in the calculation of nuclear polarization corrections to the 2S-2P Lamb shift in μ-D. There are concluding remarks and discussion in Ch. 5.

Chapter 2

Balanced Two-Component Fermi Gases

In this chapter, we consider a homogeneous, balanced gas of fermions in two spin states interacting strongly through a large scattering length at low temperatures, of which various studies are ongoing [49, 50]. In order to move towards a more quantitative description of data that experiments and numerical simulations have provided, finite-interaction-range corrections must be included in the formalism. The most readily examined parts of the theory of such a system in our approach are known as universal relations. They are referred to as such because of their total lack of system dependence in the unitary, or $|a| \to \infty$, limit. Such universal relations were first derived in the zero-range limit by Shina Tan in 2005 [15, 16, 17] using a particular quantum-mechanical approach and apply to both few- and many-body systems at zero or non-zero temperatures. In the universal relations of those references, Tan introduced what has become known as the *contact*, C, defined by the large-momentum asymptote of the $1/k^4$ tail of the momentum distribution. Initially, this quantity was known as the *integrated contact intensity*. This is a state-dependent quantity that depends on such quantities as the scattering length, density, and temperature of the system. The leading-order expression for the large-momentum tail of the momentum distribution is an example of a universal relation involving Tan's contact:

$$\rho_\sigma(k) \to \frac{C}{k^4}\,, \tag{2.1}$$

where k is the magnitude of the relative momentum of two fermions interacting through a large scattering length. One additional example is the *adiabatic relation* giving the change in total energy E of the gas due to an adiabatic change in the scattering length. It is

$$\frac{dE}{da} = \frac{C}{4\pi m a^2}\,, \tag{2.2}$$

as seen in Refs. [17, 20], where additional universal relations are also studied in the zero-range limit.

The contact and related universal relations can also be derived in pionless EFT using a formal tool called the operator product expansion (OPE) [18, 19, 51], which is a quantum field-theoretical expansion of a nonlocal operator in a small spatial or time separation. It was first used to rederive Tan's universal relations and show that the contact is related to the leading two-body interaction term in the EFT in Ref. [20]. In this work, universal relations improved by the inclusion of the finite effective range of the two-body interaction are calculated. And just as the *contact* played an important role in the zero-range limit, two additional important quantities enter into the universal relations valid beyond the zero-range limit. One of these measures the sensitivity of the energy of the system to the effective range and is referred to as the *derivative contact*. The other new term gives a measure of the averaged kinetic energy of opposite-spin fermion pairs at zero relative distance. Of the universal relations we derived in this work, some were previously derived in a quantum-mechanical framework by Werner and Castin in Ref. [52]. In the zero-range limit, the OPE has also been applied to the problem previously [20, 21, 53]. In this work, we used the OPE in an EFT setting to derive additional universal relations including a finite interaction range perturbatively. This approach makes no assumptions regarding the microscopic details of the interaction which causes the large scattering length, so it is model independent.

The first portion of this chapter contains a review of the EFT used to describe the short-range interactions relevant to this work, as well as the renormalization of the theory using a hard momentum-space cutoff on the integrals over intermediate states up to next-to-leading order (NLO) in the EFT expansion in ℓ/a, where ℓ is the range of the atom-atom interaction and a is the two-body scattering length. Renormalization is often necessary in

field-theoretical approaches in order to eliminate divergences appearing in the calculations and obtain physical results. Following the presentation of the renormalization of the theory, we give the universal relations up to NLO in Sec. 2.2. That section also demonstrates how the renormalized two-body operators in the OPE form the contact and derivative contact operators of the presented universal relations. Next, Sec. 2.3 contains a numerical comparison between the field-theoretical results given here and provided Quantum Monte Carlo (QMC) data for the momentum distribution of the gas. This comparison is best made in the present case of two equally-populated spin states. Otherwise, the QMC method is complicated by the fermion sign problem. Finally, the detailed derivations of several universal relations are provided in Sec. 2.4. Integrals and definitions useful for the derivation of the following results are contained in Appendix A.

2.1 Effective Field Theory

The two-body t-matrix for a system of two fermions in opposite spin states interacting through a large scattering length a can be written as

$$t(k) = \frac{4\pi}{m} \frac{1}{k \cot \delta_0 - ik} \,, \tag{2.3}$$

where k is the relative momentum of the two interacting particles, m is the mass per particle (we assume the two particles are of equal mass), and the scattering phase shift is denoted δ_0. The subscript indicates total orbital angular momentum $L = 0$, or S-wave scattering.

This t-matrix may be expanded when k is smaller than the inverse of the interaction range R of the underlying potential, i.e. at low energies, using the effective range expansion. While one may expand about any k-value in the radius of convergence of the theory, such as the location of the deuteron binding momentum, the expansion about $k = 0$ is useful here and is given by

$$k \cot \delta_0 = -\frac{1}{a} + \frac{r_s}{2} k^2 + \cdots \,, \tag{2.4}$$

where a is the S-wave scattering length, and the S-wave effective range is denoted r_s and is $O(1/\Lambda)$ or smaller, where Λ is the momentum-space cutoff of the renormalization scheme

used in this work and $\Lambda \sim 1/R$. Systems with such properties can be described by an EFT in which particles interact only through contact interactions as long as the short-range details of the system are not resolved by the momentum scales in the system, i.e. when $k < 1/R$.

The Lagrangian for an EFT applicable to this system is given order-by-order as

$$\mathcal{L} = \mathcal{L}_0 + \mathcal{L}_1 + \cdots , \tag{2.5}$$

where $\mathcal{L}_{0,1}$ are the Lagrangians which are leading order (LO) and next-to-leading order (NLO) in the effective range r_s. The dots denote operators that contribute at higher orders in the EFT expansion and contain more derivatives and/or fields. The components of the Lagrangian that we are interested in are the LO and NLO terms. These are given by

$$\mathcal{L}_0 = \sum_{\sigma=1,2} \psi_\sigma^\dagger \left(i\partial_t + \frac{\nabla^2}{2m} \right) \psi_\sigma - \frac{\lambda_0}{m} \psi_1^\dagger \psi_2^\dagger \psi_2 \psi_1 \tag{2.6}$$

$$\mathcal{L}_1 = \frac{\rho_0}{4} \left(\psi_1^\dagger \psi_2^\dagger \psi_2 \overleftrightarrow{\nabla}^2 \psi_1 + \text{H.c.} \right) + \delta\mathcal{L}_1 , \tag{2.7}$$

$$\delta\mathcal{L}_1 = -\frac{\delta\lambda_0}{m} \psi_1^\dagger \psi_2^\dagger \psi_2 \psi_1 . \tag{2.8}$$

In these expressions, Planck's constant is set to $\hbar = 1$. The leading order Lagrangian given in Eq. (2.6) corresponds to the zero-range model [20]. The first term of that equation is the Lagrangian density for a free, non-relativistic particle, and the second is the LO interaction term with a bare coupling constant λ_0 related to the scattering length and the UV cutoff through renormalization. The term $\mathcal{L}_1$ consists of the effective-range term and contains ρ_0 and also $\delta\mathcal{L}_1$, which is present to subtract a divergence arising in the scattering amplitude calculation with this Lagrangian. This is a feature of the particular regularization scheme used in this chapter, in which all field-theoretic loop integrals are regulated using a finite UV cutoff. The LO and NLO expressions are renormalized below, and the coupling constants of the theory, λ_0, ρ_0 and counterterm $\delta\lambda_0$, are calculated in order to reproduce the LO and NLO t-matrix.

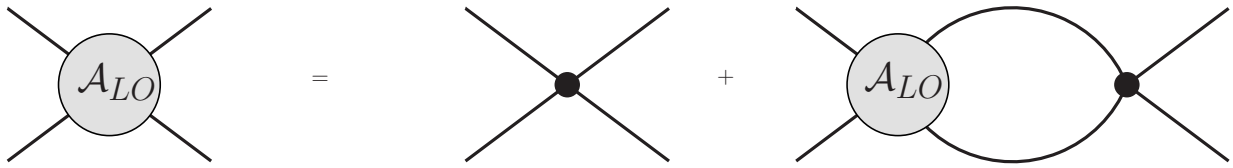

Fig. 2.1 – Leading order scattering amplitude.

2.1.1 Leading-order amplitude

The leading order vertex must be iterated to all orders in the expansion of the field-theoretical action $e^{-i\int dt\, H_I}$, where $H_I = -\int d^3\boldsymbol{R}\,\mathcal{L}_I(\boldsymbol{R})$, and the quantity $\boldsymbol{R}$ is in bold font to indicate that it is a vector quantity. This gives the nonperturbative properties of the system, which are LO in the effective range expansion [8, 9]. The diagrams whose sum gives the two-body scattering amplitude form an integral equation equivalent to the Lippmann–Schwinger (LS) equation,

$$i\mathcal{A}_{\rm LO}(E) = -i\frac{\lambda_0}{m} - i\frac{\lambda_0}{m}\mathcal{I}_0(E,\Lambda)i\mathcal{A}_{\rm LO}(E)\,, \tag{2.9}$$

where E is the total energy of the two-body system. The diagrams corresponding to Eq. (2.9) are given in Fig. 2.1 and come from iterating the non-perturbative contact interaction to all orders on the right-hand side (RHS) of the figure. $\mathcal{I}_0(E,\Lambda)$ is the loop integral in that figure and depends on the energy E and the ultraviolet cutoff Λ imposed on the integral. This integral in Eq. (2.9) is given in detail by Eq. (A.2) in Appendix A.

The low-energy constant (LEC) λ_0 depends on the cutoff and is determined by the requirement that Eq. (2.9) reproduces the t-matrix given in Eq. (2.3) in the zero-range limit. If we isolate the amplitude on one side of Eq. (2.9), the other side may be expressed as $-\frac{i\lambda_0}{m}/(1+\frac{i\lambda_0}{m}\mathcal{I}_0(E,\Lambda))$. This can also be obtained by iterating the interaction to all orders as described above and realizing that this sum must form a geometric series if it is to remain finite. In other words, we can rewrite the LO amplitude of Fig. 2.1 as

$$i\mathcal{A}_{\rm LO} = \sum_{j=0}^{\infty}\left(-\frac{i\lambda_0}{m}\right)^{j+1}\mathcal{I}_0^j(E,\Lambda) = -\frac{i\lambda_0}{m}\frac{1}{(1+\frac{i\lambda_0}{m}\mathcal{I}_0(E,\Lambda))}\,. \tag{2.10}$$

This expression for the amplitude in Eq. (2.10) may then be directly compared to the leading order amplitude of Eq. (2.3) with $k\cot\delta_0 = -1/a$ using the known form of $\mathcal{I}_0(E,\Lambda)$. In that

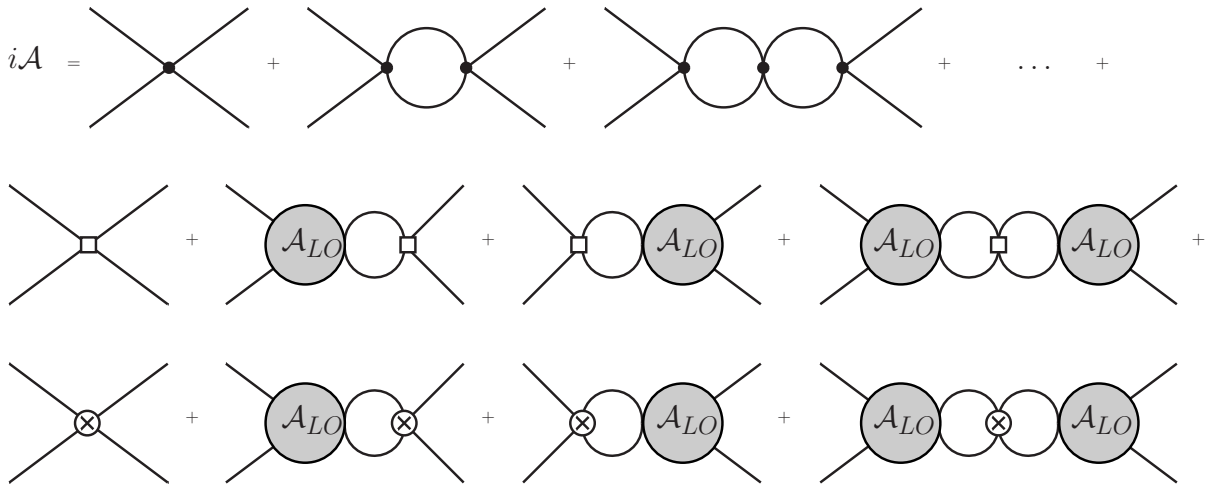

Fig. 2.2 – Scattering amplitude through NLO. Solid dots denote the λ_0 vertex, squares represent an insertion of the ρ_0 vertex, and the crossed circle vertices represent the counterterm vertex $\delta\lambda_0$.

comparison, λ_0 is the only unknown. Thus, we write it as an explicit function of Λ and scattering length a as

$$\lambda_0 = \frac{4\pi a}{1 - 2a\Lambda/\pi}\,. \tag{2.11}$$

2.1.2 Next-to-leading-order amplitude

In this section, we detail the renormalization of the EFT at NLO in the short-range interaction. Renormalization to this order was explained using a technique known as dimensional regularization with partial divergence subtraction (PDS), for example, in Ref. [8]. However, because we use an explicit momentum-space cutoff, an additional subtraction term is introduced below in addition to the NLO coupling constant ρ_0.

The NLO effective-range expansion of the t matrix of Eq. (2.3) is given by

$$t(k) = \frac{4\pi}{m}\frac{1}{-\frac{1}{a} + \frac{1}{2}r_s k^2 - ik} \approx \frac{4\pi}{m}\frac{1}{-\frac{1}{a} - ik}\left(1 - \frac{r_s k^2/2}{-\frac{1}{a} - ik} + O(r_s^2)\right)\,, \tag{2.12}$$

where the leading factor of 1 in parentheses of the final expression corresponds to the LO t-matrix and the second term is its NLO correction. Higher-order terms are encapsulated in $O(r_s^2)$. Note that this final expression in Eq. (2.12) is the result of expanding in a small finite effective range. The NLO part of this expression is reproduced below by a calculation

of the scattering amplitude with one perturbative insertion of the interaction Hamiltonian density given by $\mathcal{H}_1 = -\mathcal{L}_1$. This is simply the same procedure used in the LO case, only with the addition of the NLO vertex insertions.

Figure 2.2 shows the scattering amplitude up to NLO. The second row includes the sum of diagrams containing only one insertion of the ρ_0 vertex, and the third row of the figure gives the diagrams with one insertion of the $\delta\lambda_0$ vertex. The vertex factors present in the second and third lines of Fig. 2.2 are inserted only once because they are each directly proportional to the effective range r_s, which gives the desired form of the range contribution to the NLO t matrix. In addition to these two terms, the subleading part of the factor λ_0 on the order of $1/\Lambda \sim r_s$ arising from the chosen regularization method must also be included.

Summing all of the aforementioned contributions to the NLO scattering amplitude, we obtain

$$i\mathcal{A}_{\rm NLO} = -i\mathcal{A}_{\rm LO}^2 \frac{mk^2}{2\pi^2\Lambda} - i2\rho_0 \frac{m\mathcal{A}_{\rm LO}^2}{\lambda_0}\left(\frac{mk^2}{\lambda_0} - \frac{m\Lambda^3}{6\pi^2}\right) - i\frac{\delta\lambda_0}{m}\left(\frac{m\mathcal{A}_{\rm LO}}{\lambda_0}\right)^2 . \tag{2.13}$$

Each of the terms in Eq. (2.13) gives the NLO contribution from each of the three rows of diagrams in Fig. 2.2. The first comes from the first row of diagrams in the figure when we include only the NLO contribution proportional to k^2/Λ after summing over all diagrams in that row. The next contribution is the sum of diagrams containing a single effective-range vertex, and it contains a Λ^3 divergence. It is necessary that the term $\propto \delta\lambda_0$ subtracts the divergence of $O(\Lambda^3)$. Then, comparing Eq. (2.13) to the NLO part of Eq. (2.12), we calculate the constants ρ_0 and $\delta\lambda_0$ as

$$\rho_0 = \frac{\lambda_0^2}{16\pi m}\left(r_s - \frac{4}{\pi\Lambda}\right), \tag{2.14}$$

$$\delta\lambda_0 = \frac{(\lambda_0\Lambda)^3}{48\pi^3}\left(r_s - \frac{4}{\pi\Lambda}\right). \tag{2.15}$$

In Eq. (2.15), $\delta\lambda_0$ is a counterterm needed for proper renormalization. This is in distinction to the PDS renormalization scheme used in Chapter 4 below on polarization effects in the deuteron. In that case there is an NLO contribution to λ_0 (alternatively written mC_0) that is proportional to the deuteron effective range present in order to obtain the phase shift

expanded about the deuteron binding momentum γ, rather than to eliminate a spurious divergence from a loop integral.

2.2 Universal Relations at Next-to-Leading Order

In conjunction with the field-theoretical approach applied in this work, we use a tool called the operator product expansion (OPE) to calculate the momentum distribution of the system, as well as the contact C and the two new parameters associated with the NLO effective-range correction. The other universal relations addressed are then expressed in terms of expectation values of the operators associated with these three parameters. We present the detailed derivation of these universal relations in Sec. 2.4. In this section, universal relations including the $1/k^6$ correction to the $1/k^4$ tail of the momentum distribution and range corrections to the energy relation, adiabatic relation, pressure relation, and the virial theorem for a harmonic potential are given.

Through use of the OPE, we find the momentum distribution at momentum, or wave number, k large compared to the fermi momentum for atoms in a spin state σ to be

$$\rho_\sigma(k) \to \frac{C}{k^4} + \frac{C' + D}{k^6} + O\left(\frac{1}{k^8}\right), \tag{2.16}$$

where C is the previously discussed contact, which may be understood as the asymptote of the scaled momentum distribution given in Fig. 2.3. It is also a measure of the sensitivity of the properties of the system to the inverse scattering length. D is referred to as the derivative contact since it is associated with the second derivative of the contact operator in the leading Lagrangian $\mathcal{L}_0$. It is a measure of the sensitivity of the system's properties to the finite effective range r_s and is calculable from QMC simulations. Further, C' in Eq. (2.16) comes about by incorporating the averaged pair kinetic energy in the system. In the two-body system, for example, $C' = C\,K^2/2$, where K is the momentum of the center of mass of the particles. Since a value for C' is not known at this time, it is not included in Fig. 2.3. However, it is possible that a value could be obtained via a fit to the $1/k^6$ tail of more precise data from QMC simulations. Equation (2.16) for the momentum distribution

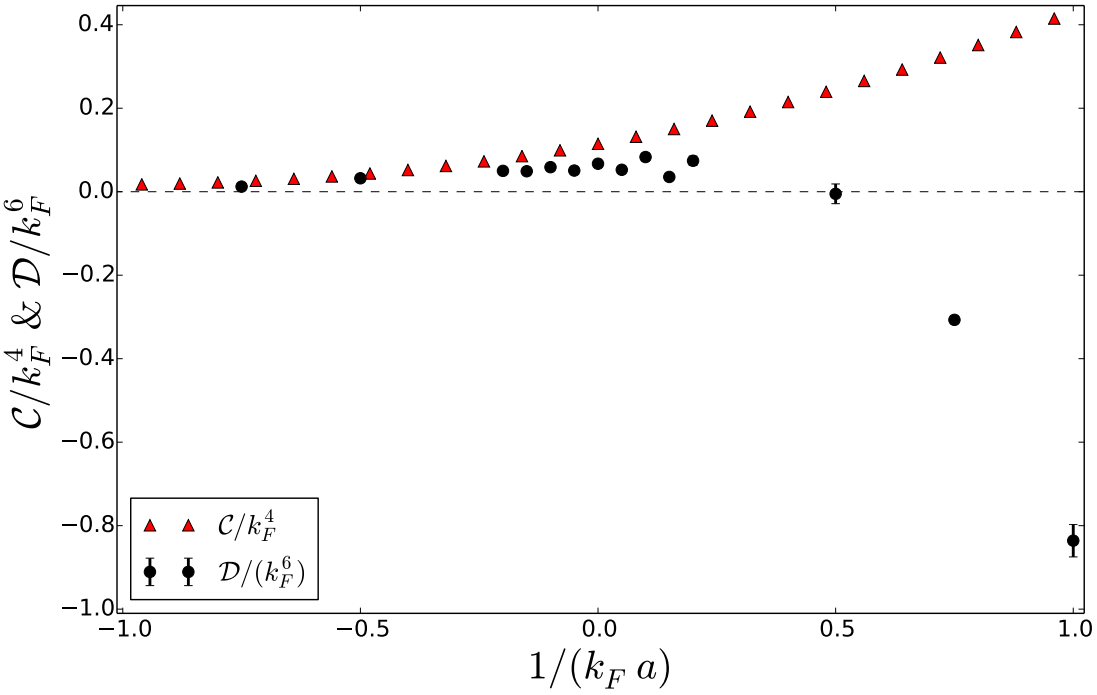

Fig. 2.3 – Dimensionless contact density $\mathcal{C}/k_F^4$, represented by the triangles on the graph, and the derivative contact density $\mathcal{D}/k_F^6$ as a function of $1/(k_F a)$ at zero temperature from QMC simulation in Refs. [56] and [57]. The point $1/(k_F a) = 0$ corresponds to the unitary limit.

is valid in the zero-effective-range limit, and the form of the equation remains the same after taking range corrections into account because those corrections are contained in the coefficients C, C', and D. The derivation of this equation is contained in Sec. 2.4, where it is also demonstrated that the contact and derivative contact are the respective expectation values $\langle \int d^3\mathbf{R}\mathcal{O}_C \rangle$ and $\langle \int d^3\mathbf{R}\mathcal{O}_D \rangle$. $\mathcal{O}_C$ is proportional to the contact term in $\mathcal{L}_0$ and thus the coupling constant λ_0, while $\mathcal{O}_D$ is similarly related to $\mathcal{L}_1$. Additionally, as discussed by Z. Yu *et al.* and P. Zhang *et al.* in Refs. [54, 55], the $1/k^4$ term in the tail of the momentum distribution receives contributions with similar interpretations to C' and D near p- or d-wave resonances.

After deriving the momentum distribution and understanding the three coefficients contained therein, the energy relation may be written. This relation rewrites the sum of the individually UV-cutoff-sensitive kinetic and interaction energies into pieces that are

individually finite and insensitive to the UV cutoff. This is

$$\langle H \rangle = \frac{C}{4\pi m a} + r_s \frac{D}{16\pi m} + \langle T^{(\mathrm{sub})} \rangle, \tag{2.17}$$

in which $\langle H \rangle$ is the expectation value of the Hamiltonian for a generic mixture of energy eigenstates. The contribution to the energy of the system from an external potential has not been included in Eq. (2.17). $T^{(\mathrm{sub})}$ is the renormalized (divergence-subtracted) kinetic energy defined below. The derivation of this equation is also given in Sec. 2.4, and the result is

$$\begin{aligned} \langle T^{(\mathrm{sub})} \rangle = \sum_\sigma \int_0^\infty \frac{dk}{4\pi^2 m} \left[k^4 \rho_\sigma(k) - C - \frac{\theta(k-k_0)}{k^2}(C' + D) + \cdots \right] \\ + \frac{C' + D}{2\pi^2 m k_0} - r_s \frac{C' + 3D}{16\pi m} \,. \end{aligned} \tag{2.18}$$

In order to obtain this equation, we wrote the kinetic energy operator $\mathcal{T}$ defined in Sec. 2.4 in terms of the renormalized operator given in Eq. (2.53). Next, the momentum distribution $\rho_\sigma(k)$ was substituted in for this using the OPE result of Eq. (2.69). The momentum lower limit $k_0 < k$ was imposed in order to avoid an IR divergence in Eq. (2.18), and the second to last term in the same equation removes the dependence on this IR cutoff. Equation (2.17) was derived via the method shown following the momentum distribution derivation at the end of Sec. 2.4. While this energy relation is valid for a generic mixture of states, the relations given in the remainder of this section only hold for a pure eigenstate. If the state of the system is a generic mixture of eigenstates, the relations only approximately hold, and only so long as the off-diagonal terms in the matrices are negligible [15, 16, 17].

As in Ref. [16], the adiabatic relation is defined as the change in the energy of the system due to an adiabatic change in the scattering length a. For the effective range, r_s, a similar adiabatic relation can be determined by taking the derivative of the energy with respect to r_s. The relation involving the derivative with respect to the scattering length is

$$\frac{dE}{da} = \left\langle \frac{dH}{da} \right\rangle = \frac{C}{4\pi m a^2} \,, \tag{2.19}$$

where we used the Feynman–Hellmann theorem to obtain the first equality. For the second equality in Eq. (2.19),

$$\frac{dH}{da} = \int d^3\boldsymbol{R} \frac{\mathcal{O}_C}{(4\pi m a^2)} + O\left(\frac{1}{\Lambda^2}\right) \tag{2.20}$$

was obtained through the use of $d\lambda_0/da = \lambda_0^2/(4\pi a^2)$ and $d\rho_0/da = \rho_0\lambda_0/(2\pi a^2)$. Equation (2.19) remains identical to the form it had in the zero-range limit in Eq. (2.2) because the finite-range correction is contained within the expectation value C.

We find that the adiabatic relation involving the effective-range derivative is given by

$$\frac{dE}{dr_s} = \left\langle \frac{dH}{dr_s} \right\rangle = \frac{D}{16\pi m}\,, \tag{2.21}$$

where the Feynman–Hellmann theorem was again used to move past the first equality of Eq. (2.21), and

$$\frac{dH}{dr_s} = \int d^3\boldsymbol{R} \frac{\mathcal{O}_D}{(16\pi m)} + O(\rho_0) \tag{2.22}$$

was obtained using $d\rho_0/dr_s = \lambda_0^2/(16\pi m)$ and $da/dr_s = d\lambda_0/dr_s = d\Lambda/dr_s = 0$. Terms that are proportional to ρ_0 are dropped, since they are of higher order than NLO when incorporated into H. Thus, D is independent of r_s up to NLO in r_s, i.e. dE/dr_s is well behaved as $r_s \to 0$. This was discussed in Refs. [52, 56, 57].

The next effective-range corrected formulas produced here are the pressure relation [17] and the virial theorem [58]. Further, as the energy of a homogeneous gas scales linearly with the volume, the energy density is expressible as a function of variables that are volume-independent. An example of this is the Helmholtz free-energy density $\mathcal{F}$, which depends only on intensive thermodynamic quantities of the system such as chemical potential μ_σ, the temperature T, and parameters such as the scattering length and effective range. The following equality may be derived from dimensional analysis:

$$\left[T\frac{\partial}{\partial T} + \mu_\sigma \frac{\partial}{\partial \mu_\sigma} - \frac{a}{2}\frac{\partial}{\partial a} - \frac{r_s}{2}\frac{\partial}{\partial r_s}\right]\mathcal{F} = \frac{5}{2}\mathcal{F}, \tag{2.23}$$

where on the left-hand side (LHS) the sum of the logarithmic derivative of each parameter of the system multiplied by its dimension is taken. This reduces to the RHS, which is the free energy multiplied by its energy dimension of 5/2. Then, using the relation between entropy

density s, temperature T, energy density $\mathcal{E}$, and Helmholtz free energy density $\mathcal{F} = \mathcal{E} - Ts$ and the relation $\mathcal{F} = -\mathcal{P} + \mu_\sigma n_\sigma$ we obtain the pressure relation

$$\mathcal{P} = \frac{2}{3}\mathcal{E} + \frac{\mathcal{C}}{12\pi m a} + r_s \frac{\mathcal{D}}{48\pi m}. \tag{2.24}$$

In Eq. (2.24), $\mathcal{E}$, $\mathcal{C}$, and $\mathcal{D}$ are E, C, and D, respectively, divided by the volume of the system.

The next relation we write here is the *energy relation*. It comes again from dimensional analysis for a gas trapped in a harmonic potential $V(\boldsymbol{R})$ with trap frequency ω. The result is

$$\left[\sum_i \omega_i \frac{\partial}{\partial \omega_i} - \frac{a}{2}\frac{\partial}{\partial a} - \frac{r_s}{2}\frac{\partial}{\partial r_s}\right] E = E. \tag{2.25}$$

Then, by using that $\Sigma_i \omega_i \partial V(\boldsymbol{R})/\partial\omega_i = 2V(\boldsymbol{R})$ and Eqs. (2.19) and (2.21) the virial theorem for a trapped atomic gas was obtained as

$$E = 2V - \frac{C}{8\pi m a} - r_s \frac{D}{32\pi m}, \tag{2.26}$$

where the average of the harmonic potential is denoted by V for the system.

The subleading $1/k^6$ tail of the momentum distribution developed here and given in Eq. (2.16) and the relation of the associated derivative contact to the energy given in Eq. (2.21) were first derived through an analysis of the many-body wave function in systems of two-component fermions with a large scattering length in Ref. [52]. It is interesting that these very general results are reproduced here through the use of the OPE for two-body states. Two universal relations that have not been extended here to include range corrections are the *local pair density* and the *inelastic two-body loss rate*. These were studied at leading order in this EFT framework in Refs. [20, 21].

2.3 Ground-state Results for a Homogeneous Gas

Obtaining a numerical value for the derivative contact is necessary if it is to be of meaningful use. In this section, we extract the value of D from recent QMC calculations and compare it

to the value of the contact C in the zero-range limit. The momentum distribution is plotted here with QMC simulation data for comparison.

The energy density of a balanced, homogeneous Fermi gas in its ground state can be expanded about the unitary limit where $1/a \to 0$ and expressed as

$$\mathcal{E} = \left(\xi - \frac{\zeta}{k_F a} + S k_F r_s + \cdots \right) \mathcal{E}_F \,. \tag{2.27}$$

Here, $\mathcal{E}_F = \frac{1}{10\pi^2} k_F^5 / m$ is the Fermi energy density and $k_F = (3\pi^2 n)^{1/3}$ is the Fermi momentum for a system of total number density n. At unitarity, the only scales in the expression for the energy density are the Fermi momentum and the mass. The other parameters in Eq. (2.27) are the so-called Bertsch parameter ξ and slope parameters ζ and S with respect to the $1/k_F a$ and $k_F r_s$ axes, respectively. These parameters approach constant values in the unitary limit. At the same time, the energy density still contains a correction proportional to $k_F r_s$. Additionally, the slope S becomes a function of $k_F a$.

For a Fermi gas, the contact density $\mathcal{C}$ can be calculated in various limits through the use of the expression for the energy of the gas in each limit. The energy density in the unitary limit as given in Eq. (2.27) is an example of this, and by using Eq. (2.19) the contact density can be expressed as

$$\mathcal{C}/k_F^4 \to \frac{4}{9\pi^2}(k_F a)^2, \qquad a \to 0^- \text{ (BCS limit)}, \tag{2.28}$$

$$\to \frac{2\zeta}{5\pi}, \qquad a \to \pm\infty \text{ (unitary limit)}, \tag{2.29}$$

$$\to \frac{4}{3\pi}(k_F a)^{-1}, \qquad a \to 0^+ \text{ (BEC limit)}, \tag{2.30}$$

where ζ is again the constant found in Eq. (2.27) determined from either experimental results or by theoretical means. In the BCS and BEC limits, the energy density expressions are found in Ref. [59]. The dimensionless contact density $\mathcal{C}/k_F^4$ is parametrically suppressed by $(k_F a)^2$ in the BCS limit and enhanced by $1/k_F a$ in the BEC limit. It increases as one moves through unitarity from the BCS to the BEC limit.

The value of the contact has been obtained by various experimental groups through several observables. The contact across the BCS-BEC crossover was first determined via

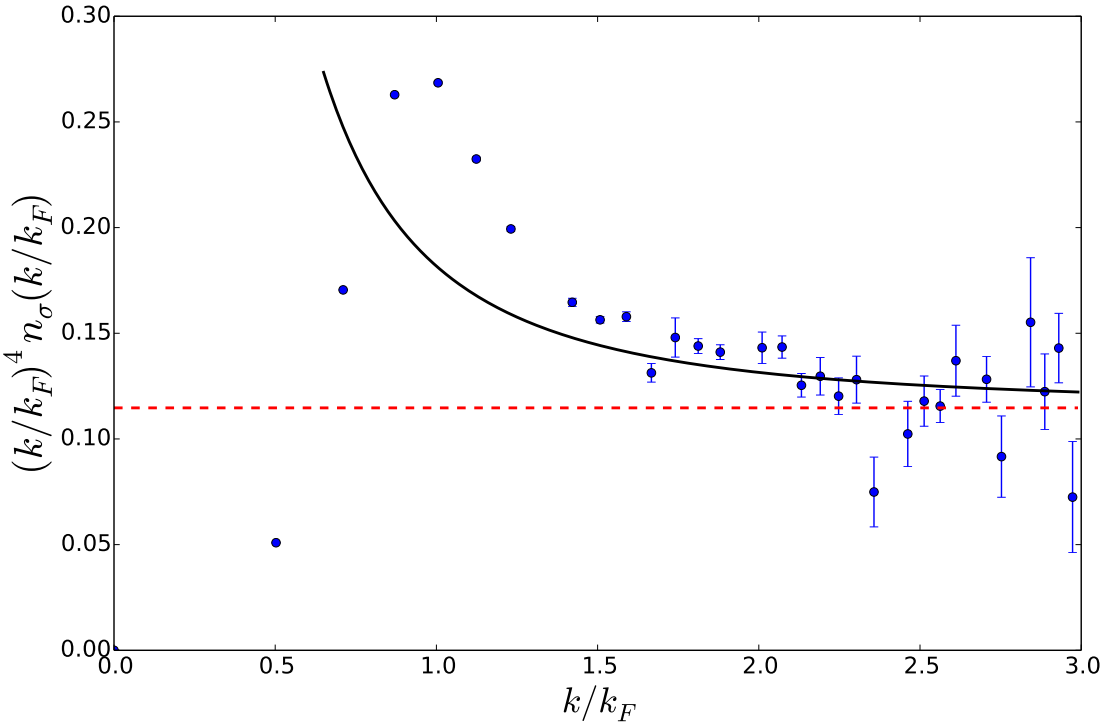

Fig. 2.4 – Scaled momentum distribution close to unitarity, or $(k/k_F)^4 n_\sigma(k/k_F)$. The index σ indicates either of two possible spin states. It is given as a function of k/k_F and compared to the QMC result of Ref. [57]. The dashed horizontal line is $\mathcal{C}/k_F^4$, and the solid line is $\mathcal{C}/k_F^4 + \mathcal{D}/(k_F^4 k^2)$. We use the values near unitarity of $\mathcal{C}/k_F^4 = 0.115$ and $\mathcal{D}/k_F^6 = 0.061$.

photo association in Refs. [60] and [61]. Precise values of the constant ζ were obtained in the unitary limit as $\zeta = 0.93(5)$ from a thermodynamic measurement [62] and as $\zeta = 0.91(4)$ from the static structure factor [63]. The dependence on temperature was determined from the structure factor using Bragg spectroscopy [63, 64], as well as from rf spectroscopy [65]. Several of the universal relations have been verified via testing the consistency of the numerically determined values of the contact obtained from various observables and properties of the system such as the momentum distribution, the rf lineshape, photoemission spectra, the adiabatic theorem, and the virial theorem [66].

The contact has also been calculated using QMC simulations [67, 68, 69, 70, 71, 72] and other methods [73, 74, 75]. At the time of this study, the most accurate theoretical value for ζ is given as $\zeta = 0.901(3)$ in Ref. [76]. This results in a value for the dimensionless contact density of $\mathcal{C}/k_F^4 \approx 0.115$. Further, the slope S from Eq. (2.27) was calculated in

Refs. [56, 57]. The expression for the derivative contact density for the ground state is

$$\mathcal{D} = \frac{8k_F^6}{5\pi} S(k_F a)\,. \tag{2.31}$$

We find some of the asymptotic behavior of the derivative contact density to be

$$\begin{aligned} \mathcal{D}/k_F^6 \to & \frac{8S}{5\pi}\,, && a \to \pm\infty \text{ (unitary limit)}, \\ \to & -0.9(1)(k_F a)^{-3}\,, && a \to 0^+ \text{ (BEC limit)}, \end{aligned} \tag{2.32}$$

where $S = 0.12(1)$ was obtained in Ref. [57]. This gives a resulting value of $\mathcal{D}/k_F^6 = 0.061$ in the unitary limit. Equation (2.32) may be derived with the use of Eq. (2.27), and the relationship between $\mathcal{D}$ and the derivative of the energy with respect to the effective range given in Eq. (2.21). The result obtained in this study for $\mathcal{D}/k_F^6$ in the BEC limit, or $1/k_F a > 0$, resulted from fitting $\mathcal{D}$ to the QMC data for S [57] shown in Fig. 2.4. Note that the data in this figure are rescaled by the leading factor found in Eq. (2.31). The expression for the dimer binding energy, given by $E_{\text{dimer}} = 1/(ma^2)[1 + r_s/a + \cdots]$, gives the derivative contact for the dimer as $D_{\text{dimer}} = 16\pi/a^3$. This is consistent with the power law in the BEC limit. A power law in the BCS limit was not known at the time of this work.

Figure 2.3 displays the scaled contact density $\mathcal{C}/k_F^4$ and derivative contact density $\mathcal{D}/k_F^6$ as a function of $1/k_F a$. $\mathcal{C}$ is roughly twice as large as $\mathcal{D}$ in the unitary limit. However, in the BEC limit, the magnitude of $\mathcal{D}$ increases at a faster rate than that of $\mathcal{C}$, which follows from the fact that in this limit, the effective-range correction is more important as the approximation of universal physics deteriorates. Figure 2.4 shows the scaled momentum distribution near the unitary limit. The OPE results in Eq. (2.16) describe the QMC data of Ref. [57] well when $k \gtrsim 1.5k_F$. The as-yet unknown contribution from C', originating from the center of mass kinetic energy, is not included in this study.

2.4 Operator Product Expansion and Related Calculations

This section contains a detailed description of the methods used in this work. Included is a description of the nonlocal coordinate space operator that gives the momentum distribution in the large-k, or short-distance limit, which is used in the derivation of the above universal relations. The OPE was developed separately by Wilson [18], Kadanoff [19], and Polyakov [51] in 1969. It was developed in the field of high-energy physics and has been used, for example, to describe certain properties of deep inelastic scattering of an electron off of a hadron [77], but its range of applicability is broader than just the high-energy regime. It provides an expansion of a spatially nonlocal operator into a series of local operators with coefficients that are functions of the relative spatial separation $\boldsymbol{r}$, as long as $\boldsymbol{r}$ is small. The resulting expansion of the product of operators $\mathcal{O}_A$ and $\mathcal{O}_B$ separated in space by nonlocal distance $\boldsymbol{r}$ is given by

$$\mathcal{O}_A\left(\boldsymbol{R}-\frac{\boldsymbol{r}}{2}\right)\mathcal{O}_B\left(\boldsymbol{R}+\frac{\boldsymbol{r}}{2}\right)=\sum_n W_n(\boldsymbol{r})\mathcal{O}_n(\boldsymbol{R}), \tag{2.33}$$

where, in general, this is an infinite sum over all possible local operators and W_n denotes the *Wilson* coefficient corresponding to each local operator $\mathcal{O}_n(\boldsymbol{r})$. Using the OPE, we derive expressions for the two-body contact and derivative contact in terms of expectation values of field-theoretical operators. The Hamiltonian is then expressed in terms of those operators.

The nonlocal operator that is considered in this work is the one-body density operator corresponding to the coordinate-space representation of the momentum distribution given by $\psi^\dagger_\sigma(\boldsymbol{R}-\boldsymbol{r}/2)\psi_\sigma(\boldsymbol{R}+\boldsymbol{r}/2)$. The Fourier transform of this leads to the momentum-space distribution $\rho_\sigma(\boldsymbol{k})$ for particles of spin σ. This can be better understood by first writing the momentum distribution as

$$\rho_\sigma(\boldsymbol{k})=\langle\tilde{\psi}^\dagger_\sigma(\boldsymbol{k})\tilde{\psi}_\sigma(\boldsymbol{k})\rangle\,, \tag{2.34}$$

where $\tilde{\psi}^\dagger_\sigma(\boldsymbol{k})$ is the Fourier transform of the coordinate-space quantum field $\psi_\sigma(\boldsymbol{r})$. Thus it can be seen that in terms of the coordinate-space representation, the momentum distribution

in Eq. (2.34) is

$$\rho_\sigma(\boldsymbol{k}) = \int_{\boldsymbol{R}} \int_{\boldsymbol{r}} e^{i\boldsymbol{k}\cdot\boldsymbol{r}} \left\langle \psi_\sigma^\dagger(\boldsymbol{R}-\boldsymbol{r}/2)\psi_\sigma(\boldsymbol{R}+\boldsymbol{r}/2)\right\rangle \,, \tag{2.35}$$

$$= \sum_n \int_{\boldsymbol{r}} e^{i\boldsymbol{k}\cdot\boldsymbol{r}} W_n(\boldsymbol{r}) \int_{\boldsymbol{R}} \langle \mathcal{O}_n(\boldsymbol{R})\rangle \,, \tag{2.36}$$

where $\int_{\boldsymbol{R}} = \int d^3\boldsymbol{R}$ and $\int_{\boldsymbol{r}} = \int d^3\boldsymbol{r}$, the W_n are two-body Wilson coefficients. Equation (2.33) was used to rewrite the RHS of Eq. (2.35) with the OPE to form Eq. (2.36).

Operators on the RHS of Eq. (2.36) have been constructed out of the EFT fields and their coordinate-space derivatives. The field ψ_σ has dimension $\Delta = 3/2$ in the EFT expansion, the dimension of the Galilean invariant derivative

$$\overleftrightarrow{\partial_i} = \overrightarrow{\partial_i} - \overleftarrow{\partial_i} \tag{2.37}$$

is $\Delta = 1$, and the derivative with respect to time has $\Delta = 2$. The direction of the arrows indicate whether the field to the left or to the right has its derivative taken when Eq. (2.37) is inserted between two fields. Operators up to dimension $\Delta = 6$ which are relevant for this problem are listed here:

Δ	$\mathcal{O}_{1,\Delta}$	$\mathcal{O}_{2,\Delta}$
3	$\psi_\sigma^\dagger\psi_\sigma$	
4	$\psi_\sigma^\dagger \overleftrightarrow{\partial_i}\psi_\sigma$	$\psi_1^\dagger\psi_2^\dagger\psi_2\psi_1$
5	$\psi_\sigma^\dagger \overleftrightarrow{\partial_i}\overleftrightarrow{\partial_j}\psi_\sigma$	$\psi_1^\dagger\psi_2^\dagger\psi_2 \overleftrightarrow{\partial_i}\psi_1 + h.c.$
6	$\psi_\sigma^\dagger \overleftrightarrow{\partial_i}\overleftrightarrow{\partial_j}\overleftrightarrow{\partial_k}\psi_\sigma$	$\psi_1^\dagger\psi_2^\dagger\psi_2 \overleftrightarrow{\partial_i}\overleftrightarrow{\partial_j}\psi_1 + h.c.$

(2.38)

The importance of each of these field-theoretical operators is indicated by its dimension. A lower dimension signifies greater importance in the momentum distribution.

The unit operator is not listed here because it does not enter the problem, as the momentum distribution for the vacuum is zero. Additionally, the time derivative ∂_t is omitted here because it can be eliminated and replaced with momentum-dependent operators using the equations of motion one may obtain from Eqs. (2.6) and (2.7) [53]. In the first column in the list of operators, the numbers given correspond to the dimension of operators in each

respective row. The second and third columns give the one- and two-body operators, as indicated by the subscript of $\mathcal{O}_{1,\Delta}$ and $\mathcal{O}_{2,\Delta}$ at the top of the table. It was discussed in Ref. [20] that the dimension of $\psi_1^\dagger\psi_2^\dagger\psi_2\psi_1$ is lowered to $\Delta = 4$ from $\Delta = 6$ due to the strong interaction. A similar effect takes place for the operator $\psi_1^\dagger\psi_2^\dagger\psi_2 \overleftrightarrow{\partial_i}\overleftrightarrow{\partial_j}\psi_1$ such that its dimension is $\Delta = 6$ rather than $\Delta = 8$.

Equation (2.33) may be rewritten more suitably for the problem at hand as

$$\psi_\sigma^\dagger(\boldsymbol{R} - \boldsymbol{r}/2)\psi_\sigma(\boldsymbol{R} + \boldsymbol{r}/2) = \sum_\Delta \left(W_{1,\Delta}(\boldsymbol{r})\,\mathcal{O}_{1,\Delta}(\boldsymbol{R}) + W_{2,\Delta}(\boldsymbol{r})\,\mathcal{O}_{2,\Delta}(\boldsymbol{R}) + \cdots\right) , \tag{2.39}$$

where the index n of each $W_{n,\Delta}$ is indicative of whether the coefficient corresponds to a one- or two-body operator, and the second index Δ gives the scaling dimension of the operator. Wilson coefficients were determined in this study for one- and two-body operators through dimension $\Delta = 6$. At leading order, only operators through dimension $\Delta = 4$ were needed and the result was comparatively simple. At LO, the nonlocal matrix element and the one- and two-body matrix elements may be calculated using Figs. 2.5, 2.6, and 2.7 below with the LO amplitude inserted wherever $\mathcal{A}$ is written in the figures. The OPE at leading order allowed the nonlocal matrix element to be expressed as found in Ref. [20], namely

$$\begin{aligned}\left\langle\psi_\sigma^\dagger(\boldsymbol{R} - \boldsymbol{r}/2)\psi_\sigma(\boldsymbol{R} + \boldsymbol{r}/2)\right\rangle =& W_{1,3}(\boldsymbol{r})\langle\mathcal{O}_{1,3}(\boldsymbol{R})\rangle + W_{1,4}\langle\mathcal{O}_{1,4}(\boldsymbol{R})\rangle + W_{2,4}\langle\mathcal{O}_{2,4}(\boldsymbol{R})\rangle\,, \quad (2.40)\\ =& \langle\psi_\sigma^\dagger\psi_\sigma(\boldsymbol{R})\rangle + \frac{1}{2}r_i\langle\psi_\sigma^\dagger \overleftrightarrow{\partial_i}\psi_\sigma(\boldsymbol{R})\rangle - \frac{r}{8\pi}\langle\lambda_0^2\psi_1^\dagger\psi_2^\dagger\psi_2\psi_1(\boldsymbol{R})\rangle\,, \quad (2.41)\end{aligned}$$

where an Einstein summation convention is assumed over like-indices. Matching the RHS of Eq. (2.40) onto the evaluated LHS nonlocal matrix element in the same equation facilitated the calculation of the coefficients leading the operator matrix elements in Eq. (2.41). And, as the Fourier transform of r gives $1/k^4$, it was discovered [20] that the LO contact is given by $C = \int_{\boldsymbol{R}}\langle\lambda_0^2\psi_1^\dagger\psi_2^\dagger\psi_2\psi_1(\boldsymbol{R})\rangle$, as this operator corresponds to the large-k tail of the momentum distribution. Greater detail is presented in the NLO calculations below on the method of doing this matching.

To compute the NLO momentum distribution and other universal relations, we must introduce the off-shell (or 'off of the mass shell' in energy-momentum space) scattering amplitude $\mathcal{A}(E, \boldsymbol{p}, \boldsymbol{k})$, in which the ingoing and outgoing momenta p and k are not necessarily the same and can have magnitudes $p \neq k \neq \sqrt{mE}$, prior to detailing the calculation of the needed matrix elements forming the RHS of the OPE. This off-shell amplitude must be known in order to correctly obtain the various Wilson coefficients. When we considered the renormalization of the theory in Sec. 2.1, the on-shell amplitude depending upon relative momentum k, with $k^2 = mE$, was included. Here, the off-shell amplitude must be used in order to match the operators in Eq. (2.39) to the corresponding terms in the nonlocal matrix element. This is because it explicitly contains a momentum dependence that contributes to the loop integral results in the calculation. Generally, the off-shell amplitude with incoming momenta $(E/2, \pm\boldsymbol{p})$ and outgoing momenta $(E/2, \pm\boldsymbol{k})$ ought to be a function of three variables, namely E, $\boldsymbol{p}$, and $\boldsymbol{k}$. But, the leading order amplitude, $\mathcal{A}_{\rm LO}(E)$ is dependent only on the total energy and not on external momenta. So, the calculation of a loop diagram containing $\mathcal{A}_{\rm LO}(E)$ is simplified by factorization into a product of the amplitude and the loop integral, as shown in the last term of Eq. (2.9).

But, at NLO this is no longer true because the diagrammatic ρ_0 vertex is momentum-dependent. Thus, an expansion of the off-shell amplitude in powers of $1/\Lambda$ gives

$$\begin{aligned}\mathcal{A}_{\rm LO} - \mathcal{A}_{\rm LO}^2 \frac{m(mE)}{2\pi^2\Lambda} - \mathcal{A}_{\rm LO}^2 \frac{2m^2\rho_0 mE}{\lambda_0^2} \\ + \mathcal{A}_{\rm LO} \frac{m\rho_0}{\lambda_0}(\boldsymbol{p}^2 + \boldsymbol{k}^2 - 2mE) + \cdots ,\end{aligned} \tag{2.42}$$

where the LO amplitude is proportional to $1/E$ and the two following terms are NLO in $1/\Lambda$ and reduce to Eq. (2.13) in the on-shell limit. The last term in Eq. (2.42) is proportional to $\boldsymbol{p}^2/\Lambda^2$, and terms beyond this are power suppressed. The parameters a^{-1}, $\boldsymbol{p}$, $\boldsymbol{k}$, and $\sqrt{mE}$ are of the same size or much smaller than Λ, but $\lambda_0 \sim 1/\Lambda$ and $\rho_0 \sim 1/\Lambda^3$. Terms that are of order $1/\Lambda^2$ may be dropped when the task at hand is computing the NLO amplitude, in which case $\mathcal{A}_{\rm NLO}$ is only a function of E. On the other hand, when calculating matrix elements necessary in the OPE, the term that is proportional to $\boldsymbol{p}^2 + \boldsymbol{k}^2$ contributes loop momentum factors in the diagrams containing the amplitude and can lead to a UV divergence. The

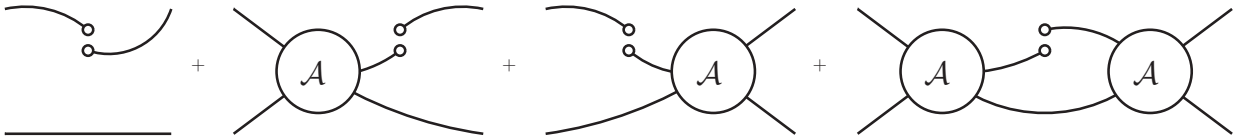

Fig. 2.5 – Diagrams for the operator $\langle\psi^\dagger_\sigma(\boldsymbol{R}-\boldsymbol{r}/2)\psi_\sigma(\boldsymbol{R}+\boldsymbol{r}/2)\rangle$ for the 2 atom scattering state. The empty dots imply locations $\pm\boldsymbol{r}/2$ where an atom is annihilated and created at an equal time.

important implication is that terms of order $1/\Lambda^2$ may be dropped only at the end of a calculation, or NLO terms will be missed.

We keep terms of size $\sim 1/\Lambda$ in the final NLO results and renormalize the operators either by a multiplying renormalization factor or the addition of different operators as counterterms that subtract both divergences and any Λ-dependence. The complete off-shell amplitude $\mathcal{A}(E,\boldsymbol{p},\boldsymbol{k})$ is rewritten here in terms of the amplitude $\mathcal{A}_\lambda(E)$ containing diagrams with only the λ_0 coupling constant, as well as $\mathcal{A}_\rho(E)$ and $\mathcal{A}_{\rho'}(E)$. The latter two amplitudes contain one power of the coupling constant ρ_0 but scale as $1/\Lambda$ and $1/\Lambda^2$, respectively. In all three aforementioned amplitudes, any power suppressed terms $\sim(\sqrt{mE}/\Lambda)^n$ in loop integral $\mathcal{I}_0(E,\Lambda)$ are kept. The off-shell amplitude is

$$\begin{aligned}
\mathcal{A}(E,\boldsymbol{p},\boldsymbol{k}) &= \mathcal{A}(E) + (\boldsymbol{p}^2+\boldsymbol{k}^2-2mE)\mathcal{A}_{\rho'}(E)\,,\\
\mathcal{A}(E) &= \mathcal{A}_\lambda(E) + \mathcal{A}_\rho(E)\,,\\
\mathcal{A}_\lambda &= -\frac{1}{m/\lambda_0 + i\mathcal{I}_0(E,\Lambda)}\,,\\
\mathcal{A}_\rho &= -\frac{2\rho_0 m^2}{\lambda_0^2} mE\,\mathcal{A}_\lambda^2\,,\\
\mathcal{A}_{\rho'} &= \frac{\rho_0 m}{\lambda_0}\,\mathcal{A}_\lambda\,,
\end{aligned} \tag{2.43}$$

where $\mathcal{I}_0(E,\Lambda)$ is given in the Appendix in Eq. (A.2). Additionally, $\mathcal{A}_\lambda$ still fulfills the LS equation given by Eq. (2.9) with $\mathcal{A}_\lambda$ in place of $\mathcal{A}_{\rm LO}$:

$$\mathcal{A}_\lambda = -\lambda_0/m(1+\mathcal{I}_0\, i\mathcal{A}_\lambda)\,. \tag{2.44}$$

Figure 2.5 shows the diagrams which contribute to the matrix element for the two-atom scattering state of incoming four-momenta $(p_0, \pm\boldsymbol{p})$ and outgoing momenta $(k_0, \pm\boldsymbol{k})$, as well as a total energy equal to $E = 2p_0 = 2k_0$. In this study, this is generalized to a system with nonzero CM momentum, and the results are shown below. The nonlocal operator matrix element is

$$\begin{aligned}\langle\psi_\sigma^\dagger(\boldsymbol{R}-\tfrac{\boldsymbol{r}}{2})\psi_\sigma(\boldsymbol{R}+\tfrac{\boldsymbol{r}}{2})\rangle = \delta_{\boldsymbol{pk}}e^{i\boldsymbol{p}\cdot\boldsymbol{r}} + \left[\frac{ie^{i\boldsymbol{p}\cdot\boldsymbol{r}}}{p_0-\frac{\boldsymbol{p}^2}{2m}}i\mathcal{A}(E) + (p\to k)\right] - \mathcal{I}_{\rho,0}\,\mathcal{A}^2(E) \\ - 2\big[(\tfrac{\boldsymbol{p}^2+\boldsymbol{k}^2}{2} - 2mE)\mathcal{I}_{\rho,0} + \mathcal{I}_{\rho,2}\big]\mathcal{A}_\lambda\mathcal{A}_{\rho'}\,, \qquad (2.45)\end{aligned}$$

where we use the shorthand notation $\delta_{\boldsymbol{pk}} = (2\pi)^3\delta^{(3)}(\boldsymbol{p}-\boldsymbol{k})$. The loop integral $\mathcal{I}_{\rho,2n}$ is in Appendix A in Eq. (A.10). The symbol $(p\to k)$ indicates the presence of a term identical to the previous one in braces in which p has been replaced by k.

Through the insertion of $\mathcal{I}_{\rho,0}$ and $\mathcal{I}_{\rho,2}$ from Eq. (A.10) into Eq. (2.45) and the expansion in powers of r (not to be mistaken for r_s) through r^3, we then obtain

$$\begin{aligned}\langle\psi_\sigma^\dagger(\boldsymbol{R}-\tfrac{\boldsymbol{r}}{2})\psi_\sigma(\boldsymbol{R}+\tfrac{\boldsymbol{r}}{2})\rangle = \delta_{\boldsymbol{pk}} - \left[\frac{\mathcal{A}(E)}{p_0-\frac{\boldsymbol{p}^2}{2m}} + (p\to k)\right] + \frac{i\mathcal{A}^2(E)m^2}{8\pi\sqrt{mE}} \\ + ir_ip_i\delta_{\boldsymbol{pk}} - ir_i\left[\frac{p_i\,\mathcal{A}(E)}{p_0-\frac{\boldsymbol{p}^2}{2m}} + (p\to k)\right] - r\,\frac{\mathcal{A}^2(E)m^2}{8\pi} \\ - r_ir_j\frac{p_ip_j}{2}\delta_{\boldsymbol{pk}} + \frac{r_ir_j}{2}\left[\frac{p_ip_j\mathcal{A}(E)}{p_0-\frac{\boldsymbol{p}^2}{2m}} + (p\to k)\right] - ir^2\,\frac{\mathcal{A}^2(E)m^2\sqrt{mE}}{16\pi} \\ - ir_ir_jr_k\frac{p_ip_jp_k}{6}\delta_{\boldsymbol{pk}} + i\frac{r_ir_jr_k}{6}\left[\frac{p_ip_jp_k\mathcal{A}(E)}{p_0-\frac{\boldsymbol{p}^2}{2m}} + (p\to k)\right] + r^3\,\frac{\mathcal{A}^2(E)m^3E}{48\pi} \\ + \mathcal{O}(r^4)\,, \qquad (2.46)\end{aligned}$$

where the Einstein summation convention for like indices is assumed. Further, we drop terms of $O(1/\Lambda^2)$ at this point, following the previously described prescription. In Eq. (2.46), there are $\sqrt{mE}$-dependent terms that are distinguished from $|\boldsymbol{p}|$-dependent terms because the atoms are kept off-shell in the calculations, i.e. $E \neq \boldsymbol{p}^2/m$. Each of the terms in this equation must be matched to the matrix elements of the related local operators, and it is by this process that the Wilson coefficients of the local operators are determined. $\mathcal{A}^2(E)$

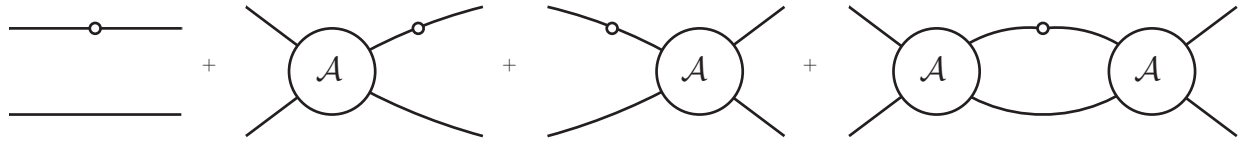

Fig. 2.6 – Diagrams for one-body operator. Empty dots imply an insertion of the one-body operator given in Eq. (2.38) and $\mathcal{A}(E, \boldsymbol{p}, \boldsymbol{k})$ represents the off-shell amplitude of Eq. (2.43).

gives the renormalized square amplitude with the first effective-range correction. However, Eq. (2.46) remains valid in the zero-range limit, as alluded to previously, where $\mathcal{A}(E)$ is replaced by $\mathcal{A}_{\rm LO}$. As the r^3 term is still present, it is evident that the $1/k^6$ correction to the momentum distribution at large momentum is still present even if $r_s \to 0$.

In the following subsection, we calculate the matrix elements of local operators for the two-body scattering state. As noted in the calculation of the nonlocal operator, the power-suppressed terms in Eq. (2.43) are not dropped during intermediate steps. Terms up to NLO in the EFT expansion are kept only after the renormalization process.

2.4.1 One-body local operators

We present the detailed calculation of matrix elements for one-body operators of various scaling dimensions in this subsection. These correspond to the operators labeled $\mathcal{O}_{1,\Delta}$ in Eq. (2.38). The Feynman diagrams in Fig. 2.6 show all contributions of operators of the form $\mathcal{O}_{1,\Delta}$ to the two-atom scattering state. The first diagram is the only one present in the absence of two-body interactions. Because Fig. 2.6 holds for any one-body operator, the matrix element for a one-body operator has the general form

$$\begin{aligned}\langle \mathcal{O}_{1,\Delta} \rangle = v_{1,\Delta}(\boldsymbol{p})\, \delta_{\boldsymbol{pk}} - \left[\frac{v_{1,\Delta}(\boldsymbol{p})\ \mathcal{A}(E)}{p_0 - \boldsymbol{p}^2/(2m)} + (p \to k) \right] \\ - \mathcal{I}_0^{(1,\Delta)}\, \mathcal{A}^2(E) - 2\big[(\tfrac{\boldsymbol{p}^2+\boldsymbol{k}^2}{2} - 2mE)\mathcal{I}_0^{(1,\Delta)} + \mathcal{I}_2^{(1,\Delta)}\big] \mathcal{A}_\lambda \mathcal{A}_{\rho'}\,, \end{aligned} \tag{2.47}$$

in which $v_{1,\Delta}(\boldsymbol{p})$ is the vertex factor corresponding to operator $\mathcal{O}_{1,\Delta}$. These factors up through dimension $\Delta = 6$ are tabulated in Table A.1 of Appendix A. The loop integrals $\mathcal{I}_{2n}^{(1,\Delta)}$ are given in the same appendix in Eq. (A.4).

For operator $\mathcal{O}_{1,3} = \psi_\sigma^\dagger \psi_\sigma$, the matrix element for a two-body state of ingoing relative momentum $\boldsymbol{p}$ and outgoing momentum $\boldsymbol{k}$ is

$$\begin{aligned}\langle \mathcal{O}_{1,3} \rangle =& \delta_{\boldsymbol{pk}} - \left[\frac{\mathcal{A}(E)}{p_0 - \boldsymbol{p}^2/(2m)} + (p \to k) \right] \\ &+ \frac{im^2 \mathcal{A}^2(E)}{8\pi\sqrt{mE}} \Big(1 + ir_s \sqrt{mE} \Big) + O(\Lambda^{-2}) \,. \end{aligned} \tag{2.48}$$

In this equation $r_s \mathcal{A}^2(E) = r_s \mathcal{A}_\lambda^2$ up to NLO in the effective range. We then match Eq. (2.48) to the second line of Eq. (2.46), other than the term proportional to r_s. The Wilson coefficient so obtained is

$$W_{1,3} = 1 \,. \tag{2.49}$$

The term proportional to the range is subtracted later through the inclusion of the appropriate term in the Wilson coefficient of the two-body operator of Eq. (2.59), below.

The next term needed for the OPE matching process is $\mathcal{O}_{1,4} = \psi_\sigma^\dagger \overleftrightarrow{\partial_i} \psi_\sigma$, and it gives the matrix element

$$\langle \mathcal{O}_{1,4} \rangle = 2ip_i \delta_{\boldsymbol{pk}} - \left[\frac{2ip_i \mathcal{A}(E)}{p_0 - \boldsymbol{p}^2/(2m)} + (p \to k) \right] . \tag{2.50}$$

Making a comparison of this term to ones containing one power of p_i in Eq. (2.46), we find that the Wilson coefficient multiplying $\mathcal{O}_{1,4}$ is

$$W_{1,4} = \frac{1}{2} r_i \ . \tag{2.51}$$

The next operator to consider is $\mathcal{O}_{1,5} = \psi_\sigma^\dagger \overleftrightarrow{\partial_i} \overleftrightarrow{\partial_j} \psi_\sigma$, and we calculate the related matrix element as

$$\begin{aligned}\langle \mathcal{O}_{1,5} \rangle =& -4p_i p_j \, \delta_{\boldsymbol{pk}} + \left[\frac{4p_i p_j \mathcal{A}(E)}{p_0 - \boldsymbol{p}^2/(2m)} + (p \to k) \right] - \frac{4\delta_{ij}}{3} \left[i \frac{d\mathcal{I}_2}{dE} \right] \mathcal{A}^2(E) \\ &- \frac{4m\delta_{ij}}{3} \left[\frac{m\Lambda^3}{3\pi^2} + \left(\tfrac{\boldsymbol{p}^2 + \boldsymbol{k}^2}{m} - 2E \right) i \frac{d\mathcal{I}_2}{dE} + 2imE\mathcal{I}_0 \right] \mathcal{A}_\lambda \mathcal{A}_{\rho'} \,. \end{aligned} \tag{2.52}$$

Table 2.1 – One-body Operators

Δ	$\mathcal{O}_{1,\Delta}$	$W_{1,\Delta}$
3	$\psi_\sigma^\dagger \psi_\sigma$	1
4	$\psi_\sigma^\dagger \overleftrightarrow{\partial_i} \psi_\sigma$	$\frac{1}{2} r_i$
5	$\psi_\sigma^\dagger \overleftrightarrow{\partial_i} \overleftrightarrow{\partial_j} \psi_\sigma^{(\text{ren})}$	$\frac{1}{8} r_i r_j$
6	$\psi_\sigma^\dagger \overleftrightarrow{\partial_i} \overleftrightarrow{\partial_j} \overleftrightarrow{\partial_k} \psi_\sigma$	$\frac{1}{48} r_i r_j r_k$

One-body operators up to scaling dimension 6 and their Wilson coefficients $W_{1,\Delta}$, where the subscript '1' indicates a one-body operator and Δ corresponds to the dimensionality of that operator.

This matrix element contains a linear divergence coming from the fact that $\Lambda^3 \mathcal{A}_{\rho'} \sim \Lambda$, and this and other cutoff dependent terms are renormalized through the addition of the two-body operators $\psi_1^\dagger \psi_2^\dagger \psi_2 \psi_1$ and $\psi_1^\dagger \psi_2^\dagger \psi_2 \overleftrightarrow{\nabla}^2 \psi_1$ with the appropriate factors. The one-body operator $\psi_\sigma^\dagger \overleftrightarrow{\partial_i} \overleftrightarrow{\partial_j} \psi_\sigma$ becomes the kinetic energy term in the Hamiltonian when i and j are contracted, and the cutoff dependence of the corresponding matrix element implies that the kinetic energy is sensitive to the short-distance region of an underlying potential of a size smaller than the length scale $a \sim 1/\sqrt{mE}$, beyond which the effective theory of this work loses predictive power. However, through this renormalization procedure, we find combinations of operators that are insensitive to this short-distance behavior.

Using the two-body operators from Sec. 2.1 in their renormalized forms shown below in Eqs. (2.59) and (2.64), we calculate the result for the renormalized one-body operator of dimension $\Delta = 5$ as

$$\begin{aligned} \langle \mathcal{O}_{1,5}^{(\text{ren})} \rangle &= \left\langle \mathcal{O}_{1,5} + \frac{2\delta_{ij}}{3\pi^2} \left[\Lambda \big(1 + \tfrac{2z}{3}\big)\, \mathcal{O}_{2,4}^{(\text{ren})} + \frac{1-3z}{4\Lambda} \mathcal{O}_{2,6}^{(\text{ren})} \right] \right\rangle \\ &= -4 p_i p_j \delta_{\boldsymbol{pk}} + \left[\frac{4 p_i p_j \mathcal{A}(E)}{p_0 - \boldsymbol{p}^2/(2m)} + (p \to k) \right] - i\delta_{ij} \frac{\sqrt{mE}}{2\pi} m^2 \mathcal{A}^2(E) + O(\Lambda^{-2})\,. \end{aligned} \tag{2.53}$$

In Eq. (2.53), $z = \frac{m\rho_0 \Lambda^2}{\lambda_0}$, and the superscript $^{(\text{ren})}$ indicates a renormalized operator whose UV behavior is properly regularized. Comparing Eq. (2.53) to the $O(r^2)$ terms of Eq. (2.46),

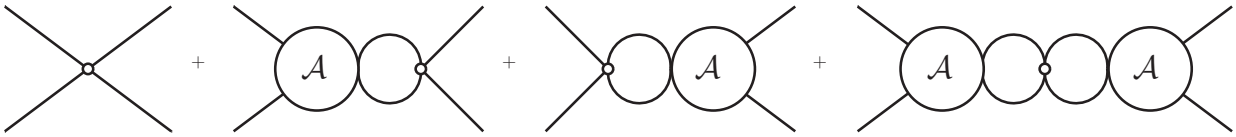

Fig. 2.7 – Diagrams for 2-body operators. The empty dots indicate the insertion of a two-body operator.

this operator's Wilson coefficient is calculated to be

$$W_{1,5} = \frac{1}{8} r_i r_j. \tag{2.54}$$

The last one-body matrix element considered here is for the operator $\mathcal{O}_{1,6} = \psi_\sigma^\dagger \overleftrightarrow{\partial_i} \overleftrightarrow{\partial_j} \overleftrightarrow{\partial_k} \psi_\sigma$ and is given by

$$\langle \mathcal{O}_{1,6} \rangle = -i8 p_i p_j p_k \delta_{\boldsymbol{pk}} + \left[\frac{i8 p_i p_j p_k \mathcal{A}(E)}{p_0 - \boldsymbol{p}^2/(2m)} + (p \to k) \right]. \tag{2.55}$$

It is not necessary to conduct any renormalization process for this operator because its results are already finite and cutoff-independent. And, comparing it to the terms of $O(r^3)$ found in Eq. (2.46), the corresponding Wilson coefficient is

$$W_{1,6} = \frac{1}{48} r_i r_j r_k \,. \tag{2.56}$$

Table 2.1 provides a summary of Wilson coefficients corresponding to the relevant one-body operators in this study.

2.4.2 Two-body local operators

In this section, we calculate matrix elements for operators of the form $\mathcal{O}_{2,\Delta}$ in detail for two-atom scattering states, and each operator's Wilson coefficient is determined. Figure 2.7 contains the relevant diagrams. Two-body operators of dimensions 4 and 6 are the only ones for which matrix elements need to be calculated for the momentum distribution and other universal relations.

Since Fig. 2.7 is the complete set of diagrams for any two-body operator, the general matrix element of a two-body operator is written

$$\begin{aligned}\langle \mathcal{O}_{2,\Delta} \rangle =&(1 + i\mathcal{I}_0\mathcal{A}(E))\big[v_{2,\Delta}(p,k) + 2i\mathcal{I}_0^{(2,\Delta)}\mathcal{A}(E)\big] \\ &+ i\mathcal{A}_{\rho'}\Big\{ 2\mathcal{I}_2^{(2,\Delta)}(1 + i\mathcal{I}_0\mathcal{A}_\lambda) + \mathcal{I}_2\big[v_{2,\Delta}(p,k) + 2i\mathcal{I}_0^{(2,\Delta)}\mathcal{A}_\lambda\big] \\ &+ (\boldsymbol{p}^2 + \boldsymbol{k}^2 - 4mE)(1 + 2i\mathcal{I}_0\mathcal{A}_\lambda)\mathcal{I}_0^{(2,\Delta)} \\ &+ \Big[v_{2,\Delta}(p)(\boldsymbol{k}^2 - 2mE) + v_{2,\Delta}(k)(\boldsymbol{p}^2 - 2mE)\Big]\mathcal{I}_0 \Big\}, \end{aligned} \tag{2.57}$$

where $v_{2,\Delta}(p,k) = v_{2,\Delta}(p) + v_{2,\Delta}(k)$ is the vertex factor for the two-body operator of dimension Δ. These factors are presented in Table A.2 of Appendix A up to scaling dimension 6. As a matter of convenience, we break the vertex factors into terms depending on a vertex's ingoing and outgoing momenta. These factors can depend either on the external or loop momentum of the particles. Terms that are loop-momentum dependent are included in the integrals $\mathcal{I}_0$ and $\mathcal{I}_2$ defined in Eq. (A.1). It is important to note here that $\mathcal{O}_{2,4}$ has a momentum-independent vertex factor given by $v_{2,4}(p,k) = 1$. The way this is broken up is by assigning $v_{2,4}(p) = 1/2$ and $v_{2,4}(k) = 1/2$ in order to follow the prescription of Eq. (2.57). Further, one may not directly use the LS equation to simplify $(1 + i\mathcal{I}_0\mathcal{A})$ in the equation above because of the fact that $\mathcal{A}(E) = \mathcal{A}_\lambda + \mathcal{A}_\rho$ in this case. The LS equation includes only $\mathcal{A}_\lambda$. Further, any factors of the energy-dependent amplitude that multiply $\mathcal{A}_{\rho'}$ must be $\mathcal{A}_\lambda$ and not $\mathcal{A}_\rho$ because only terms that are NLO in ρ_0, and thereby NLO in the effective range r_s, should be kept.

The leading two-body operator $\mathcal{O}_{2,4} = \psi_1^\dagger\psi_2^\dagger\psi_2\psi_1$ has been calculated in the zero-range model in Ref. [20] and in the field-theoretical two-channel model at a narrow Feshbach resonance [59]. The matrix element for this operator in this approach is

$$\langle \mathcal{O}_{2,4} \rangle = (1 + i\mathcal{I}_0\,\mathcal{A}(E))^2 + i\mathcal{A}_{\rho'}(1 + i\mathcal{I}_0\,\mathcal{A}_\lambda)\big[2\mathcal{I}_2 + (\boldsymbol{p}^2 + \boldsymbol{k}^2 - 4mE)\mathcal{I}_0\big]\,. \tag{2.58}$$

Multiplying by a factor of λ_0^2, the operator giving renormalized results $\lambda_0^2\psi_1^\dagger\psi_2^\dagger\psi_2\psi_1$ was obtained, as in Refs. [20, 59]. We also obtain the NLO renormalized operator in this study,

and it is given by

$$\begin{aligned}\langle \mathcal{O}_{2,4}^{(\mathrm{ren})} \rangle &= \Big\langle \lambda_0^2 \Big(1 + \frac{m\rho_0 \Lambda^3}{3\pi^2}\Big) \mathcal{O}_{2,4} \Big\rangle \\ &= m^2 \mathcal{A}^2(E) + 2m\lambda_0 \mathcal{A}_\rho - i(\boldsymbol{p}^2 + \boldsymbol{k}^2 - 2mE) m^2 \rho_0 \mathcal{I}_0 \mathcal{A}_\lambda^2 \\ &= m^2 \mathcal{A}^2(E) + O(\Lambda^{-2}) \,, \end{aligned} \tag{2.59}$$

where the LS equation of Eq. (2.44) was used to eliminate $1 + i\mathcal{I}_0 \mathcal{A}_\lambda$ in favor of $-m\mathcal{A}_\lambda/\lambda_0$. In Eq. (2.59), the terms $\sim 1/\Lambda^2$ are dropped. Note also that the operator $\mathcal{O}_{2,4}^{(\mathrm{ren})}$ is in fact $\mathcal{O}_C$, the operator associated with the contact density.

This can then be compared with the third term proportional to r of Eq. (2.46), and by doing so we find that the Wilson coefficient for this operator is

$$W_{2,4} = -\frac{r}{8\pi} + \frac{r_s}{8\pi} \,, \tag{2.60}$$

where the term proportional to the effective range r_s is necessary to cancel the term proportional to r_s in Eq. (2.48), as mentioned above. For $\mathcal{O}_{1,3}$, note that the renormalization was not written as $\mathcal{O}_{1,3}^{(\mathrm{ren})} = \mathcal{O}_{1,3} + \frac{r_s}{8\pi}\lambda_0^2 \mathcal{O}_{2,4}$ because the matrix element $\langle \mathcal{O}_{1,3} \rangle$ is finite and contains no explicit cutoff dependence. Thus, renormalization is not the proper method to eliminate the spurious r_s-dependent term in $\langle \mathcal{O}_{1,3} \rangle$. And yet, this term must be canceled because the nonlocal matrix element on the LHS of the OPE has no such r_s-dependence, so we use the Wilson coefficient $W_{2,4}$ to accomplish this through adding the term in Eq. (2.60) with r_s in its numerator.

For the two-body operator of dimension $\Delta = 5$ given by $\mathcal{O}_{2,5} = \psi_1^\dagger \psi_2^\dagger \psi_2 \overleftrightarrow{\partial_i} \psi_1 + \mathrm{H.c.}$, the matrix element is simplified by the fact that $\mathcal{I}_{2n}^{(2,5)} = 0$ and is

$$\begin{aligned}\langle \mathcal{O}_{2,5} \rangle =& 2i(p_i + k_i)[1 + i\mathcal{I}_0 \, \mathcal{A}(E)] \\ & - 2\mathcal{A}_{\rho'} \Big\{ (p_i + k_i)\mathcal{I}_2 + [p_i(\boldsymbol{k}^2 - 2mE) + k_i(\boldsymbol{p}^2 - 2mE)]\mathcal{I}_0 \Big\} \,. \end{aligned} \tag{2.61}$$

Table 2.2 – Two-body Operators

Δ	$\mathcal{O}_{2,\Delta}$	$W_{2,\Delta}$
4	$\psi_1^\dagger \psi_2^\dagger \psi_2 \psi_1^{(\mathrm{ren})}$	$-\frac{r-r_s}{8\pi}$
5	$\psi_1^\dagger \psi_2^\dagger \psi_2 \overleftrightarrow{\partial_i} \psi_1^{(\mathrm{ren})} + h.c.$	0
6	$\psi_1^\dagger \psi_2^\dagger \psi_2 \overleftrightarrow{\nabla}^2 \psi_1^{(\mathrm{ren})} + h.c.$	$-\frac{r^3}{384\pi}$

Two-body operators $\mathcal{O}_{2,\Delta}$ up to scaling dimension 6 and their Wilson coefficients.

The renormalization of the operator is accomplished through the inclusion of a multiplicative factor:

$$\begin{aligned}\langle \mathcal{O}_{2,5}^{(\mathrm{ren})} \rangle &= \langle \lambda_0 \Big(1 + \frac{m\rho_0 \Lambda^3}{6\pi^2}\Big) \mathcal{O}_{2,5} \rangle \,, \\ &= -2i(p_i + k_i) m \mathcal{A}(E) + O(\Lambda^{-2}) \,. \end{aligned} \tag{2.62}$$

Because this matrix element does not correspond to any part of the RHS of Eq. (2.46), its Wilson coefficient is $W_{2,5} = 0$.

Next, we define the operator $\psi_1^\dagger \psi_2^\dagger \psi_2 \overleftrightarrow{\partial_i} \overleftrightarrow{\partial_j} \psi_1 + \mathrm{H.c.}$ as $\mathcal{O}_{2,6}$ when contracted with δ_{ij} such that it can be matched to the terms in the nonlocal operator matrix element of Eq. (2.46). The result obtained is

$$\begin{aligned}\langle \mathcal{O}_{2,6} \rangle &= -4(1 + i\mathcal{I}_0 \mathcal{A}(E))(\boldsymbol{p}^2 + \boldsymbol{k}^2 + 2i\mathcal{I}_2 \mathcal{A}(E)) \\ &- 4i\mathcal{A}_{\rho'} \Big\{ 2(1 + i\mathcal{I}_0 \mathcal{A}_\lambda)\mathcal{I}_4 + (\boldsymbol{p}^2 + \boldsymbol{k}^2 + 2i\mathcal{I}_2 \mathcal{A}_\lambda)\mathcal{I}_2 \\ &\qquad + (\boldsymbol{p}^2 + \boldsymbol{k}^2 - 4mE)(1 + 2i\mathcal{I}_0 \mathcal{A}_\lambda)\mathcal{I}_2 \\ &\qquad + [\boldsymbol{p}^2(\boldsymbol{k}^2 - 2mE) + \boldsymbol{k}^2(\boldsymbol{p}^2 - 2mE)]\mathcal{I}_0 \Big\} \,. \end{aligned} \tag{2.63}$$

For the renormalization of the operator $\mathcal{O}_{2,6}$, we use momentum-dependent operators, and this dimension $\Delta = 6$ operator is considered in the on-shell limit in which $\boldsymbol{p}^2 = \boldsymbol{k}^2 = mE$.

This allows us to avoid energy-dependent operators in the renormalization process.

$$\langle \mathcal{O}_{2,6}^{(\mathrm{ren})} \rangle = \left\langle \lambda_0^2 \left(1 + \tfrac{3}{2}x\right) \mathcal{O}_{2,6} - \left[\frac{4\lambda_0^3 \Lambda^3}{3\pi^2} (1+2x) + \frac{12\lambda_0^2 \Lambda^2 x}{5} \right] \mathcal{O}_{2,4} \right\rangle \tag{2.64}$$

$$= -\,8mE\, m^2 \mathcal{A}^2(E) + O(\Lambda^{-2})\,, \tag{2.65}$$

where $x = \frac{\rho_0 m \Lambda^3}{3\pi^2}$. The operators C and D corresponding to the contact and derivative contact in Eq. (2.16) are related to the renormalized two-body operators as follows:

$$\mathcal{O}_{2,4}^{(\mathrm{ren})} = \mathcal{O}_C\,, \tag{2.66}$$

$$\mathcal{O}_{2,6}^{(\mathrm{ren})} = -4\mathcal{O}_D\,. \tag{2.67}$$

These equalities are valid when the factors of ρ_0 are dropped in Eq. (2.64). This is possible in this case because there is already a factor of this coupling constant in the Hamiltonian, and here the problem is only treated to NLO in the range r_s, which ρ_0 is proportional to. Next, Eq. (2.64) is compared to the final term $\propto r^3$ found in Eq. (2.46), and the Wilson coefficient corresponding to this operator to be

$$W_{2,6} = -\frac{r^3}{384\pi}\,. \tag{2.68}$$

A summary of the two-body Wilson coefficients for operators of dimension $\Delta = 4..6$ is contained in Table 2.2.

These results are generalizable to a two-body system with center-of-mass momentum $\boldsymbol{K}$. The relative momentum of the two particles remains $\pm\boldsymbol{p}$, and the single particle momentum can therefore be expressed as $\boldsymbol{K}/2 \pm \boldsymbol{p}$. In addition to this shift of $\boldsymbol{K}/2$ in the single-particle momentum, the total energy E must be replaced by the Galilean invariant energy $E - K^2/4m$. This momentum boost results in a multiplicative factor of $e^{i\boldsymbol{K}\cdot\boldsymbol{r}/2}$ in Eq. (2.45) and is reproduced in the OPE by the appropriate factors. The results in Table 2.1 may be written in a compact form using $\psi_\sigma^\dagger e^{\boldsymbol{r}\cdot\overleftrightarrow{\partial}/2}\psi_\sigma$ to reproduce this boost-related factor. Results can be adjusted in the two-body sector to account for a finite center-of-mass momentum by including the two-body operator $\psi_1^\dagger \psi_2^\dagger \psi_2 e^{\boldsymbol{r}\cdot\overleftrightarrow{\partial}'/2}\psi_1$ instead of $\mathcal{O}_{2,4}$. In this new two-body

operator, $\overleftrightarrow{\partial_i'} = \overrightarrow{\partial_i} + \overleftarrow{\partial_i}$. The exponential of the new operator can be expanded in small r, and the two resulting new operators up to scaling dimension $\Delta = 6$ are defined as

$$\begin{aligned}
\mathcal{O}'_{2,5} &= 2i\, \psi_1^\dagger \psi_2^\dagger \psi_2 \overleftrightarrow{\partial_i'} \psi_1^{(\mathrm{ren})}\,, \\
\mathcal{O}'_{2,6} &= -\tfrac{1}{2} \psi_1^\dagger \psi_2^\dagger \psi_2 \overleftrightarrow{\partial_i'} \overleftrightarrow{\partial_j'} \psi_1^{(\mathrm{ren})}\,.
\end{aligned}$$

Here, the Wilson coefficients are in a sense trivial to determine, since once the correct factors from the definitions of $\mathcal{O}'_{2,5}$ and $\mathcal{O}'_{2,6}$ are included, the coefficient $W_{2,4}$ is used.

2.4.3 Momentum distribution and Hamiltonian

Once all of the results from matching the one- and two-body matrix elements to the nonlocal matrix element given in Eq. (2.46) are obtained, we write the momentum-space momentum distribution as

$$\begin{aligned}
\rho_\sigma(\boldsymbol{k}) &= \int_{\boldsymbol{R}} \int_{\boldsymbol{r}} e^{i\boldsymbol{k}\cdot\boldsymbol{r}} \langle \psi_\sigma^\dagger(\boldsymbol{R} - \boldsymbol{r}/2) \psi_\sigma(\boldsymbol{R} + \boldsymbol{r}/2) \rangle \\
&= \int_{\boldsymbol{R}} \Bigg\{ \delta_{\boldsymbol{k}} \langle \mathcal{O}_{1,3}(\boldsymbol{R}) \rangle - i \frac{\nabla_{k_i} \delta_{\boldsymbol{k}}}{2} \langle \mathcal{O}_{1,4}(\boldsymbol{R}) \rangle - \frac{\nabla_{k_i} \nabla_{k_j} \delta_{\boldsymbol{k}}}{8} \langle \mathcal{O}_{1,5}^{(\mathrm{ren})}(\boldsymbol{R}) \rangle \\
&\qquad + i \frac{\nabla_{k_i} \nabla_{k_i} \nabla_{k_k} \delta_{\boldsymbol{k}}}{48} \langle \mathcal{O}_{1,6}(\boldsymbol{R}) \rangle + \left(\frac{1}{k^4} + r_s \frac{\delta_{\boldsymbol{k}}}{8\pi} \right) \langle \mathcal{O}_C(\boldsymbol{R}) \rangle + \frac{1}{k^6} \langle \mathcal{O}_D(\boldsymbol{R}) \rangle \\
&\qquad + \left(\frac{\hat{k}_i}{k^5} - r_s \frac{\nabla_{k_i} \delta_{\boldsymbol{k}}}{32\pi} \right) \langle \mathcal{O}'_{2,5}(\boldsymbol{R}) \rangle + \left(\frac{6\hat{k}_i \hat{k}_j - \delta_{ij}}{k^6} + r_s \frac{\nabla_{k_i} \nabla_{k_j} \delta_{\boldsymbol{k}}}{32\pi} \right) \langle \mathcal{O}'_{2,6}(\boldsymbol{R}) \rangle \Bigg\}\,,
\end{aligned} \tag{2.69}$$

where $\delta_{\boldsymbol{k}} = (2\pi)^3 \delta^{(3)}(\boldsymbol{k})$, and the unit vector $\hat{k}_i = k_i/k$. In Eq. (2.69), the second and third terms in the second line within the braces correspond to the contact C and derivative contact D of Eq. (2.16). In the last line, the term proportional to $1/k^6$ is related to the center of mass parameter $C' = \int_{\boldsymbol{R}} \delta_{ij} \langle \mathcal{O}'_{2,6}(\boldsymbol{R}) \rangle$ in Eq. (2.16) once the angular average is taken over the vector $\boldsymbol{k}$. The term in the last line that is proportional to $1/k^5$ vanishes after the same angular averaging takes place.

Then, in order to derive the energy relation given by Eq. (2.17), the Hamiltonian in the absence of any external potential is rewritten using terms in the Lagrangian seen in Eqs. (2.6) and (2.7) and given as $H = H_0 + H_I$. These are given by

$$\begin{aligned} H_0 &= \int_{\boldsymbol{R}} \Big[\mathcal{T}(\boldsymbol{R}) + \frac{\lambda_0}{m} \mathcal{O}_{2,4}(\boldsymbol{R}) \Big] , \\ H_1 &= \int_{\boldsymbol{R}} \Big[\frac{-\rho_0}{4} \mathcal{O}_{2,6}(\boldsymbol{R}) + \frac{\delta\lambda_0}{m} \mathcal{O}_{2,4}(\boldsymbol{R}) \Big] . \end{aligned} \tag{2.70}$$

The operators in these two parts of the Hamiltonian must then be rewritten in terms of the operators appearing in Eq. (2.16), and the result is

$$H_0 = \int_{\boldsymbol{R}} \left[\mathcal{T} + \frac{\mathcal{O}_C}{4\pi m a} - \left(\frac{\Lambda}{2\pi^2 m} + \frac{\rho_0 \Lambda^3}{3\pi^2 \lambda_0} \right) \mathcal{O}_C \right] ; \tag{2.71}$$

$$H_1 = \int_{\boldsymbol{R}} \frac{\rho_0}{\lambda_0^2} \mathcal{O}_D = \int_{\boldsymbol{R}} \frac{1}{16\pi m} \left(r_s - \frac{4}{\pi\Lambda} \right) \mathcal{O}_D \, . \tag{2.72}$$

The three different operators appearing in Eq. (2.71) are

$$\mathcal{T}(\boldsymbol{R}) \equiv \frac{1}{2m} \sum_\sigma \nabla \psi_\sigma^\dagger \cdot \nabla \psi_\sigma \, , \tag{2.73}$$

$$\mathcal{O}_C(\boldsymbol{R}) \equiv \mathcal{O}_{2,4}^{(\mathrm{ren})} = \lambda_0^2 \Big(1 + \frac{m\rho_0\Lambda^3}{3\pi^2} \Big) \mathcal{O}_{2,4} \, , \tag{2.74}$$

$$\mathcal{O}_D(\boldsymbol{R}) \equiv -\frac{\mathcal{O}_{2,6}^{(\mathrm{ren})}}{4} = -\frac{\lambda_0^2}{4} \Big[\mathcal{O}_{2,6} - \frac{4\lambda_0\Lambda^3}{3\pi^2} \mathcal{O}_{2,4} \Big] + O(\rho_0) \, . \tag{2.75}$$

Here, λ_0 and ρ_0 are the bare coupling constants appearing in the Lagrangian and are related to the scattering length and effective range as shown in Eqs. (2.11) and (2.14). In Eq. (2.75), we drop the terms proportional to ρ_0 appearing in the definition of $\mathcal{O}_{2,6}^{(\mathrm{ren})}$ because a factor of ρ_0 already multiplies the derivative contact operator found in the finite range part of the Hamiltonian of Eq. (2.72), and terms proportional to ρ_0^2 ought to be dropped in the NLO calculation as mentioned previously. Using Eq. (2.14), the portion of the Hamiltonian given by H_1 is broken up into a term proportional to $r_s \mathcal{O}_D$ and another proportional to $\frac{1}{\Lambda} \mathcal{O}_D$.

The last term in the square brackets of Eq. (2.75) is present to subtract the divergent part of the matrix element $\langle \mathcal{O}_D \rangle$ to yield a finite, physical result. This fulfills the same

purpose as the $\delta\lambda_0$ in the Lagrangian of Sec. 2.1. Comparison of $\mathcal{O}_D$ and $\mathcal{O}_{2,6}^{(\mathrm{ren})}$ reveals that $\frac{\rho_0}{\lambda_0^2}\mathcal{O}_D$ and $\frac{-\rho_0}{4\lambda_0^2}\mathcal{O}_{2,6}^{(\mathrm{ren})}$ give the same result in the Hamiltonian.

The subtracted term corresponding to the kinetic energy of the gas, $T^{(\mathrm{sub})}$, in Eq. (2.17) is defined by absorbing the explicit cutoff dependence found in H_0 and H_1 into this kinetic term as

$$\langle T^{(\mathrm{sub})}\rangle = \int_{\boldsymbol{R}} \left\langle \mathcal{T} - \frac{1}{2\pi^2 m}\left[\Lambda\Big(1+\tfrac{2m\rho_0\Lambda^2}{3\lambda_0}\Big)\mathcal{O}_C + \frac{\mathcal{O}_D}{2\Lambda}\right]\right\rangle. \tag{2.76}$$

$T^{(\mathrm{sub})}$ contains terms that are proportional to the contact operator multiplied by Λ and also by Λ^3 in order to subtract the divergent parts of $\int_{\boldsymbol{R}}\langle\mathcal{T}\rangle$. The term proportional to $\frac{1}{\Lambda}\mathcal{O}_D$ is present in order to remove the remaining cutoff dependence.

2.5 Conclusion and outlook for the OPE in systems of two-component fermions

In this chapter, we considered the operator product expansion of the nonlocal coordinate-space expression of the momentum distribution in terms of local operators of the effective field theory describing a two-component, homogeneous Fermi gas characterized by a large interparticle scattering length and small S-wave effective range. By making use of the results for the momentum distribution of a two-particle scattering state, the operators up to scaling dimension $\Delta = 6$ were matched to the nonlocal matrix element and the corresponding Wilson coefficients were obtained. A sharp UV cutoff was used in the EFT calculations, and corrections to the results due to a finite effective range were included.

The principal results of this study are extended universal relations containing the previously known contact C and the two quantities C' and D. In particular, it is the sum of these two new quantities that appears as the asymptote of the subleading $(C'+D)/k^6$ tail of the momentum distribution. The latter of these two quantities, the derivative contact D, appears in other universal relations characterizing the total energy and its derivative with respect to the range r_s, the pressure of the gas, and the virial theorem as an effective-range correction of the form $r_s D$. This subleading tail was first discussed by Werner and Castin in

Ref. [52], as was the relation of this quantity to the energy. These results were reproduced by utilizing the OPE in this study.

Interestingly, while effective-range corrections to various observables are typically reduced by a factor of r_s/a, the size of D is not itself suppressed in this manner in comparison to the size of C. As an example, the QMC simulation of Ref. [57] obtained a value for the derivative contact density $\mathcal{D}/k_F^6 \approx 0.06$ in the unitary limit, whereas the value for the contact density in the same limit is $\mathcal{C}/k_F^4 \approx 0.11$. In the BEC limit, in which the scattering length approaches zero from positive infinity, the derivative contact becomes more important than the contact because the former scales as $1/(k_F a)^3$, while the latter scales as $1/(k_F a)$ in this limit. The result for the tail of the momentum distribution given in this work, even in the absence of a known value for $\mathcal{C}'$, gives a noticeable improvement in the theoretical description of the numerical many-body data for the same quantity in the region where $k \gtrsim 1.5k_F$ as demonstrated in Fig. 2.4. The NLO contribution $\mathcal{D}/k^6$ gives a correction to the momentum distribution of around 20% near $1.5k_F$ in the unitary limit.

These various results are the first step in a broader effort to calculate range-corrected universal relations for other observables such as the single-particle dispersion relation, structure factors, and rf spectroscopy. An interesting further application of this work would be to a system of fermions in three distinguishable states, in which a three-body operator leads to the Efimov effect and a $1/k^5$ tail is present in the momentum distribution for the large, imbalanced mass ratio $m_1/m_2 > 13.6$ [78]. Further, range-corrected universal relations in a system of three identical bosons [79] would be interesting to examine. We have not discussed the *pair density* or inelastic two-body scattering [20] here, but these topics would constitute interesting further applications of the work we have presented in this chapter.

Chapter 3

Efimov Effect in Heteronuclear Three-body Systems

In the balanced, homogeneous gas of fermions in two spin states considered above, three particles were not allowed to come into contact because of the Pauli exclusion principle. However, if the statistics of the system are changed such that it contains fermions in three spin states, or one bosonic species, or more than one species of bosons or fermions or a mixture of the two interacting through a large scattering length, three-body interactions can occur which lead to very interesting universal physics. The resulting system-independent phenomena have been considered in nuclei [3] and in gaseous mixtures of atoms [80, 81]. This field has generally come to be described as Efimov physics [3, 82], in which there is a discrete scaling of observables referred to as the Efimov effect. An example of this discrete scaling is that there exists an infinite sequence of three-body bound states in the unitary limit separated by a scaling factor which we denote λ as one approaches the three-atom binding threshold at zero energy from negative infinity. The observables we consider in this chapter also exhibit such a discrete scaling.

Such discrete scaling is of interest in nuclear physics, but it is often studied in the context of ultracold atoms because there it is possible to utilize a Feshbach resonance [83] to tune an inter-atomic scattering length to an unnaturally large value in order to access universal physics, in which the range of the underlying inter-atomic potential and the detailed substructure of the interacting particles are not important. Occasionally, such universal

behavior results from an accidental fine-tuning of the scattering length by nature, such as in a gas of ^{4}He atoms [1]. In this work, we explore universal physics in a system consisting of a heteronuclear mixture of small-mass-number fermions and heavier bosonic particles in which the interspecies scattering length between a light fermion and a heavy boson has been tuned to be much larger than either of the intraspecies scattering lengths and any of the underlying interaction ranges. The fermionic particles, for the purposes of this study, are assumed to be prepared in one spin state, which is an experimentally realizable assumption. Such systems, as well as those in which the light atom is a boson, have been of recent experimental interest [38, 80, 84, 85].

One of the universal features of the system we consider is the three-body recombination process whereby two heavy bosonic atoms and one light fermionic atom scatter into a recoiling heavy atom and a shallow-bound diatomic molecule consisting of one fermion and one boson. This is possible when the interspecies scattering length is large and positive. The rate at which this recombination process occurs is calculated below and generalized for finite-temperature gases. The temperature dependence of the recombination rates were calculated using universal functions of dimensionless scaling variables, which parameterize the energy dependence of the scattering matrix. We compared the results of this study to experimental data for the ^{40}K-^{87}Rb system [38] and made a prediction for the ^{6}Li-^{87}Rb mixture. The method presented may be readily applied to heteronuclear systems of atoms of masses not included here. An additional process known as atom-diatomic molecule *relaxation* occurs when the three-body energy is between the atom-diatomic molecule threshold and the three-atom threshold for a positive interspecies scattering length, and we calculate the rate at which this occurs at finite temperature and again compare with the data of Ref. [38].

In order to study three-body recombination in heteronuclear mixtures, we have made use of the Skorniakov–Ter-Martirosian (STM) integral equation [86] originally used to describe neutron-deuteron scattering, but which has more recently been applied to low-energy atom-diatomic molecule (AD) scattering [87, 88]. This allows the calculation of AD scattering amplitudes and phase shifts for a given value of orbital angular momentum L. These phase shifts are then related to universal scaling functions that parameterize the energy-dependent three-body recombination rates in Sec. 3.3. In the orbital angular momentum

$L = 0$ scattering channel, the relationship between the phase shifts and the scaling functions and three-body parameters of the system is known as Efimov's radial law. Once the recombination rate is known for each L, they are summed, and we calculate the temperature-dependent rate constant as a function of the scattering length by taking a Boltzmann average over the energy-dependent recombination rates at each value of the scattering length. Lastly, we compare our results with experimental data in Sec. 3.4.

3.1 The STM Equation

The Lagrangian density that has been given earlier in Eq. (2.5) may also be applied to the three-body scattering sector. To do so, Bedaque, Hammer, and van Kolck discovered that it is necessary to include a single three-body interaction counterterm in the Lagrangian in order to properly renormalize the scattering amplitude [13]. The corresponding Lagrangian density for a system of two distinguishable species is

$$\begin{aligned}\mathcal{L} =&\psi_1^\dagger \left(i\partial_t + \frac{\nabla^2}{2m_1} \right) \psi_1 + \psi_2^\dagger \left(i\partial_t + \frac{\nabla^2}{2m_2} \right) \psi_2 \\ &+ g_2 d^\dagger d - g_2 \left(d^\dagger \psi_1 \psi_2 + \psi_1^\dagger \psi_2^\dagger d \right) - \frac{g_3}{4} d^\dagger d \psi_2^\dagger \psi_1 + \cdots ,\end{aligned} \tag{3.1}$$

where subscripts 1 and 2 indicate particles of species 1 and 2 and g_2 and g_3 are the bare two- and three-body coupling constants. In Eq. (3.1), d is an auxiliary field for a diatomic molecule consisting of one particle of species 1 and one of species 2. The approach including this auxiliary field is often referred to as the "dibaryon" formalism and is more useful in developing the STM equation in this EFT framework [13] than writing the theory only in terms of fields corresponding to individual atoms. The first two terms of this Lagrangian density are the kinetic terms for the atoms of each species. The third term corresponds to the kinetic energy of the non-dynamical auxiliary field d. The last two terms generate the S-wave contact interactions between two dissimilar particles and the three-body interaction. Higher order terms containing more fields and their derivatives are indicated by the dots.

Though the systems of atoms in experiments relevant to this work are, in fact, many-body systems, many properties may be described by the physics of two and three interacting

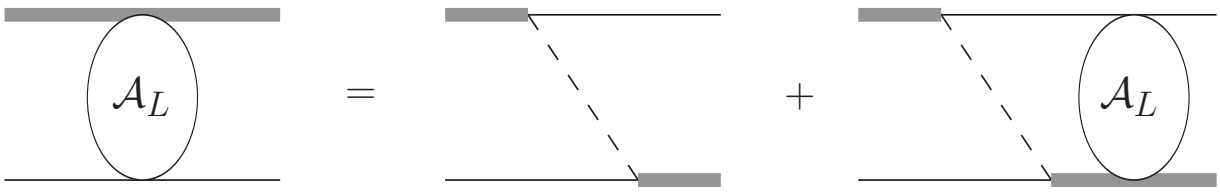

Fig. 3.1 – This diagram gives the integral equation for the elastic A_2D scattering amplitude for orbital angular momentum L. The solid black line indicates a particle of species 2, the dashed line a particle of species 1, and the thick line is a diatomic molecule composed of one particle of each species. Note that we have not included a three-body force.

bodies. The particular three-atom system considered here is labeled as $(A_1A_2A_2)$. The two atoms A_1 and A_2 have masses m_1 and m_2, respectively, with $m_1 < m_2$. The interspecies S-wave scattering length is labeled a and is large and positive, but the scattering length between any identical atoms is negligible. The two atoms A_1 and A_2 can form a weakly bound diatomic molecule D which has binding energy $E_D = 1/2\mu a^2$, where the reduced mass $\mu = m_1m_2/(m_1 + m_2)$. For three-body energy E and orbital angular momentum L, the elastic scattering phase shift $\delta^{(L)}_{A_2D}(k_E)$ is given by

$$\mathcal{A}_L(k_E, k_E; E, \Lambda) = \frac{2\pi}{\mu_{A_2D}} \frac{1}{k_E \cot \delta^{(L)}_{A_2D}(k_E) - ik_E}\,, \tag{3.2}$$

where $\mu_{A_2D} = m_2(m_1+m_2)/(2m_2+m_1)$ is the A_2D reduced mass and $k_E = \sqrt{2\mu_{A_2D}(E + E_D)}$. In Eq. (3.2), Λ is the ultraviolet cutoff imposed on the problem. The on-shell scattering amplitude $A_J(k_E, k_E; E, \Lambda)$ can be determined by solving the STM equation in a modified form applicable to heteronuclear mixtures [41, 40].

In general, the amplitude is a function of the ingoing and outgoing relative momenta p and k, as well as the three-body energy E. The dependence of the amplitude on the UV cutoff Λ arises from the regularization of the integral term in the inhomogeneous STM equation

$$\begin{aligned}\mathcal{A}_L(p, k; E, \Lambda) =& \frac{2\pi m_1}{a\mu^2}(-1)^n M_L(p, k; E) + \frac{m_1}{\pi\mu}\int_0^\Lambda dq\, q^2 M_L(p, q; E) \\ &\times \frac{(-1)^n A_L(q, k; E, \Lambda)}{-1/a + \sqrt{-2\mu(E - q^2/2\mu_{A_2D}) - i\epsilon}}\,.\end{aligned} \tag{3.3}$$

As we discuss below, the cutoff dependence of the amplitude does not disappear for $L = 0$ as one increases Λ even though the amplitude remains finite, but it does disappear for $L \geq 1$. The integer n in Eq. (3.3) is equal to L when the heavy particle A_2 is a boson and $L + 1$ if the heavy particle is a fermion. This work examines the case wherein the heavy particles are bosonic, which is more relevant for current experiments. Equation (3.3) is also applicable to the three-body bound-state problem, albeit without the inhomogeneous term. In either case, the STM equation does not have a unique solution as the cutoff is taken to infinity for $L = 0$. This comes from the fact that we have approximated the interactions as pointlike. Further details on the derivation of the equivalent of Eq. (3.3) for the case of three identical bosons are given in Ref. [2]. We give the diagrammatic representation of Eq. (3.3) in Fig. 3.1.

In Eq. (3.3), the kernel function $M_L(p, q; E)$ can be interpreted as the potential mediating the exchange of the light atom in partial wave L from one of the two heavy atoms to the other. Its detailed form is given in momentum space by

$$M_L(p, q; E) = \frac{1}{pq} Q_L \left(\frac{p^2 + q^2 - 2\mu E - i\epsilon}{2pq\mu/m_1} \right) . \tag{3.4}$$

For a complex argument z, $Q_L(z)$ is the Legendre function of the second kind for partial wave L. These functions can be written in terms of Legendre polynomials as

$$Q_L(z) = \frac{1}{2} \int_{-1}^{1} dx \frac{P_L(x)}{z - x} . \tag{3.5}$$

Note that the kernel given by Eq. (3.4) does not contain a three-body force, unlike that of Ref. [13]. This is because we carry out the renormalization in a different way, which we detail below.

A few further clarifications about this theoretical framework are important to make at this time. First, it is notable that when $L \geq 1$, the solutions for the amplitude in Eq. (3.3) are independent of the cutoff Λ, and therefore so are the phase shifts obtained from Eq. (3.2). This is true as long as $m_2/m_1 < 38.63$, beyond which the D-wave Efimov effect enters [82, 89], and as long as $p, k, 1/a \ll \Lambda$ so that the theory is applicable. The results presented here are restricted by both of these assumptions.

As mentioned above, for $L = 0$, the amplitude in Eq. (3.3) does not converge as $\Lambda \to \infty$, though it does remain finite. To resolve this issue, one must take a three-body parameter as an input from experiments or first-principles calculations. It turns out that there is a linear relationship between the three-body parameter κ_* mentioned in the introduction and the UV cutoff. Alternatively, one may take the inverse of the location of a three-body recombination minimum a_{*0} as an input parameter. The recombination minimum may take any value of the scattering length for which there is a local minimum in the three-body loss rate. Experimentally, this can be found in atomic physics by tuning the magnetic field that the atoms are immersed in until a minimum in the three-body loss rate is observed. The relationship between the UV cutoff and three-body paramter results in a log-periodicity of the amplitude in the cutoff with a period equal to the system-dependent scaling factor λ shown in Eq. (1.1) [87, 13, 90]. The cutoff dependence of the amplitude emerges from the behavior of the amplitude in the region at and above the cutoff, where the EFT Lagrangian cannot be expected to be sufficient to describe the system reliably. In this work, by solving the STM equation for a variety of cutoff values Λ in the range $1/a \ll \Lambda_0 < \Lambda < \lambda\Lambda_0$ for a chosen Λ_0, we obtained a set of phase shifts $\delta^{(0)}_{A_2D}(k_E)$ corresponding to a set of a_{*0} values. Then, the Efimov radial law we define below is fit to these phase shifts to obtain universal scaling functions that are independent of the cutoff Λ and scale with $\sqrt{E/E_D}$ following the method of Ref. [39]. This is our alternative to the use of a three-body counterterm as described by Bedaque, Hammer, and van Kolck in Ref. [13] for the purpose of renormalization in the three-body problem. In either method of renormalizing the problem, a three-body input parameter is necessarily taken from experiments or a microscopic model.

The kernel given by Eq. (3.4) contains a branch cut in the complex q plane for energies higher than $E = 0$, namely the three-atom threshold. To avoid this problem we rotate the integration path clockwise into the fourth quadrant of the complex plane by an angle ϕ and integrate along a straight line from $q = 0 \to \Lambda e^{-i\phi}$ [91]. It is necessary to then integrate from that endpoint in the complex plane along an arc of length Λ back to the positive, real q axis in order to obtain correct amplitudes. In the solution of the STM equation, we first solve for the half-on-shell amplitude $\mathcal{A}(p, k_E; E, \Lambda)$, but must then iterate the integral equation one more time to obtain the fully on-shell amplitude needed for the phase shifts.

3.2 Recombination Rates and Scaling Functions

The three-atom system ($A_1A_2A_2$) with two atoms of species 2 with atomic number density n_2 and one atom of species 1 with number density n_1 can leave a shallow trap as an A_2D pair via a process called three-body recombination. This occurs when a heavy and light atom form a diatomic molecule and the third atom recoils, as energy must be conserved in the process. As such events happen in a gas, it is possible to measure a loss rate as atoms leave the trap they are contained in. The rate constant α is defined for this process as [41]

$$\frac{d}{dt}n_2 = 2\frac{d}{dt}n_1 = -2\alpha n_1 n_2^2. \tag{3.6}$$

When the three body energy is zero, the rate constant for recombination into a shallow diatomic molecular state of binding energy E_D can be obtained from the A_2D S-wave scattering amplitude [41, 92] and is given by

$$\alpha_s = 4\mu_{A_2D}\sqrt{\frac{\mu_{A_2D}}{\mu}}a^2\left|\mathcal{A}_0\left(0, \frac{1}{a}\sqrt{\frac{\mu_{A_2D}}{\mu}}; 0\right)\right|^2. \tag{3.7}$$

The dependence of Eq. (3.7) on the interspecies scattering length a can be written analytically [41] as

$$\alpha_s = C(\delta)\frac{\sin^2\theta_{*0} + \sinh^2\eta_*}{\sinh^2(\pi s_0 + \eta_*) + \cos^2\theta_{*0}}\frac{a^4}{m_1}\,, \tag{3.8}$$

where the dependence on the mass ratio $\delta = m_1/m_2$ is contained in the coefficient

$$C(\delta) = 64\pi^2\left[(1+\delta^2)\phi(\delta) - \sqrt{\delta(2+\delta)}\right]. \tag{3.9}$$

In Eq. (3.9), the phase $\phi(\delta) = \arcsin[(1+\delta)^{-1}]$. The scaling factor s_0 is the solution of the transcendental equation explained for identical bosons in Ref. [13]. For the heteronuclear case a modified equation is necessary, though its origins are similar to the bosonic case, and we take this from Ref. [41]:

$$s_0\cosh[\pi s_0/2]\sin[2\phi(\delta)] - 2\sinh[s_0\phi(\delta)] = 0\,. \tag{3.10}$$

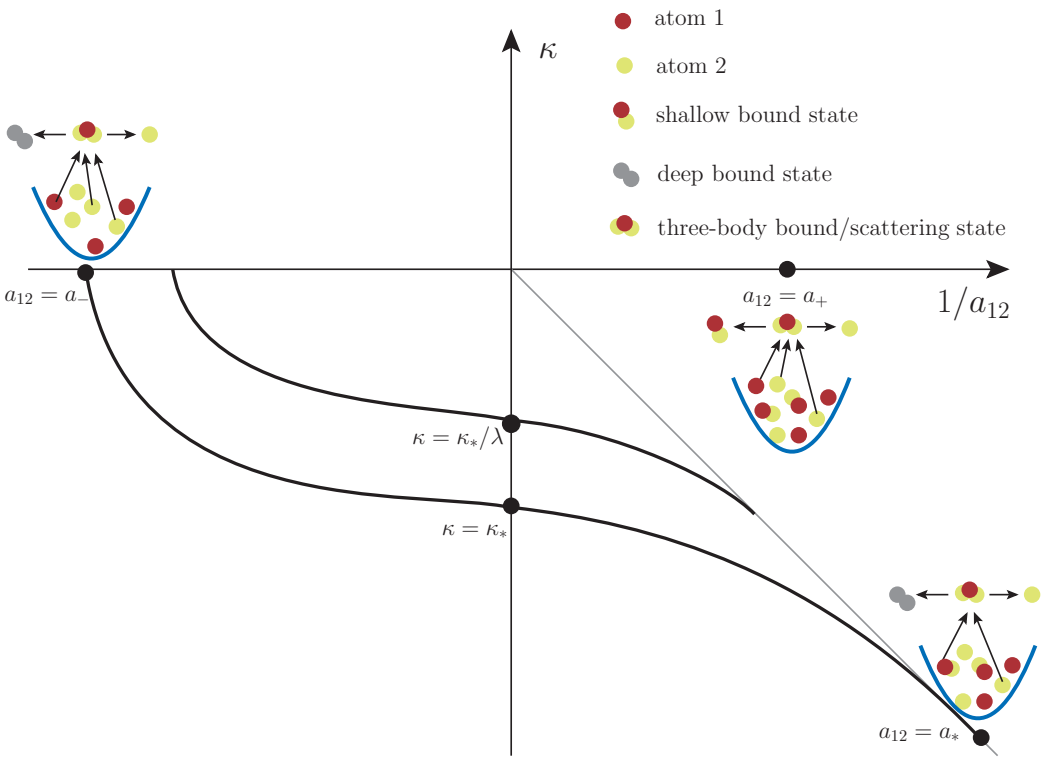

Fig. 3.2 – This plot provides a visualization of various universal features of the heteronuclear system. The solid lines represent universal three-body bound states at various values of the interspecies scattering length, and the solid dots in the figure represent the location of three-body parameter values. κ is the binding momentum of a universal three-body bound state and λ is the scaling factor separating such states, a_- is the location where the three-body state arrives at the three-atom threshold ($E = 0$), a_* is the location where the bound state intersects the atom-diatomic molecule threshold, and a_+ is written a_{*0} in this dissertation and indicates the location of a three-body recombination minimum. We thank Bijaya Acharya for providing this figure.

In Eq. (3.8), the angle θ_{*0} is given by

$$\theta_{*0} = s_0 \ln(a/a_{*0}), \tag{3.11}$$

where a_{*0} is the value of the scattering length a at the location of a local minimum in the three-body recombination rate, or a recombination minimum. A visualization of this three-body parameter and others is given in Fig. 3.2. The a-dependence in Eq. (3.11) results in a log-periodicity with respect to a in Eq. (3.8), with a period equal to the scaling factor $\lambda = e^{\pi/s_0}$. An additional parameter, η_*, is introduced in Eq. (3.8) and amounts to the introduction of an anti-Hermitian interaction term in the three-body Hamiltonian [93, 94],

allowing for an additional loss channel. This parameter modifies α_s to account for the formation of deeply bound diatomic molecular states occurring in experimental systems. These deeply bound states are characterized by binding energy $\sim 1/2\mu\ell^2$, where ℓ is the underlying interaction length, as opposed to the much more shallow bound state energy $1/2\mu a^2$ characterizing the shallow diatomic molecules.

The value of a_{*0} associated with a particular cutoff Λ is determined by fitting the expression in Eq. (3.8) to numerical results arrived at for a particular cutoff value using Eq. (3.7) for a range of a values after setting $\eta_* = 0$. This provides a value of a_{*0} for each Λ. Because a_{*0} is multivalued, our process amounts to tracking the location of a specific minimum as the cutoff is varied. By doing this, we get the proportional relationship we need between Λ and $1/a_{*0}$ in order to use a Λ-value in Eq. (3.3) that gives the scattering amplitude corresponding to three-body parameter a_{*0}. This is important because once we have a value of the three-body parameter, say from first principles calculations or from an experiment, we can use that to obtain the cutoff value we need to calculate the A_2D amplitude of Eq. (3.3), and thus the phase shift of Eq. (3.2) for $L = 0$. As we will see below, this will allow for the calculation of the three-body recombination rate.

While the introduction of the parameter η_* serves to lower the effect of recombination into a shallow diatomic molecule and recoiling atom, it leads to additional three-atom losses due to the formation of deeply bound diatomic molecules in the final state. The analytical expression for this rate contribution at the three-atom threshold is given by [41]

$$\alpha_d = C(\delta)\frac{\coth(\pi s_0)\cosh(\eta_*)\sinh(\eta_*)}{\sinh^2(\pi s_0 + \eta_*) + \cos^2\theta_{*0}}\frac{a^4}{m_1}\,. \tag{3.12}$$

This means that to calculate the maximum threshold recombination rate $\alpha_{\rm th}^{\rm max}$, we must sum the maxima of both the shallow and deep molecule rate constants. These maxima occur at $\theta_{*0} = \pi/2$, and their sum is

$$\alpha_{\rm th}^{\rm max} = C(\delta)\frac{1 + \sinh^2\eta_* + \coth(\pi s_0)\cosh(\eta_*)\sinh(\eta_*)}{\sinh^2(\pi s_0 + \eta_*)}\frac{a^4}{m_1}\,. \tag{3.13}$$

A helpful check of our S-wave three-body recombination rate at nonzero energy obtained from the amplitude we calculated for a particular value of the three-body parameter a_{*0} in

Eq. (3.3) can be performed using Eqs. (3.8), (3.12), and (3.13). The comparison is made when we take the limit $E \to 0$ of our recombination rate, where we ought to obtain the same result, up to a known factor, that Eq. (3.13) gives when we allow for the formation of both shallowly and deeply bound diatomic molecules.

An additional process may be observed if one prepares the cold-atomic system to only contain free atoms of species A_2 and diatomic molecules D. This is known as atom-diatomic molecule *relaxation*, in which an atom A_2 interacts with the shallowly-bound molecule D in such a way that the molecule relaxes into a deeply bound state and the atom and molecule recoil, enabling them to leave a shallow trap. A local maximum in the relaxation rate occurs where a three-body bound state contacts the A_2D threshold at scattering length $a = a_*$ (not to be taken as a_{*0}). This location is shown in Fig. 3.2 and corresponds to a resonant enhancement of the relaxation rate. This enhancement is present because there is a resonant connection of the atom and diatomic molecule with a trimer state at $a = a_*$ leading to a strong loss channel where the trimer decays into a free atom and deeply bound molecule. Helfrich, Hammer, and Petrov have developed an analytical expression describing the rate at which this relaxation occurs in heteronuclear mixtures [41], and at $E = 0$ the expression for the relaxation rate constant is

$$\beta_0(E=-0) = \frac{2\pi\mu^{3/2}}{\mu_{A_2D}^{3/2}} \frac{\sinh(2\pi s_0)\sinh(2\eta_*)}{\sinh^2(\pi s_0+\eta_*)+\cos^2[s_0\ln(a/a_{*0})]} \frac{a}{2\mu}\,. \tag{3.14}$$

In general, this S-wave relaxation rate for a particular value of a is given by

$$\beta(E) = \frac{k_E}{\mu_{A_2D}} \sigma_{A_2D}^{(\mathrm{inel})}(E)\,, \tag{3.15}$$

where the inelastic cross section in Eq. (3.15) is given in Appendix B by Eq. (B.3). This process only occurs when the inelasticity parameter is non-zero since it requires the formation of deep diatomic molecules. In order to obtain correct results, one must integrate in the STM equation along the same integration path described previously, but one must analytically continue the cutoff as $\Lambda \to \Lambda e^{i\eta_*/s_0}$ [41].

3.3 Three-body recombination and universal scaling functions

The three-body recombination rate is given by $K_3^{(L)}(E)$ at energy E, and it is related to the inelastic $A_1A_2A_2 \to A_2D$ S matrix. Equation (3.3) only involves the amplitude for elastic $A_2D \to A_2D$ scattering, but this problem may be circumvented using the unitarity of the total S matrix to access this inelastic part, and in this work the recombination rate will therefore be written purely in terms of the S matrix for elastic A_2D scattering. This can be written $S^{(L)}_{A_2D,A_2D}(E) = \exp[2i\delta^{(L)}_{A_2D}(E)]$ [39]. Further, we found that the recombination rate for the heteronuclear mixture addressed here is given as

$$K_3^{(L)}(E) = \frac{128\pi^2\mu^{3/2}}{\mu_{A_2D}^{3/2}} \frac{2L+1}{x^4} \left[1 - \left|S^{(L)}_{A_2D,A_2D}(E)\right|^2\right] \frac{a^4}{2\mu}\,, \tag{3.16}$$

where the scaling variable $x = \sqrt{E/E_D}$ is dimensionless. This describes the process fully in the absence of deeply bound molecules, but these are taken into account later in this section. A detailed derivation of Eq. (3.16) is given in Appendix B. The differences between three-body recombination when $L = 0$ and when $L \geq 1$ can now be made plain.

3.3.1 Orbital Angular Momentum $L \geq 1$

There is a real-valued scaling function of the dimensionless scaling variable x corresponding to each total orbital angular momentum $L \geq 1$ given by

$$f_L(x) = 1 - e^{-4Im\,\delta^{(L)}_{A_2D}(E)}\,. \tag{3.17}$$

Once the phase shifts for A_2D scattering in partial wave L have been obtained using Eqs. (3.2) and (3.3) above, we are ready to incorporate Eq. (3.17) into the formula for the recombination rate and obtain the contribution from the L^{th} partial wave to the total rate. In general, only the first few partial waves contribute to the recombination rate, and for identical bosons the $L = 0$ channel dominates the higher partial waves. However, in heteronuclear mixtures, the amplitudes from higher partial waves can dominate the total recombination rate for

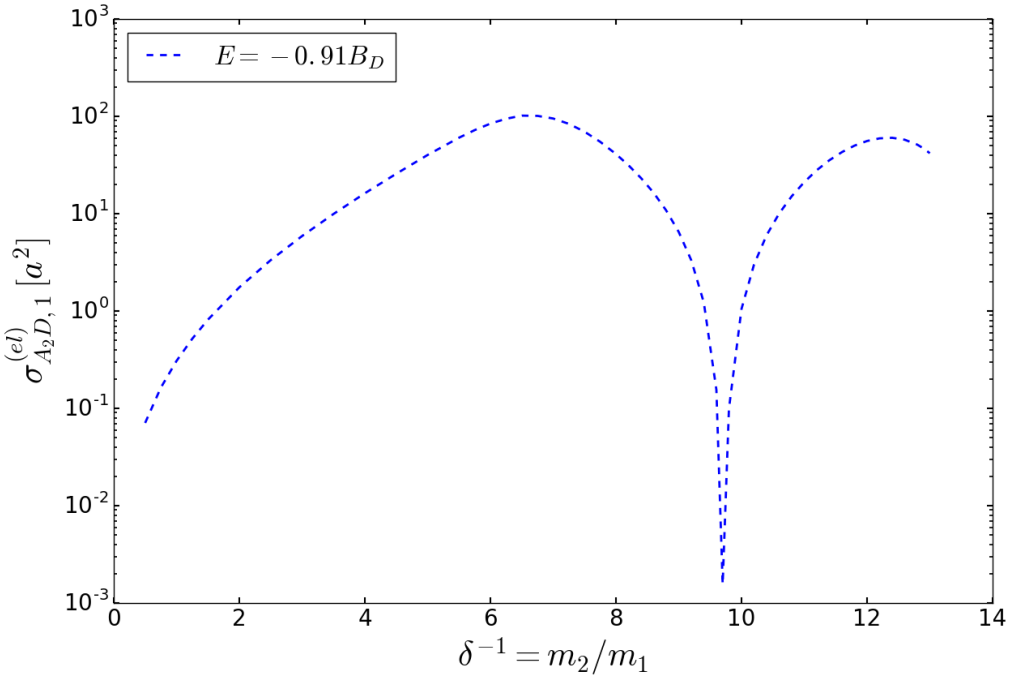

Fig. 3.3 – We reproduce one of the curves in Fig. 4 of Ref. [40] when the heavy particle species is fermionic and $E = -0.91B_D$, where B_D is the diatomic molecular binding energy. This value is chosen because it approaches the A_2D threshold, where the two peaks visible in the curve become more pronounced. The two peaks in the plot indicate the presence of two three-body P-wave bound states. These states do not exhibit the universal scaling discussed in this section. However, Efimov physics is observed in the $L = 1$ channel when the mass ratio is above $\delta_c^{-1} \approx 13.61$.

experimentally relevant temperatures, especially as the mass ratio $\delta = m_1/m_2$ decreases. Further, as we calculate the phase shifts for higher partial waves, it becomes increasingly difficult to achieve numerical accuracy in $f_L(x)$ at small values of x, so it is necessary to use the approximate form

$$f_L(x) \approx a_L x^{2\lambda_L+4} + b_L x^{2\lambda_L+6} \tag{3.18}$$

for small x, where $\lambda_L = L$ [39, 95]. The coefficients a_L and b_L are obtained by fitting Eq. (3.18) to data for $f_L(x)$ at the lowest x values that still have small numerical uncertainties. We then incorporate these $L \geq 1$ partial wave scaling functions into the

following equation for the energy-dependent three-body recombination rate $K_3^{(L\geq 1)}$:

$$K_3^{(L\geq 1)}(E) = \frac{128\pi^2\mu^{3/2}}{\mu_{A_2D}^{3/2}} \frac{(2L+1)f_L(x)}{x^4} \frac{a^4}{2\mu} \,. \tag{3.19}$$

We note that this equation contains no dependence on the three-body parameter a_{*0} because the STM equation of Eq. (3.3) has a unique solution for each $L \geq 1$. Thus, there is no discrete scaling to be observed in three-body recombination in these higher-partial-wave scattering channels.

As an additional test of our method for $L \geq 1$, we calculate the elastic atom-diatomic molecule scattering cross section $\sigma_{A_2D,L}^{(\mathrm{el})}$ at zero energy as a function of m_2/m_1 for the case when species 2 is bosonic and reproduce the corresponding solid curve in Fig. 3 of Ref. [40]. We also exactly reproduce the behavior of the P-wave cross section of Fig. 4 in the same reference below the critical mass ratio $\delta_c^{-1} \approx 13.61$ for the case in which the heavy particles are fermions. That plot indicates there are two universal three-body bound states in this region of mass ratios [40], and we reproduce the curve at energy $E = -0.91B_D$ in Fig. 3.3.

3.3.2 Angular momentum $L = 0$

The $L = 0$ scattering channel has some additional properties that make it more interesting than the $L \geq 1$ channels, and these properties are detailed in this section. It is this scattering channel in which the solution to the heteronuclear STM equation of Eq. (3.3) is non-unique, but is instead log-periodic as the cutoff is varied for a given interspecies scattering length. Proceeding to eliminate this log-periodicity and obtain $L = 0$ phase-shifts related to a known three-body parameter correctly, we note that in addition to being related to scattering phase shifts as seen above Eq. (3.16), S matrix elements for elastic A_2D scattering are related to universal functions s_{ij} of the dimensionless scaling variable x via Efimov's radial law [2]. This gives

$$S_{A_2D,A_2D}^{(L=0)}(E) = s_{22}(x) + \frac{s_{21}(x)^2 e^{2i\theta_{*0}-2\eta_*}}{1 - s_{11}(x)e^{2i\theta_{*0}-2\eta_*}} \,. \tag{3.20}$$

We obtain complex-valued scaling functions $s_{ij}(x)$ by first setting η_* to zero for the purposes of a fit and then fitting the RHS of Eq. (3.20) for each x to the numerical S matrix

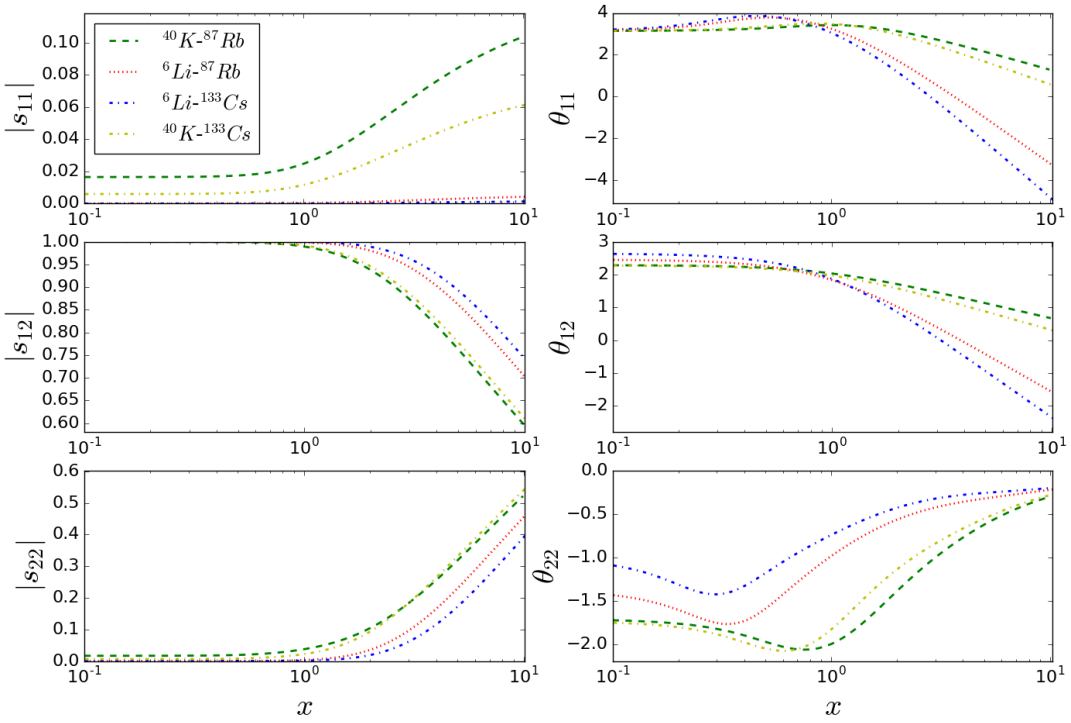

Fig. 3.4 – S-wave universal functions for ^{40}K-^{87}Rb, ^{6}Li-^{87}Rb, ^{40}K-^{133}Cs, and ^{6}Li-^{133}Cs. We present them as functions of universal scaling variable $x = \sqrt{E/E_D}$, and they parameterize all of the non-universal physics of their respective heteronuclear system. They are valid regardless of the details of the underlying interaction potential in the system.

element related to phase shift values acquired with Eqs. (3.2) and (3.3) for the range of a_{*0} values corresponding to a varied set of Λ-values as discussed in Sec. 3.1. The three-body parameter values thereby inserted into the RHS of Eq. (3.20) correspond to the Λ values used to obtain the S matrix element on the LHS. For the four systems ^{40}K-^{87}Rb, ^{6}Li-^{87}Rb, ^{40}K-^{133}Cs, and ^{6}Li-^{133}Cs, we plot the S-wave scaling functions of the form $|s_{ij}|e^{i\theta_{ij}}$ in Fig. 3.4. We observe apparent trends in each tile of the figure as the mass ratio is varied. Then, values for η_* have been determined, or estimated, in either experiments or theoretical calculations for these systems [41, 4, 38, 96] and are included in the S-wave recombination rate for shallow and deep diatomic molecules. Equation (3.20) is helpful because it separates the S matrix expression into terms that depend on the three-body parameters a_{*0} and η_* and those that depend on non-universal three-body physics or universal two-body physics, i.e. scaling variable $x = \sqrt{E/E_D}$.

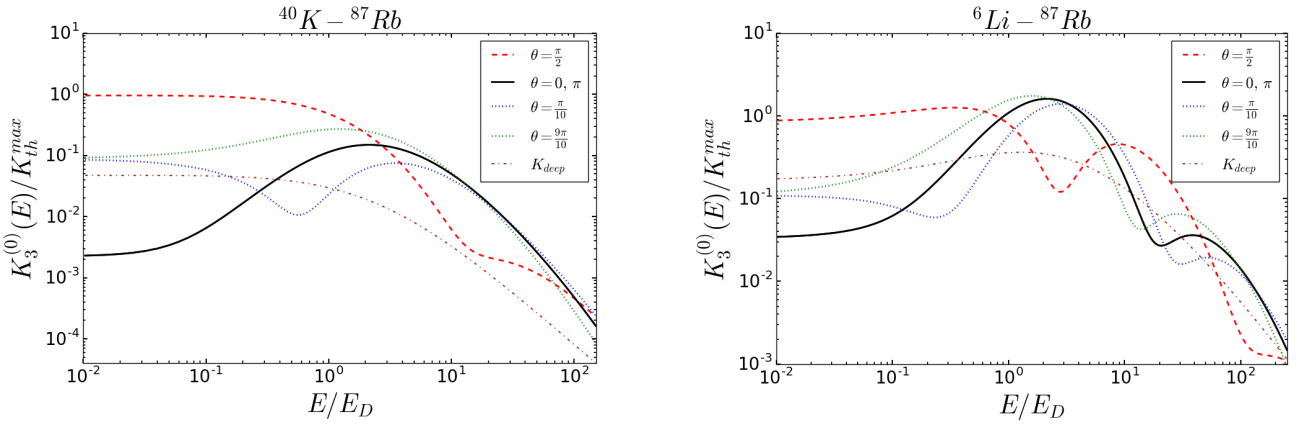

Fig. 3.5 – On the left, we show the $L = 0$ recombination rate and K_{deep} each divided by the maximum threshold value K_{th}^{max} for a variety of values of θ_{*0} in the ^{40}K-^{87}Rb system with $\eta_* = 0.05$ and on the right we give the $L = 0$ recombination rate and K_{deep} each divided by K_{th}^{max} for a variety of values of θ_{*0} in the ^{6}Li-^{87}Rb system with $\eta_* = 0.2$.

With the universal functions s_{ij} in hand, we calculate the S-wave heteronuclear three-body recombination rate $K_3^{(0)}(E)$ as

$$K_3^{(0)}(E) = \frac{128\pi^2\mu^{3/2}}{\mu_{A_2D}^{3/2}}\frac{1}{x^4}\left(1 - \left|s_{22}(x) + \frac{s_{12}(x)^2 e^{2i\theta_{*0}-2\eta_*}}{1 - s_{11}(x)e^{2i\theta_{*0}-2\eta_*}}\right|^2 - \frac{(1-e^{-4\eta_*})|s_{12}(x)|^2}{|1 - s_{11}(x)e^{2i\theta_{*0}-2\eta_*}|^2}\right)\frac{a^4}{2\mu}, \tag{3.21}$$

where the third term in the parenthesis of Eq. (3.21) is from the incorporation of possible transitions from an A_2D scattering state or three atoms into an atom and a deeply bound diatomic molecule in the intermediate state. The need for this term is discussed at length in Ref. [39]. With the possession of one of the recombination minima and the inelasticity parameter as experimental or theoretical inputs, this equation then yields the energy-dependent S-wave recombination rate.

We give the rate for recombination into an atom and a *shallow* diatomic molecule in Eq. (3.21), but an additional contribution must be added to this because of the formation of *deeply* bound molecules in the final state. The significance of this contribution depends on the size of η_* for a given system. In the $L \geq 1$ scattering channels this contribution is subleading in the zero-range limit [39]. But, when $L = 0$ there is a leading order term

$$K_3^{\rm deep}(E) = \frac{128\pi^2\mu^{3/2}(1-e^{-4\eta_*})[1 - |s_{11}(x)|^2 - |s_{12}(x)|^2]}{\mu_{A_2D}^{3/2}x^4|1 - s_{11}(x)e^{2i\theta_{*0}-2\eta_*}|^2}\frac{a^4}{2\mu} \tag{3.22}$$

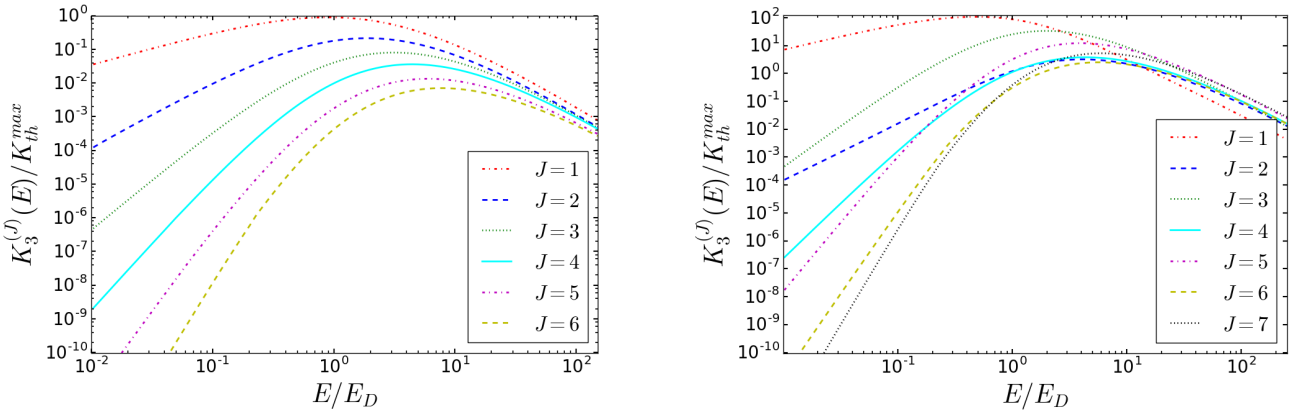

Fig. 3.6 – On the left, we show $K_3^{(L)}(E)/K_{th}^{max}$ for ^{40}K-^{87}Rb, and on the right we show $K_3^{(L)}(E)/K_{th}^{max}$ for ^{6}Li-^{87}Rb. J is used in place of L in the vertical plot axes and follows the labeling convention of Ref. [5]. However, in this dissertation we consistently label orbital angular momentum with L.

that must be added to the rate due to recombination into shallow molecules in order to obtain the total recombination rate.

We verify the $E \to 0$ limits of $K_3^{(0)}(E)$ and $K_3^{\rm deep}(E)$ in Eqs. (3.21) and (3.22) in this study by comparing them with the analytical threshold expressions of Eqs. (3.8) and (3.12) multiplied by a factor of 2 from the statistics of the system. The S-wave three-atom threshold expression for the recombination into both shallow and deep states has a maximum value $K_{\rm th}^{\rm max}$ at $\theta_{*0} = \pi/2$. This value is proportional to $\alpha_{\rm th}^{\rm max}$ defined in Eq. (3.13) by a factor of 2, or $K_{\rm th}^{\rm max} = 2\alpha_{\rm th}^{\rm max}$.

In Fig. 3.5, we show the energy dependence of $K_3^{(0)}(E)$ and $K_3^{\rm deep}(E)$ at various values of θ_{*0} for the ^{40}K-^{87}Rb and ^{6}Li-^{87}Rb. Theoretical results for these or similar systems can be provided by the author upon request. The rates are displayed in the units of $K_{\rm th}^{\rm max}$. The variations in the shape of the $K_3^{(0)}$ curves as θ_{*0} for these systems show that the energy dependence of S-wave recombination into a shallow state has a detailed dependence on the scattering length and the scaling parameter s_0.

The energy dependence of the recombination rate $K_3^{(L\geq 1)}$ for higher partial waves is shown in Fig. 3.6 for ^{40}K-^{87}Rb and ^{6}Li-^{87}Rb. These are also expressed in the units of the S-wave rate maximum $K_{\rm th}^{\rm max}$ in order to facilitate a comparison of the magnitude of the $L \geq 1$ rate contributions to the $L = 0$ contribution. In the ^{40}K-^{87}Rb system, the contributions of

successively higher partial waves get smaller, and this is different behavior than that exhibited by a system of identical bosons, in which the contribution from the $L = 4$ partial wave was comparable to that of the $L = 1$ partial wave [39]. Such behavior is only observable in the ^{6}Li-^{87}Rb system at very low energies. Additionally, we found that while the recombination rates $K_3^{(L)}(E)$ in Figs. 3.5 and 3.6 have similar energy dependence near the three-atom threshold to those found in Ref. [97], we do not reproduce the dependence on the mass ratio δ suggested therein. Instead, we find a more complicated mass-ratio dependence for general values of three-body energy E. We only expect the results of Ref. [97] at zero temperature.

In order to ascertain the experimental temperature scale around and above which recombination minima are unlikely to be measured due to large $L \geq 1$ scattering channel contributions, Figs. 3.5 and 3.6 can be compared. For example, in ^{40}K-^{87}Rb, the $L = 1$ partial-wave contribution becomes larger than the S wave around E_D, which corresponds to a temperature $T_{\rm KRb} = 0.3E_D/k_B \approx 0.1(a/a_0)^{-2}K$, where a_0 is the Bohr radius. But, in ^{6}Li-^{87}Rb higher partial waves obscure at a very low temperature $\sim 10^{-3}E_D$, which corresponds to a temperature $T_{\rm LiRb} = 10^{-3}E_D/k_B \approx 0.015(a/a_0)^{-2}K$. These relations provide some constraints on the observation of Efimov physics and can be viewed as either setting a maximum scattering length below which minima can be observed, so long as $a \gg \ell$ still holds, or giving a temperature below which one may begin to observe known minima located at a given value of a and lower.

3.4 Comparison with Experiment

In order to compare the results of this study with experiments we need values for the two three-body parameters a_{*0} and η_*. Then, we calculate the contributions from all necessary scattering sectors and combine them into a total expression for the recombination rate as

$$K_3(E) = \sum_{L=0}^{\infty} K_3^{(L)}(E) + K_3^{\rm deep}(E)\,. \tag{3.23}$$

Next, we take a Boltzmann average over $K_3(E)$ in order to arrive at the recombination rate constant at a given scattering length and finite temperature used in relevant experiments [39].

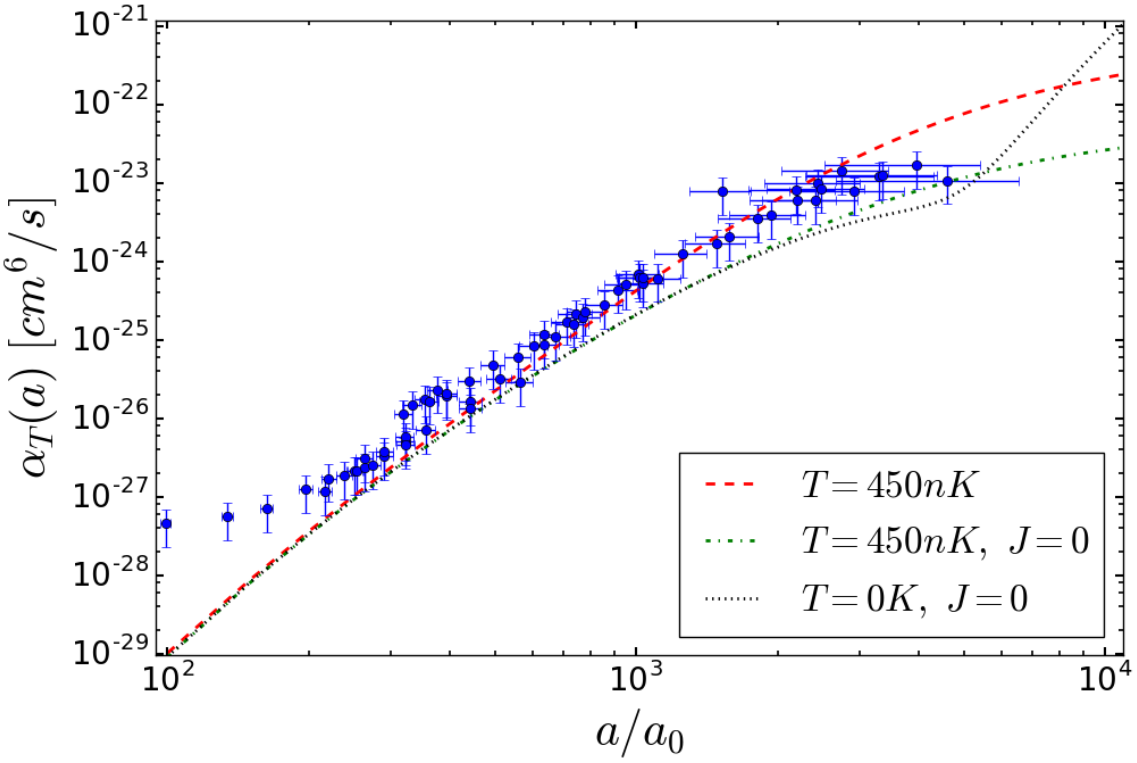

Fig. 3.7 – Recombination rate constant α_T as a function of the scattering length a for ^{40}K-^{87}Rb with $\eta_* = 0.05 \pm 0.02$ [41] and the three-body parameter adjusted to reproduce a recombination minimum at $a_{*0} \approx 5000a_0$. The dashed red line at 450 nK corresponds to the temperature at which the large-a data of Bloom *et al.* given by the blue dots with error bars in this plot was taken [38].

This thermal-averaged rate constant is

$$\alpha_T \approx \frac{\int_0^\infty dE\, E^2 e^{-E/k_B T} K_3(E)}{2\int_0^\infty dE\, E^2 e^{-E/k_B T}}\,, \tag{3.24}$$

where the leading factor of 2 in the denominator is the symmetry factor 2!1!. The lower limit on the integral is $E = 0$ because we start the integration at the three-atom threshold, which is appropriate for a gas of initially free atoms.

Bloom *et al.* estimated the inelasticity parameter η_* to be $\eta_* = 0.26$ for a ^{40}K-^{87}Rb mixture [38] by matching a threshold formula for the atom-molecule *relaxation* loss rate coefficient β to experimental data. On the other hand, they later gave a value $\eta_* = 0.02$ as a good match for their measurements of the rate constant α. However, in each of those determinations of the inelasticity parameter, a zero-temperature formula

was compared to finite temperature data, so neither value of η_* may be strictly reliable. Further, the data published in that work is restricted to values of a that are smaller than the thermal wavelength of the atoms set by the experimental temperature of the gas. Meanwhile, in Ref. [41] Helfrich *et al.* found a value of $\eta_* = 0.05 \pm 0.02$ by fitting their Eq. (20) to corresponding data in Ref. [98]. For this study, we use the experimental value $a_* = 230a_0 \pm 30a_0$ obtained in Ref. [38] for ^{40}K-^{87}Rb to determine the position of the recombination minimum $a_{*0} \approx 5000a_0$. We determine the value of a_{*0} through the use of the universal relation $a_*/a_{*0} = 0.51 \exp(\pi/2s_0)$ for ^{40}K-^{87}Rb [41], which is an exact relation in the zero-range limit employed in this work. In this universal relation, a_* is the scattering length value at which the Efimov trimer state contacts the A_2D threshold. On the other hand, a theoretical calculation by Wang *et al.* [99] predicted a value of $a_{*0} = 2800a_0$. In their procedure they used a background Rb-Rb scattering length of $a_{22} = 100a_0$. The relatively large temperatures ~ 300 nK used in the experiment of Bloom *et al.* do not allow for the observation of this feature. This discrepancy between the result of Ref. [99] and the universal prediction obtained from the a_* value of Ref. [38] thus cannot be addressed. To resolve the issue, a challenging-to-achieve experimental temperature of roughly 10 nK would be needed in order to clearly observe the recombination minima in this system.

Evidence is given by Bloom *et al.* that the ^{87}Rb-^{87}Rb-^{87}Rb recombination channel due to a small scattering length a_{22} can be neglected. Namely, they observed a ratio of ^{87}Rb loss to ^{40}K loss of 2.1(1), indicating that the dominant loss channel is that of ^{40}K-^{87}Rb-^{87}Rb recombination. In our effective-field-theory approach the uncertainty in the recombination rate calculation introduced by neglecting a small valued a_{22} is of the order of a_{22}/a. The perturbative approach of Ref. [92] could be employed to account for any such corrections so long as $a_{22} < a$.

Even for the recombination minimum value we choose at $a_{*0} \approx 5000a_0$, the experimental work in Ref. [38] cannot rule for or against it as the correct location of the minimum because the average experimental temperature $\sim 300nK$ imposes the limit $a \lesssim 3000a_0$ on the range of validity for the data. Near and above that point the experimental uncertainties become rather large. Thus, for ^{40}K-^{87}Rb no Efimov features for $a \geq 0$ have been definitively observed for currently accessed scattering lengths and temperatures. From additional numerical studies

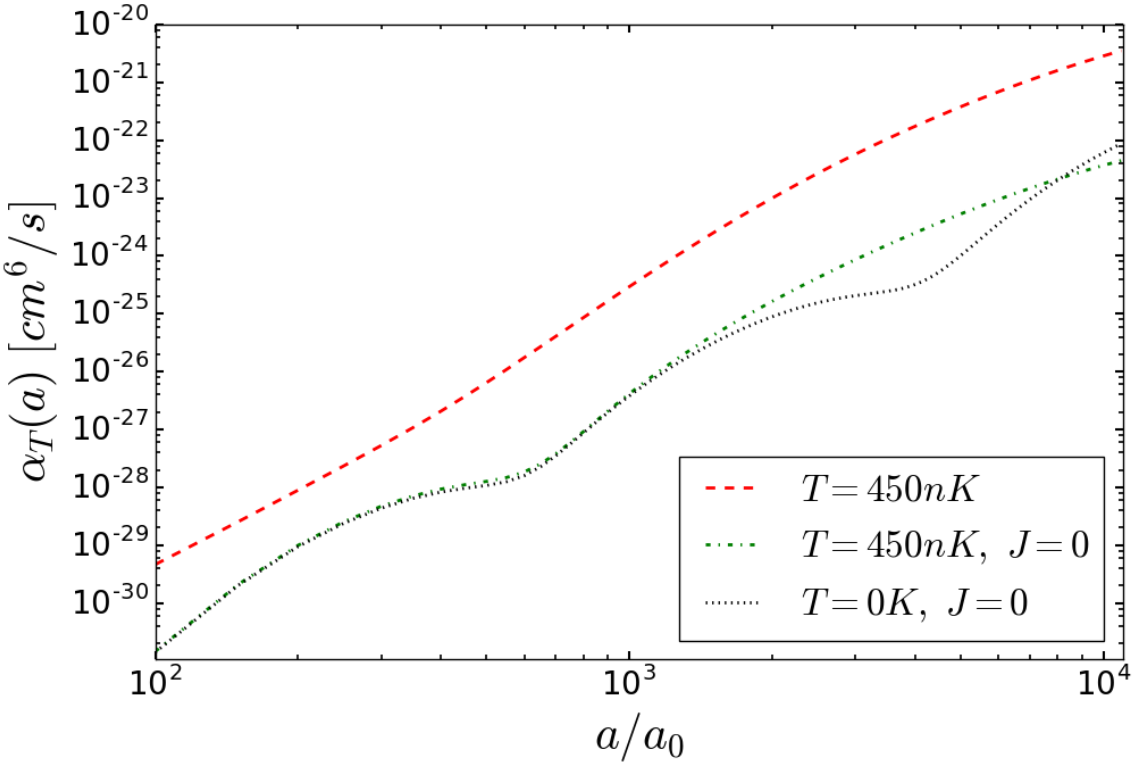

Fig. 3.8 – Recombination rate constant α_T as a function of the scattering length a for ^{6}Li-^{87}Rb for $\eta_* = 0.2$ with a recombination minimum at $a_{*0} \approx 610a_0$. The higher partial wave contributions to the rate constant increase the total result by more than an order of magnitude above the $L = 0$ ($J = 0$) rate constant. We do not know of any relevant experimental data for this system at the time of this writing.

we determine that a minimum at $a_{*0} \approx 5000a_0$ would only be observed at temperatures well below 10 nK. In Fig. 3.7, we show the data of Ref. [38] along side our curves obtained numerically using Eq. (3.24). One curve shows the $L = 0$ contribution to the rate constant at 450 nK, another shows the total rate at 450 nK after summing over L, and we include the zero-temperature result obtained by summing Eqs. (3.8) and (3.12) comparison to the finite temperature $L = 0$ contribution. In each of the three curves shown in the plot, which we label in the plot legend, we use the values $a_{*0} = 5000a_0$ and $\eta_* = 0.05$. The 450-nK curve and the experimental data are in excellent agreement except in the region $a \lesssim 200a_0$, below which contributions from the intraspecies bosonic scattering length and the finite range of the interaction may be important. The size of the discrepancy in this region may indicate that the correction from the a_{22} scattering length is the most important of the two because

the quoted van der Waals range for ^{40}K-^{87}Rb is $R_{\rm vdW} = 72a_0$ [38], which gives a range correction of only around 35%-70% in this region, while the actual difference observed there in Fig. 3.7 is much larger.

Some similar systems, namely the ^{39}K-^{87}Rb and ^{41}K-^{87}Rb mixtures, were studied by Wacker *et al.* [100]. For $a > 0$, no evidence for Efimov resonances was observed in the accessed range of scattering lengths and temperatures. This further demonstrates the difficulty that a large scaling factor imposes on the problem and makes the use of systems with a larger mass imbalance, such as ^{6}Li-^{87}Rb or ^{6}Li-^{133}Cs, attractive. Therefore, we explore finite-temperature effects on the recombination rate for the ^{6}Li-^{87}Rb mixture and give our results in Fig. 3.8. To obtain the necessary input parameters for a_{*0} and η_*, we examined a couple of sources. The ^{7}Li-^{87} Rb system was studied by Maier *et al.* in Ref. [101], and they found a value of $|a_-| = 1870a_0 \pm 121a_0$. Based on this, they suggested a value of a_- of $-1600a_0$ for ^{6}Li-^{87}Rb. With the relation $|a_-|/a_{*0} = \exp(\pi/2s_0)$, this gives a recombination minimum position of $a_{*0} \approx 610a_0$. For η_* we turned to the estimate of Petrov and Werner in Ref. [4] of $\eta_* = 0.20$ in the absence of any known experimental results. In Fig. 3.8 we use $\eta_* = 0.20$ and $a_{*0} = 610a_0$ as our three-body parameters. We find that finite-temperature effects drastically obscure the features of Efimov universality, specifically recombination minima, because of the large size of the $L \geq 1$ rate contributions at experimentally relevant temperatures. At the same time, even if there were no higher-partial-wave contributions to the overall rate, we find that finite-temperature effects in the $L = 0$ channel hide the second minimum at $a \approx 4000a_0$ seen in the dotted line of Fig. 3.8. The non-universal rate contributions from $L \geq 1$ scattering channels begin to be suppressed relative to the $L = 0$ contribution at temperatures below ~ 10 nK, and the minimum at $610a_0$ becomes experimentally accessible.

In order to better understand the mass-ratio dependence of the relative size of higher-partial-wave rate contributions, partial-wave analyses like that shown in Fig. 3.6 were performed for several additional systems. It was found that $L \geq 1$ partial wave contributions to the recombination rate become increasingly dominant as m_1/m_2 decreased. Thus, to see detailed universal behavior occurring from the $L = 0$ scattering channel, it seems that an experiment must be performed at very low temperatures for small mass ratios.

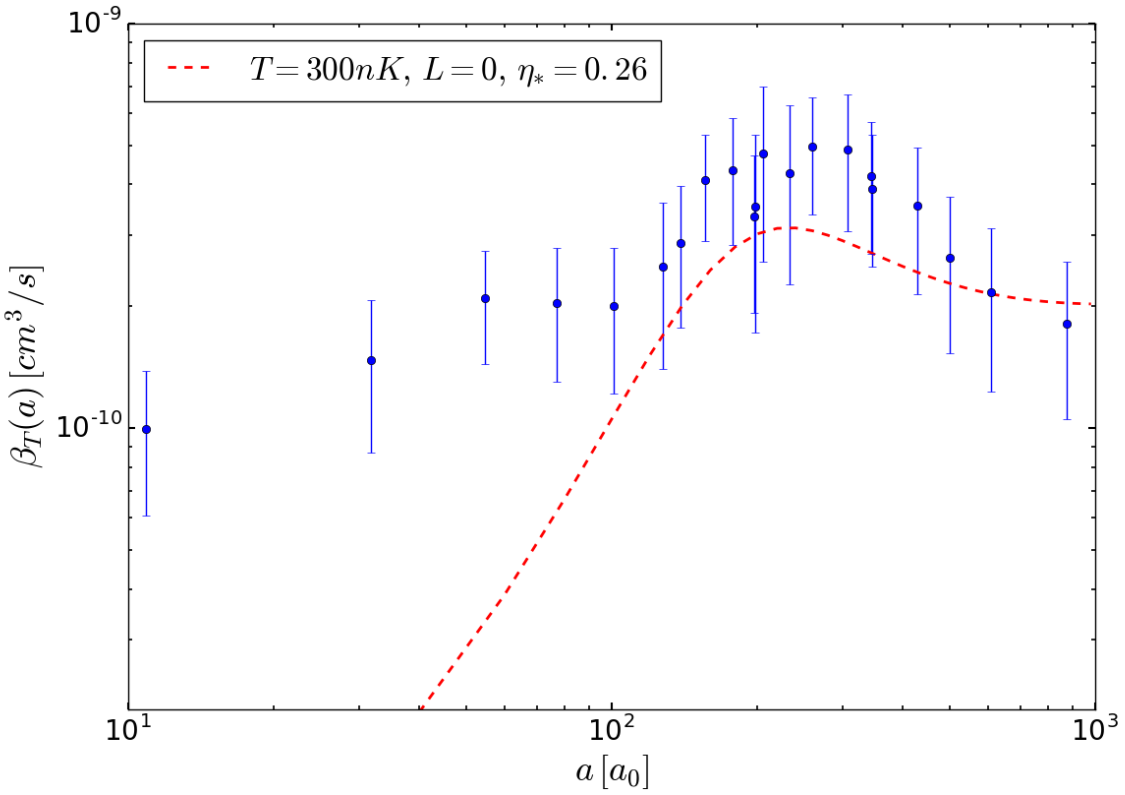

Fig. 3.9 – The atom-diatomic molecule relaxation rate as a function of the scattering length a at finite temperature for orbital angular momentum $L = 0$. The temperature 300 nK corresponding to the dashed red line is the average temperature that the experimental data presented in the plot by the blue dots with error bars was taken at. This data is from Bloom *et al.* in Ref. [38]. The value we use for η_* is also from that reference.

This observed trend is in disagreement with the suggestion of D'Incao and Esry [97] that in systems in which A_2 is bosonic the dominant recombination rate contribution comes from the $L = 0$ channel. Though this is certainly true at zero and very low temperatures, it does not seem to be true at all values of E and T, especially when the mass ratio m_1/m_2 is small.

The additional observable we address, namely the atom-diatomic molecule relaxation rate, were also calculated at finite temperatures and compared to the experimental data of Ref. [38] for the ^{40}K-^{87}Rb system. We express this rate for a particular scattering length as

$$\beta_T = \frac{\int_{-B_D}^{\infty} dE(E+B_D)^2 e^{-(E+B_D)/k_B T}\beta(E)}{\int_{-B_D}^{\infty} dE(E+B_D)^2 e^{-(E+B_D)/k_B T}} \tag{3.25}$$

where $\beta(E)$ is only a function of the three-body energy and is given by Eq. (3.15). We integrate in Eq. (3.25) from the A_2D threshold, namely $E = -B_D$, and we add B_D in the necessary places in this equation to ensure that the distribution starts at this threshold. Our thermally averaged relaxation rate $\beta_T(a)$ is presented in Fig. 3.9. Using the value of $a_{*0} \approx 5000a_0$ derived from the data of Bloom *et al.* used above, we observe the relaxation maximum at $a_* = 230a_0$, as expected. The relaxation rate has also been experimental observed at finite temperature in a system of identical bosons by Knoop *et al.* in Ref. [102]. One of the primary benefits of such experiments is the direct observation of one three-body parameter of the system, from which the full spectrum of universal three-body bound states may be obtained.

3.5 Concluding Remarks on the Heteronuclear System

In this chapter, we studied three-body recombination at finite temperatures in heteronuclear mixtures wherein the interspecies scattering length is large and positive. Universal scaling functions useful to the calculation of the temperature-dependent recombination rate were calculated using the STM equation for arbitrary values of η_* and the chosen three-body parameter a_{*0}. In this study, each mass ratio δ necessitates a new set of scaling functions, which were calculated for several systems of interest. Also, universal scaling functions for the $L \geq 1$ scattering channels were calculated. Although they do not display the Efimov effect, these loss channels contribute to the total loss rate. We showed in this chapter that the observation of the Efimov effect seems increasingly difficult as the mass ratio decreases. This is due to the relatively large $L \geq 1$ rate contributions at experimentally feasible temperatures. Thus, systems with small values of δ are in fact less favorable for the experimental observation of Efimov features at scattering lengths $a > 0$ than initially postulated [82]. Additionally, we calculated the $L = 0$ A_2D relaxation rate at finite temperature as a function of the scattering length. The results of this work were compared with experimental data for three-body recombination and atom-diatomic molecule relaxation in an ultracold mixture of ^{40}K-^{87}Rb atoms and good agreement with the data was found.

Additional studies assessing the impact of finite range corrections to the recombination rate at relatively small values of a could be carried out in a relatively straight forward way in the future. These effects were studied in an EFT framework for identical bosons in Refs. [88, 6] and for heteronuclear mixtures in Ref. [92]. The inclusion of finite range effects would provide an understanding of Efimov physics even in the case in which a is not particularly large. This could be useful for the experimental avoidance of large a values, at which the higher partial-wave contributions dominate the total recombination rate. A perturbative inclusion of a finite intraspecies scattering length a_{22} has been done in Ref. [92] at $T = 0$ K for $|a_{22}| \ll |a|$, and a nonperturbative calculation [4] was performed for $|a_{22}| \sim |a|$ at finite temperatures for $a < 0$. But, this has not yet been done for finite temperatures when $a > 0$, and major changes to the existing formalism would be necessary to accommodate additional scattering channels if $a_{22} > 0$.

Chapter 4

Nuclear Polarization Effects in Muonic Deuterium

Muonic deuterium is an important nucleus to study because of its relative simplicity compared to any larger nucleus. It is therefore an important testing ground for various theoretical approaches in few body physics [103]. One of these approaches is ∉EFT. Several papers have been published in which the properties of the deuteron are addressed using this EFT [104, 105, 106]. The deuteron is a suitable system to study with ∉EFT because it has an expansion parameter $\gamma\rho_d \sim 1/3$, where γ is the deuteron binding momentum and ρ_d the deuteron effective range.

The theoretical problem we address in this study is directly connected to the proton and deuteron radius puzzles recently highlighted by Krauth *et al.* and Hernandez *et al.* in Refs. [42, 45] and earlier by Mohr *et al.* in Refs. [107, 108]. For the proton, this puzzle is characterized by differences of at least 5.6σ between the proton radius values extracted from e-H versus μ-H measurements, as noted in Refs. [107, 108], where σ is the standard deviation of the measurements in μ-H. Some recent results such as Ref. [44] narrow the gap between the disparate radii values, but do not erase it altogether, and the problem still has not been fully understood. A similar discrepancy has also been observed between muonic deuterium (μ-D) and electronic deuterium (e-D) [109], and the dependence of this discrepancy on atomic mass A and charge number Z has been examined in various studies. Some explanations of this

discrepant behavior include but are not limited to beyond-the-standard-model theories, but we do not address them here.

We approach the radius problem in μ-D by performing a $\not\pi$EFT calculation of the correction to the 2S-2P Lamb shift in muonic deuterium due to nuclear polarization effects of two-photon-exchange (TPE) between the muon and the nucleus. This is possible because the nuclear polarization correction to the atomic spectrum is related to the deuteron charge radius by the equation [110]

$$\Delta E_{LS} = \delta_{QED} + \delta_{pol} + \delta_{Zem} + \frac{m_r^3 \alpha^4}{12} \langle r_{ch}^2 \rangle_d \,, \tag{4.1}$$

where α is the fine-structure constant, m_r is the reduced muon mass, and the sum $\delta_{pol} + \delta_{Zem}$ gives the total TPE correction, $\delta_{\rm TPE}$. Krauth *et al.* provide a similar formula in Ref. [103]. This equation allows for the extraction of the deuteron charge radius once the other contributions on the RHS of Eq. (4.1) are known from theoretical calculations and the LHS is taken from experiments. The charge radius r_{ch} in Eq. (4.1) is defined in the subleading contribution to the electric form factor of the deuteron, as in the hydrogenic case [111].

Of the terms that must be calculated theoretically, the QED corrections represented by δ_{QED} are very accurately known [112, 113]. So, for the determination of the charge radius, it is the theoretical uncertainty of the two-photon-exchange parts that contribute the most to the uncertainty of the extracted radius. The expression in Eq. (4.1) breaks up $\delta_{\rm TPE}$ into $\delta_{pol} + \delta_{Zem}$. We follow this approach and calculate the inelastic and elastic TPE terms separately. Several sources, such as Hernandez *et al.* in Ref. [114], make a further separation of the TPE correction into terms depending on few-nucleon dynamics and those depending on the properties of individual nucleons. We only consider the first case in this dissertation and do not examine corrections from the structure of individual nucleons.

We study μ-D rather than e-D because the nearly non-relativistic velocity of the muon renders the calculation simpler, but also renders the TPE part of the Lamb shift as a larger percentage of the total than in the electronic case due to the heavier muon mass, making high precision estimates of the nuclear charge radius possible. We study the Lamb shift

because S-level shifts are well understood, and the orbiting muon does not penetrate the physical volume of the nucleus at these energies, greatly simplifying the calculation.

In addition to the nuclear radius puzzle, polarization corrections to the atomic structure of light nuclei are one of the largest sources of uncertainties in shifts in atomic spectra, so these corrections are interesting beyond calculating nuclear radii and were studied long before the proton radius puzzle was unearthed. In Ref. [115], nuclear polarization corrections were studied in the context of the isotope shift of the $1S - 2S$ transition in electronic hydrogen and deuterium. At the experimental accuracy of the early 1990s, the virtual excitations of the deuteron became necessary to take into account [116, 117] for this calculation and for the extraction of nuclear sizes. By the mid 1990s, there was ongoing discussion about the precise value of the deuteron charge radius, as there is to this day [45].

Many recent studies for a system such as μ-D use state-of-the-art potentials such as AV18 or the latest chiral EFT potentials [114]. Uncertainty estimates have also been reduced to the level of a few percent in modern calculations. Previous calculations mark the progress that has been made on this topic over the last few decades. For example, Lu and Rosenfelder used a simple separable potential in Ref. [115] to determine the inelastic structure functions of the nucleus. While that is not very realistic, it allowed for a fair description of light nuclei, for which the low-energy parts of the interaction are dominant. At the same time, the separable potential of Yamaguchi used in Ref. [115] gives smaller values of the dipole polarizabilities than those given by the realistic potentials of the early to mid 1990s. At the same time, they still have reasonable and realistic numbers for the results. An alternative early calculation of the μ-D polarization shift is given by Fukushima *et al.* in Ref. [118].

We use the approach that is detailed by Leidemann and Rosenfelder in Ref. [47] and based on an earlier paper by Rosenfelder [46]. In the earlier paper, Rosenfelder first expressed the shift in terms of the forward virtual Compton amplitude, which may also be understood as the part of the full Compton amplitude in which the nucleus is in an excited intermediate state [115]. However, instead of using state-of-the-art chiral potentials, we apply $\not\pi$EFT in an approach which is related to the zero-range methods of Friar in Ref. [48] and similar to the techniques of Chen *et al.* in Ref. [104].

In Sec. 4.1, we detail the formalism that we use from Refs. [46, 47]. Then, in Sec. 4.2 we detail the theoretical techniques that we use and give the NLO renormalization of the two-body t-matrix. Section 4.3 contains our $\not\pi$EFT calculation of the leading-order longitudinal inelastic structure function and an extraction of the part due to electric-dipole excitation of the nucleus. Sections 4.4 and 4.5 provide the electric-dipole contribution to the longitudinal structure function at NLO and the determination of the NLO wavefunction renormalization factor Z, respectively. Information on additional corrections to the polarization correction is provided in Sec. 4.6, and in Sec. 4.7, the results for our calculation of the energy shift are presented and compared to previous literature. Section 4.8 discusses uncertainty in our calculation and compares it to uncertainties in previous calculations.

4.1 Energy Shift

The equation for the energy shift due to two-photon-exchange between the muon and the nucleus that we set out to use was derived by Rosenfelder in Ref. [46]. The relevant amplitude is also known as *forward virtual Compton scattering*. This gives the TPE correction to the 2S-2P Lamb shift as

$$\Delta\epsilon_{n0} = (4\pi\alpha)^2 |\phi_{n0}(0)|^2 \mathrm{Im} \int \frac{d^4q}{(2\pi)^4} \frac{2m}{(q^2+i\epsilon)^2 - 4m^2 q_0^2} \left\{ \frac{1}{\mathbf{q}^2} T_\mathrm{L} + \frac{q_0^2}{(q^2+i\epsilon)^2} T_\mathrm{T} \right\} \tag{4.2}$$

for the nth S-state, where m is the lepton mass, q^μ is the photon four-momentum, and T_L and T_T are the longitudinal and transverse forward virtual Compton amplitudes, respectively. The value of $|\phi_{n0}(0)|^2$ is $(Z\alpha m_r/n)^3/\pi$, where $\alpha \approx 1/137$ is the fine structure constant, Z is the proton number, and m_r is the muon-deuteron reduced mass. Thus, the leading TPE contributions to the energy shift are $O(\alpha^5)$. The portions of the forward virtual Compton amplitudes related to the nucleus are given by

$$\begin{aligned} T_\mathrm{L} =& T_{00}\,, \\ T_\mathrm{T} =& \left(\delta_{ij} - \frac{q_i q_j}{\mathbf{q}^2} \right) T^{ij}\,, \end{aligned} \tag{4.3}$$

where q_i are components of the photon three-momentum and $T^{\mu\nu}$ is the nuclear tensor which couples to two photons [46].

Because of the two $1/\mathbf{q}^2$ factors from the two inclusions of the instantaneous Coulomb potential in the longitudinal part of the forward virtual Compton amplitude, an IR divergence arises in the Feynman diagram calculation that is difficult to resolve. However, in Ref. [46], Rosenfelder noted that one may rewrite the forward virtual Compton amplitude in terms of the longitudinal and transverse inelastic structure functions $S_{L/T}(\mathbf{q}, \omega)$. In that case, an IR divergence is contained in the transverse part of the amplitude and exactly canceled by the seagull term, which is also necessary to preserve gauge invariance, and no IR divergence appears in the longitudinal part.

The longitudinal part in terms of the inelastic structure function is given in Ref. [46] as

$$T_{\mathrm{L}}(q_0, \mathbf{q}) = \int_0^\infty d\omega \, S_{\mathrm{L}}(\mathbf{q}, \omega) \left\{ \frac{1}{q_0 - \omega + i\epsilon} - \frac{1}{q_0 + \omega - i\epsilon} \right\} , \tag{4.4}$$

and the transverse part is

$$T_{\mathrm{T}}(q_0, \mathbf{q}) = \text{seagull} + \int_0^\infty d\omega \, S_{\mathrm{T}}(\mathbf{q}, \omega) \left\{ \frac{1}{q_0 - \omega + i\epsilon} - \frac{1}{q_0 + \omega - i\epsilon} \right\} , \tag{4.5}$$

where ω is the energy transferred to the nucleus via a virtual photon and

$$S_{\mathrm{L/T}}(\mathbf{q}, \omega) = \sum_{n \neq 0} \delta(\omega - (E_n - E_0)) |\langle n | \mathcal{O}_{\mathrm{L/T}}(\mathbf{q}) | 0 |^2 , \tag{4.6}$$

where $\mathcal{O}_{\mathrm{L}}(\mathbf{q}) = \rho(\mathbf{q})$ is the charge density operator and $\mathcal{O}_{\mathrm{T}}$ is the current operator. In our field-theoretical approach, the charge operator corresponds to a photon-nucleon vertex factor proportional to $-ie$, where $e = -|e|$ is the electron charge.

The nuclear polarization correction to the 2S energy level is obtained in Ref. [47] by integrating over the inelastic structure functions $S_{L/T}(\mathbf{q}, \omega)$ with the appropriate integration kernels obtained from the detailed leptonic and photonic Feynman rules. In the Coulomb gauge, the inelastic longitudinal structure function is related to the square amplitude for the disintegration of the deuteron by a Coulomb photon with energy ω and three-momentum $\mathbf{q}$. The inelastic transverse structure function fills the same role, albeit with a transverse vector

photon exchanged between the muon and nucleus. The equation we use for the total energy shift due to TPE is found in Ref. [47] and is

$$\Delta\epsilon_{n0} = -8\alpha^2 R_{n0}|\phi_{n0}(0)|^2 \int_0^\infty dq \int_0^\infty d\omega \left[K_L(\mathbf{q},\omega)S_L(\mathbf{q},\omega) + K_T(\mathbf{q},\omega)S_T(\mathbf{q},\omega) + K_S(\mathbf{q},\omega)S_T(\mathbf{0},\omega)\right], \tag{4.7}$$

where it should be stated that for the structure functions there are more subtle restrictions placed on the limits of integration, which we describe below. The factor R_{n0} is a correction factor determined to be $R^{(\mu)} = 0.9778$ [47] for muonic deuterium and is given in general to first order in the ratio of the nuclear radius to the Bohr radius a_B by

$$R_{n0} \simeq R = 1 - 3.06\frac{\langle r^2\rangle^{1/2}}{a_B}. \tag{4.8}$$

The purpose of this correction factor in Eq. (4.7) is to account for the slight variation of the muon wavefunction over the physical volume of the nucleus.

Reference [47] also provides the integration kernels derived with fully relativistic lepton kinematics for the various contributions to the energy shift. It is most important to maintain these relativistic kinematics in the electronic case, as these effects are small in the muonic case. However, these effects are not negligible, so we include both a relativistic and non-relativistic result in Sec. 4.7 below. As a side note, our approach allows for relativistic corrections in the nucleon kinematics, but we do not keep these very small corrections. For longitudinal inelastic excitations of the nucleus, the fully relativistic kernel is given by

$$K_L(\mathbf{q},\omega) = \frac{1}{2E_\mathbf{q}}\left[\frac{1}{(E_\mathbf{q}-m)(\omega+E_\mathbf{q}-m)} - \frac{1}{(E_\mathbf{q}+m)(\omega+E_\mathbf{q}+m)}\right]. \tag{4.9}$$

The non-relativistic (NR) reduction of Eq. (4.9) is

$$K_L^{(\mathrm{NR})}(\mathbf{q},\omega) = \frac{1}{\mathbf{q}^2}\frac{1}{\omega+\frac{\mathbf{q}^2}{2m}}, \tag{4.10}$$

where m is the lepton mass. For transverse excitations, the contribution from the leptonic and photonic propagators is given by

$$K_T(\mathbf{q},\omega) = -\frac{1}{4m|\mathbf{q}|}\frac{\omega+2|\mathbf{q}|}{(\omega+|\mathbf{q}|)^2} + \frac{\mathbf{q}^2}{4m^2}K_L(\mathbf{q},\omega)\,., \tag{4.11}$$

where m is again the lepton mass and $E_q = \sqrt{\mathbf{q}^2+m^2}$. Lastly, the seagull term has a kernel given by

$$K_S(\mathbf{q},\omega) = \frac{1}{4m\omega}\left(\frac{1}{|\mathbf{q}|} - \frac{1}{E_\mathbf{q}}\right)\,, \tag{4.12}$$

which is given in Ref. [47].

The transverse part of the structure function is much larger in e-D than in μ-D [115] in the Coulomb gauge. This is because while they are each suppressed by a factor of $1/m_\ell$, where the m_ℓ is the relevant lepton mass, the muon is much heavier than the electron, which leads to a greater suppression of the transverse term in the muonic case. As found in Table II of Ref. [47], in the Coulomb gauge, the transverse part of the energy shift contributes less than 1% of the total shift in μ-D. The seagull term was included in the transverse contribution of that reference. At the same time, it is important to note that it is the total energy shift including the longitudinal, transverse, and seagull components that is the meaningful, gauge invariant physical quantity, and that the components thereof are dependent on the gauge choice. Nevertheless, as we are working in the Coulomb gauge and studying μ-D, we restrict ourselves for the present to studying only the part of the energy shift due to longitudinal excitations.

4.2 Renormalization at NLO with PDS

In the ≠EFT framework we use, the Lagrangian in the Coulomb gauge, in which $\nabla \cdot \mathbf{A} = 0$, is given by

$$\begin{aligned}\mathcal{L} =& \psi_\sigma^\dagger \left[i\partial_0 + \frac{\nabla^2}{2M} \right] \psi_\sigma - e\psi_\sigma^\dagger Q A_0 \psi_\sigma + \frac{ie}{2M} \left[-\psi_\sigma^\dagger Q \mathbf{A} \cdot \nabla \psi_\sigma \right] \\ & - \frac{e^2}{2M} \psi_\sigma^\dagger Q \mathbf{A} \cdot \mathbf{A} Q \psi_\sigma - C_0 \left(\psi^T P_i \psi \right)^\dagger \psi^T P_i \psi \\ & + \frac{C_2}{8} \left[\left(\psi^T P_i \psi \right)^\dagger \left(\psi^T \left[P_i \overrightarrow{\partial}^2 + \overleftarrow{\partial}^2 P_i - 2 \overleftarrow{\partial} P_i \overrightarrow{\partial} \right] \psi \right) \right] , \end{aligned} \tag{4.13}$$

where M is the nucleon mass $M = 2\mu$, $\mu = m_p m_n/(m_p + m_n)$, and Q acts in isospin space to couple the photon to the proton and is $(\mathbf{1} + \tau_3)/2$. The 2×2 matrix τ_3 is the usual Pauli matrix, and $\mathbf{1}$ is the 2×2 identity matrix. In μ, m_p and m_n are the proton and neutron masses, respectively. The photon field $\mathbf{A}$ corresponds to the three-vector part of the quantum-field-theoretical photon field with the fully relativistic integration measure, and A_0 is the instantaneous momentum-space Coulomb potential rather than a quantized field. These two parts of the photon are coupled to nucleons through minimal coupling, which makes the replacements $\partial_0 \to D_0 = \partial_0 + ieQA_0$ and $\nabla \to \mathbf{D} = \nabla - ieQ\mathbf{A}$ in the first term of Eq. (4.13). This replacement leads to the second and third terms on line one of the RHS and the first term on the second line containing two factors of $\mathbf{A}$. D_0 and $\mathbf{D}$ may be compressed into the four-vector D^μ [104]. The field ψ is a nucleon field which we define as

$$\psi_{\mathbf{y},\sigma} = \int \frac{d^3p}{(2\pi)^3} \mathrm{e}^{-iE_p t} \mathrm{e}^{i\mathbf{p}\cdot\mathbf{y}} \eta_\sigma a_{\mathbf{p},\sigma} \, , \tag{4.14}$$

where σ is the index containing spin and isospin information, $a_{\mathbf{p},\sigma}$ annihilates an ingoing nucleon with momentum $\mathbf{p}$ and spin/isospin index σ, and η_σ is a spinor doublet containing the spin and isospin information of the nucleon. The most important Feynman rule involving the photon from the above Lagrangian density for our purposes is the vertex factor for a Coulomb photon coupling to a nucleon, which gives $(-ie)Q$. The vector photon propagators and instantaneous Coulomb potential are incorporated in the definitions of the integral kernels of Eq. (4.7) above, so for our purposes we do not explicitly define those here.

We once again must address the renormalization of the two-body t matrix of Chapter 2. However, for the purposes of this chapter, it is more convenient to take a different expansion of $k \cot \delta_0$ than was made in Eq. (2.4). Following the method of Ref. [104], we instead expand around the deuteron pole, $|\mathbf{k}|^2 = -\gamma_t^2$, to obtain

$$|\mathbf{k}| \cot \delta_0 = -\gamma_t + \frac{1}{2}\rho_d(|\mathbf{k}|^2 + \gamma_t^2) + \cdots , \tag{4.15}$$

where the deuteron binding momentum for the spin triplet and isospin singlet deuteron ground state is $\gamma_t^{-1} = 4.318946\,\text{fm}$ and the deuteron effective range $\rho_d = 1.764\,\text{fm}$.

Figures resembling Figs. 2.1 and 2.2 once again describe the scattering up to NLO. However, instead of the NLO amplitude containing a counterterm, used for eliminating a divergence, it contains instead an NLO correction to the coupling constant C_0 corresponding to the two-body contact interaction. We are using couplings C_0 and C_2 instead of λ_0 and ρ_0 in this chapter. We write C_0 as an expansion in the power counting scheme of [104] given by $C_0 = C_{0,-1} + C_{0,0} + \cdots$, where the second index indicates the order of the term in power counting parameter $\mathcal{Q}$ explained below. We confirm the results

$$C_{0,-1} = -\frac{4\pi}{M}\frac{1}{(\mu - \gamma)} , \tag{4.16}$$

$$C_{0,\,0} = \frac{2\pi}{M}\frac{\rho_d \gamma^2}{(\mu - \gamma)^2} , \tag{4.17}$$

$$C_{2,-2} = \frac{2\pi}{M}\frac{\rho_d}{(\mu - \gamma)^2} . \tag{4.18}$$

These coupling constants were determined in the *partial divergence subtraction* (PDS) renormalization scheme introduced by Kaplan, Savage, and Wise in Ref. [12]. In PDS, poles in D dimensions arising in the ultraviolet region of momentum-space loop-diagrammatic calculations (recall that our renormalization scheme in previous chapters included a UV cutoff Λ) are subtracted with a counterterm and a renormalization scale μ is introduced. From this, we can develop a power-counting scheme whereby we track the significance of a contribution based on the number of powers of $\mathcal{Q}$ it contains, where $\mathcal{Q} \sim p/\mu$ and p is the scale of the external momentum. Relativistic corrections in the nucleus enter at N2LO in the power counting, where there are also new contributions to C_0 and C_2 proportional to ρ_d^2.

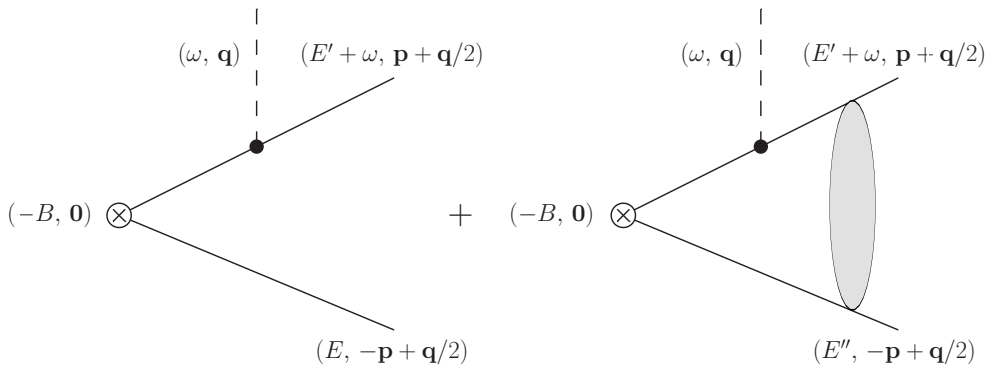

Fig. 4.1 – Diagrams for the longitudinal structure function $S_{\rm L}(\omega,\, \mathbf{q})$. The shaded oval in the second diagram indicates the inclusion of the two-nucleon scattering amplitude. The dashed line corresponds to an incoming A_0 photon, though the related propagator does not enter the calculation of the structure function, and we also leave off the factor $(-ie)$ from the photon-nucleon vertex rule until the end of the calculation. The crossed circle corresponds to the interpolating field $\mathcal{D}_i = N^T P_i N$.

4.3 Longitudinal Structure Function at LO

In this section we calculate the inelastic longitudinal structure function $S_L(\mathbf{q},\, \omega)$ in pionless EFT at LO in the deuteron effective range ρ_d. We assume that the nucleus is approximately static, i.e. has zero three-momentum, and has energy $E = -B = -\gamma^2/M$ prior to its excitation by the photon. This is reasonable because the time scale for TPE is much shorter than any other relevant time scales in the problem. We give the amplitude needed for the calculation of the structure function in Fig. 4.1 we label as $s_{L,a}(\mathbf{p}, \mathbf{q}, \theta)$, and we calculate two distinct amplitudes arising from the first diagram in the figure:

$$s_{L,a1}(\mathbf{p}, \mathbf{q}, \theta) = \frac{\delta_{ji}\sqrt{Z}}{2}\left[S(-\mathbf{p} - \mathbf{q}/2) + S(\mathbf{p} - \mathbf{q}/2)\right], \tag{4.19}$$

$$s_{L,a2}(\mathbf{p}, \mathbf{q}, \theta) = \frac{\delta_{ki}\sqrt{Z}}{2}\left[S(-\mathbf{p} - \mathbf{q}/2) - S(\mathbf{p} - \mathbf{q}/2)\right], \tag{4.20}$$

where Z is the LO renormalization factor given by $Z = -8\pi\gamma/M^2$ at LO in $\mathcal{Q}$ and $S(\pm\mathbf{p} - \mathbf{q}/2)$ is given by

$$S(\pm\mathbf{p} - \mathbf{q}/2) = \frac{iM}{-MB - p^2 \pm pq\cos\theta - q^2/4 + i\epsilon}\,. \tag{4.21}$$

Here, θ is the angle between $\mathbf{p}$ and $\mathbf{q}$, and $MB = \gamma_t^2$. The two distinct nucleon propagators of Eq. (4.21) arise when we consider all possible field-theoretical contractions in the matrix element corresponding to the first diagram. Note that we have left off the vertex factor $(-ie)$ in Eqs. (4.19) and (4.20) coming from the photon-nucleon vertex, and we place it back in at the end of the calculation. Note also that the photon-propagators do not enter here. Rather, they enter the kernels given by Eqs. (4.9) and (4.10) in addition to the lepton propagator. The Kroenecker delta functions in Eqs. (4.19) and (4.20) come from traces over projectors arising from projecting the outgoing state onto one of two possible spin and isospin configurations.

The first projector ensures that the outgoing state is in a spin triplet and an isospin singlet, and we used it to obtain Eq. (4.19). It is given by $P_i = \frac{1}{\sqrt{8}}\sigma_2\sigma_i \otimes \tau_2$. We introduce the second projector needed to project the outgoing NN-state onto a spin triplet and the isospin triplet state corresponding to $\frac{1}{\sqrt{2}}(np + pn)$ as $P_i' = \frac{1}{\sqrt{8}}\sigma_2\sigma_i \otimes \tau_2\tau_3$, and we used it to obtain Eq. (4.20). The σ_i and τ_i matrices are the Pauli matrices, where a matrix σ acts in spin-space and τ acts in isospin-space. A typical matrix element in which the outgoing states are well defined by the projectors will have a form such as $\eta_s^T P_j \eta_{s'} \eta_{s'}^T Q \eta_{s'} \eta_{s'}^T P_i^\dagger \eta_s$, where the 2×2 matrix Q ensures that the photon only couples to the outgoing proton, superscript T indicates the transpose, and † gives the complex-transpose. Since the outer spin/isospin indices are the same (s), and the inner spin/isospin indices are all s' in the matrix element, we obtain a trace over the projectors and Q as $\mathrm{Tr}\left[P_j Q P_i^\dagger\right]$. Matrix elements in which the spinors are not immediately in an ordering allowing for a trace, such as $\eta_{s'}^T P_j \eta_s \eta_{s'}^T Q \eta_{s'} \eta_{s'}^T P_i^\dagger \eta_s$, also arise in the equation. We form a matrix element over which the trace may be taken by rewriting this example matrix element as $\eta_s^T P_j^T \eta_{s'} \eta_{s'}^T Q \eta_{s'} \eta_{s'}^T P_i^\dagger \eta_s$, where we have transposed the first projection matrix and moved the spinors accordingly. The difference in the signs in Eqs. (4.19) and (4.20) comes from the differing properties of the two projectors P_i and P_i'. Some of these properties are

$$\mathrm{Tr}\Big[P_j P_i^\dagger\Big] = \mathrm{Tr}\Big[P_j' P_i'^\dagger\Big] = \frac{\delta_{ji}}{2}\,, \tag{4.22}$$

$$\mathrm{Tr}\Big[P_j' P_i^\dagger\Big] = 0\,, \tag{4.23}$$

$$\mathrm{Tr}\Big[P_j Q P_i^\dagger\Big] = \mathrm{Tr}\Big[P_j' Q P_i'^\dagger\Big] = \mathrm{Tr}\Big[P_j Q P_i'^\dagger\Big] = \frac{\delta_{ji}}{4}\,. \tag{4.24}$$

Further properties of the trace that we need are

$$\mathrm{Tr}\Big[P_j^T Q P_i^\dagger\Big] = -\,\mathrm{Tr}\Big[P_j Q P_i^\dagger\Big]\,, \tag{4.25}$$

$$\mathrm{Tr}\Big[P_j'^T Q P_i^\dagger\Big] = +\,\mathrm{Tr}\Big[P_j' Q P_i^\dagger\Big]\,, \tag{4.26}$$

where these last two equations are responsible for the sign difference present between Eqs. (4.19) and (4.20). One must also be careful to keep track of sign changes in a matrix element when nucleon Wick contraction lines cross to obtain the right results.

The LO contribution to the amplitude due to the electric-dipole excitation of the nucleus comes from the case where the outgoing unbound nucleons are in a spin triplet and the one allowed isospin triplet state. The overall antisymmetry of the wavefunction is preserved by the fact that the outgoing NN state will have odd orbital angular momentum. The first term in the small-q expansion of the amplitude in Eq. (4.20) corresponds to a P-wave between outgoing nucleons and is

$$s_D^{\mathrm{LO}}(p,q,\theta) = \sqrt{Z}\frac{iM\,p\,q\cos\theta}{(p^2+\gamma^2)^2}\,, \tag{4.27}$$

where the subscript D indicates that it is the amplitude due to the inelastic electric-dipole excitation of the nucleus. This is in agreement with Friar's result in Ref. [48]. While a full electric multipole decomposition of the result was performed in Refs. [48, 114], this was not done in Ref. [115]. Instead, an integration was performed over the complete inelastic structure functions of the nucleus. Here, our structure function calculation implicitly includes all inelastic electric multipole contributions, and the only individual contribution we explicitly extract at present is that of the inelastic electric dipole excitation of the nucleus given in Eq. (4.27). On the other hand, if one only includes dipole excitations, Ref. [47] found that for muonic deuterium these excitations constitute roughly 91% of the total energy shift from inelastic TPE.

For the second diagram in Fig. 4.1, which we label $s_{\mathrm{L},b}$, we find

$$s_{\mathrm{L},b}(\omega,\,\mathbf{q}) = \delta_{ji}\sqrt{Z}\int\frac{d^4l}{(2\pi)^4}\frac{i}{-l_0+E-\frac{\mathbf{l}^2}{2M}+i\epsilon}\frac{i}{-l_0+\omega+E-\frac{(\mathbf{l}+\mathbf{q})^2}{2M}+i\epsilon} \times\frac{i}{l_0-\frac{\mathbf{l}^2}{2M}+i\epsilon}\frac{-iC_0}{1+iC_0\mathcal{I}_0}\,, \tag{4.28}$$

where instead of using the finite cutoff scheme to determine the form of C_0 and $\mathcal{I}_0$ as was used in the previous two chapters, it is convenient instead to proceed with the PDS method described above. The integral $\mathcal{I}_0$ in the PDS scheme is given in Eq. (C.4) in Appendix C. Additionally, we see from the diagrams that $E=-B$. The bubble representing final state interactions in the second diagram of Fig. 4.1 is

$$i\mathcal{A} = \frac{-iC_0}{1+iC_0\mathcal{I}_0} = \frac{4\pi}{M}\frac{i}{-1/a_t - i\sqrt{M\omega-\frac{q^2}{4}-MB}}; \qquad \left[M\omega-\frac{q^2}{4}-MB\geq 0\right]. \tag{4.29}$$

where $a_t = 5.4030\,\mathrm{fm}$ is the np spin triplet scattering length [119]. For the NLO amplitude we also use $r_t = 1.7495\,\mathrm{fm}$. For amplitude insertions after the disintegration of the deuteron, it is appropriate to expand $|\mathbf{k}|\cot\delta_0$ about $|\mathbf{k}|=0$ rather than about the deuteron pole [104].

Next, the integral $\mathcal{I}_2$, which contains the integral over d^4l and the three associated propagators, is given by

$$\mathcal{I}_2 = \frac{i^2M^2}{8\pi}\int_0^1 dy\frac{1}{\left[MB-i\epsilon+y\left(\frac{\mathbf{q}^2}{2}-M\omega\right)-y^2\frac{\mathbf{q}^2}{4}\right]^{1/2}}\,, \tag{4.30}$$

where we first integrated over dl_0 with a complex contour integral in Eq. (4.28). Next, in order to obtain Eq. (4.30), we used Feynman parameterization and the dimensional regularization integral form

$$\int\frac{d^d\ell_E}{(2\pi)^d}\frac{1}{(\ell_E^2+\Delta)^n} = \frac{1}{(4\pi)^{d/2}}\frac{\Gamma(n-d/2)}{\Gamma(n)}\left(\frac{1}{\Delta}\right)^{n-\frac{d}{2}}. \tag{4.31}$$

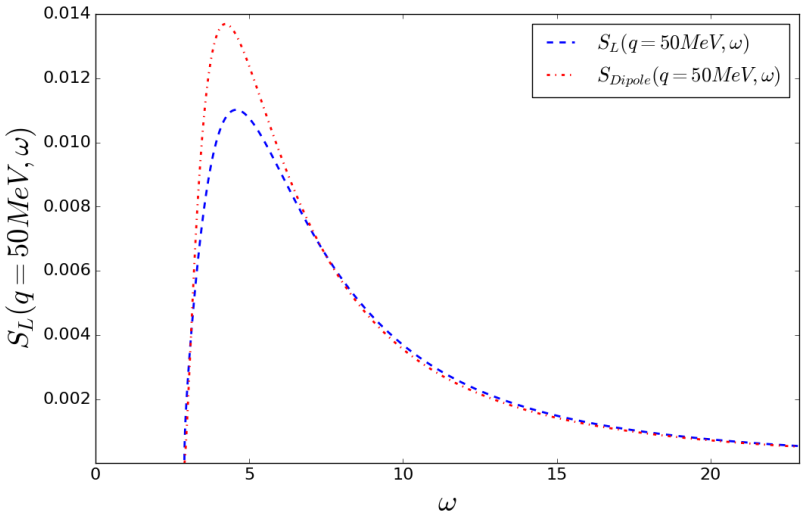

Fig. 4.2 – Comparison of $S_D(q = 50MeV, \omega)$ to $S_L(q = 50MeV, \omega)$. The units of ω are MeV and those of S_L are MeV^{-1}. The form of these structure functions at fixed $|\mathbf{q}|$ compares well with Fig. 2 of Ref. [120]. The wave-function renormalization factor from effective range theory was used in the creation of this plot. From the plot, we see that the effect of implicitly including all electric-multipole contributions serves to reduce the dipole part.

Integrating over dy in Eq. (4.30), we find that the final result for $\mathcal{I}_2$ is given by

$$\mathcal{I}_2 = \left(\frac{-M^2}{8\pi}\right)\left(\frac{1}{q}\right)\left[2i\Big(\ln\Big[-2iM\omega + q\sqrt{4MB + q^2 - 4M\omega - i\epsilon}\Big] - \ln\Big[2q\sqrt{MB} + i(q^2 - 2M\omega)\Big]\Big)\right]. \tag{4.32}$$

This integral result is finite, so no regularization method was needed in its evaluation. Thus, for the second diagram in Fig. 4.1, we arrive at

$$s_{\mathrm{L},b}(\omega,\, \mathbf{q}) = \delta_{ji}\sqrt{Z}i\mathcal{A}\mathcal{I}_2\,, \tag{4.33}$$

The structure function of Eq. (4.6) is then given by the sum of the squared amplitude over outgoing states (an integral in the present case) restricted by the energy-conserving

delta function and is

$$S_L(\mathbf{q},\,\omega) = |Z| \int \frac{dp\, p^2 \sin\theta\, d\theta\, d\phi}{(2\pi)^3} \delta\left(\frac{\mathbf{p}^2}{M} - (\omega - B - \mathbf{q}^2/4M)\right) \times \left[|s_{L,a2}(\mathbf{p},\,\mathbf{q},\,\theta)|^2 + |s_{L,a1}(\mathbf{p},\,\mathbf{q},\,\theta) + s_{L,b}(\mathbf{p},\,\mathbf{q},\,\theta)|^2\right]. \tag{4.34}$$

The square-amplitude in Eq. (4.34) is written in such a way because there is no overlap between the part of the amplitude in the outgoing spin-triplet and isospin-triplet state with that in the outgoing spin-triplet and isospin-singlet state. Thus, $s_{L,a1}$ is summed with $s_{L,b}$ and this sum has its square magnitude taken. But, the square magnitude of $s_{L,a2}$ is taken directly and added to the total square amplitude. The delta function imposed on the integral, $\delta(\mathbf{p}^2/M - (\omega - B - \mathbf{q}^2/4M))$, ensures energy conservation in the process. A further requirement is that the outgoing particles are on-shell, forcing $\mathbf{p}$ to be real. This imposes the relation that $M\omega \geq MB + q^2/4$ for all q. At LO, Eq. (4.34) may be evaluated analytically in its entirety. Further, the energy-conserving delta function in Eq. (4.34) can be rewritten in a more useful form with the relation

$$\delta(g(p)) = \sum_i \frac{\delta(p - p_i)}{|g\prime(p_i)|}, \tag{4.35}$$

where $g'(p_i) = dg(p)/dp$ evaluated at $p = p_i$. The integral over dp is then quite simple, as we replace the energy-conserving delta function with a momentum-conserving one using Eq. (4.35) and obtain

$$\delta\left(\frac{\mathbf{p}^2}{M} - (\omega - B - \mathbf{q}^2/4M)\right) = \frac{M\,\delta\left(|\mathbf{p}| - \sqrt{M(\omega - B - \mathbf{q}^2/4M)}\right)}{2\sqrt{M(\omega - B - q^2/4M)}}. \tag{4.36}$$

Equation (4.36) then allows us to replace each instance of $|\mathbf{p}|$ in Eq. (4.34) with $\sqrt{M(\omega - B) - \mathbf{q}^2/4}$.

To check the form of our results, we compare our longitudinal structure function as a function of ω at fixed $|\mathbf{q}|$ in Fig. 4.2 to Fig. 2 of Ref [120], and the comparison is favorable. Note that the plot does not begin at $\omega = 0$, as we once again impose the restriction that $\omega \geq B + \mathbf{q}^2/4M$ to ensure that the outgoing NN-state is a continuum state. Further, Ref.

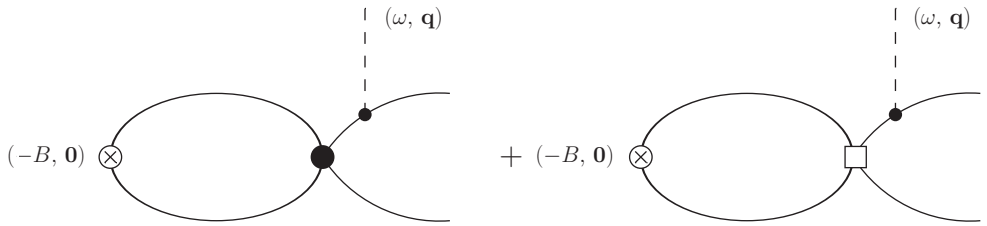

Fig. 4.3 – Diagrams for the NLO longitudinal dipole structure function $S_{\rm D}^{(\rm NLO)}(\omega,\, \mathbf{q})$. The square vertex in the first diagram corresponds to an insertion of the C_2 vertex, and the solid vertex in the second gives an insertion of the NLO $C_{0,0}$ vertex. The dashed line corresponds to an incoming A_0 photon, and we leave off the vertex rule $(-ie)$ for the small solid vertex on the outgoing nucleon legs until the end of the calculation. The crossed circle corresponds to the interpolating field $\mathcal{D}_i = N^T P_i N$ and the LO renormalization factor Z.

[115] gives perhaps one important check that we can use, which is their Eq. (26). This is a sum rule that the longitudinal structure function obeys.

Figure 4.2 includes both the inelastic longitudinal structure function due to all electric-multipoles and the part of the structure function due to dipole excitations. The latter may be found by inserting the amplitude $s_D^{\rm LO}(\mathbf{p},\, \mathbf{q},\, \theta)$ given in Eq. (4.27) into Eq. (4.34) as $|s_D(\mathbf{p},\, \mathbf{q},\, \theta)|^2$ in place of the terms in brackets in the second line of the equation. We obtain the following LO analytical result for the corresponding dipole structure function, $S_D^{\rm LO}(\mathbf{q}, \omega)$:

$$S_D^{\rm LO}(\mathbf{q}, \omega) = \frac{|Z| M^3}{12\pi^2} \frac{(M\omega - MB - q^2/4)^{3/2}}{(M\omega - q^2/4)^4} q^2 \,. \tag{4.37}$$

4.4 Dipole Structure Function at NLO

We perform the NLO calculation of the inelastic longitudinal dipole structure function in this section. For this calculation, we include the interaction term with coupling constant C_2 in Eq. (4.13) and the NLO contact coupling $C_{0,0}$ as in Fig. 4.3 and make use of the loop integrals in Eq. (C.1). Allowing for the same possible outgoing-state projections as we did for

the LO structure function, we find for the diagram with the square C_2 vertex the amplitude

$$s^{\rm NLO}_{L,C_2}(\mathbf{p},\mathbf{q},\theta) = \frac{1}{2}\delta_{ji}\sqrt{Z_{\rm LO}}\left(\frac{C_2 M}{8\pi}(\mu-\gamma)\right)\left[(\gamma^2 - p^2 - \mathbf{p}\cdot\mathbf{q} - q^2/4)S(-\mathbf{p}-\mathbf{q}/2)\right.$$
$$\left. - (\gamma^2 - p^2 + \mathbf{p}\cdot\mathbf{q} - q^2/4)S(\mathbf{p}-\mathbf{q}/2)\right], \tag{4.38}$$

where $S(\pm\mathbf{p}-\mathbf{q}/2)$ are again given by Eq. (4.21), δ_{ji} is from a trace over projectors, and C_2 is given in Eq. (4.18). It is the first term in a series expansion of Eq. (4.38) that gives the dipole contribution at NLO from the C_2 vertex. We find that this is

$$s^{\rm NLO}_{D,C_2} = \frac{1}{2}\delta_{ji}\sqrt{Z_{\rm LO}}\frac{C_2 M}{8\pi}(\mu-\gamma)\left[\frac{4iM\gamma^2 pq\,\cos\theta}{(p^2+\gamma^2)^2}\right]. \tag{4.39}$$

This is only one of three terms we must consider to obtain the NLO inelastic structure function from electric dipole excitations.

One of the two additional terms we consider is the first diagram in Fig. 4.3 corresponding to one insertion of the NLO $C_{0,0}$ vertex. For this diagram we obtain

$$s^{\rm NLO}_{L,C_{0,0}}(\mathbf{p},\mathbf{q},\theta) = \frac{1}{2}\delta_{ji}\sqrt{Z_{\rm LO}}\left(-C_{0,0}\frac{M}{4\pi}(\mu-\gamma)\right)\left[S(-\mathbf{p}-\mathbf{q}/2) - S(\mathbf{p}-\mathbf{q}/2)\right], \tag{4.40}$$

where $C_{0,0}$ is given in Eq. (4.17). We take the first term from the small-q expansion of this result as the dipole contribution from $C_{0,0}$ and obtain

$$s^{\rm NLO}_{D,C_{0,0}}(\mathbf{p},\mathbf{q},\theta) = \delta_{ji}\sqrt{Z_{\rm LO}}\left(-C_{0,0}\frac{M}{4\pi}(\mu-\gamma)\right)\left[\frac{iM\,pq\,\cos\theta}{(p^2+\gamma^2)^2}\right]. \tag{4.41}$$

The third NLO contribution to the dipolar correction multiplies the LO dipole result by $\sqrt{Z_{\rm NLO}}$. We then take this and the contributions of Eqs. (4.39) and (4.41) and include them in the square amplitude. Apart from squaring the term with $\sqrt{Z_{\rm NLO}}$, we only take the cross terms in the NLO couplings, since terms $O(\rho_d^2)$ is N2LO. The squared amplitude that we insert into Eq. (4.34) is then

$$|s^{\rm NLO}_D|^2 = |Z_{\rm NLO}|\,\left|s^{\rm LO}_D(\mathbf{p},\mathbf{q},\theta)\right|^2 + 2|Z_{\rm LO}|\left(s^{\rm LO\,*}_D(\mathbf{p},\mathbf{q},\theta)s^{\rm NLO}_{D,C_2}(\mathbf{p},\mathbf{q},\theta)\right)$$
$$+ 2|Z_{\rm LO}|\left(s^{\rm LO\,*}_D(\mathbf{p},\mathbf{q},\theta)s^{\rm NLO}_{D,C_{0,0}}(\mathbf{p},\mathbf{q},\theta)\right), \tag{4.42}$$

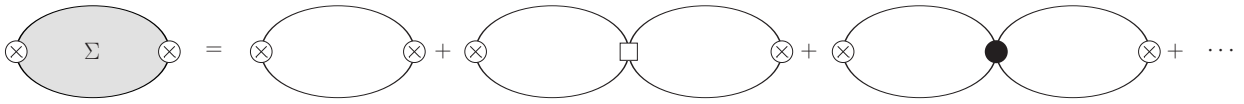

Fig. 4.4 – Diagrams for the irreducible bubble Σ up to NLO in ρ_d. The first diagram on the RHS of the equality is the LO bubble, and the second and third diagrams on the RHS are NLO in ρ_d. The square vertex corresponds to the insertion of the C_2 operator, and the solid dot corresponds to $C_{0,0}$. The crossed circle represents the interpolating field $\mathcal{D}_i = \psi^T P_i \psi$.

where the factors of 2 arise from the fact that there are two of each of those cross terms.

For the final NLO dipole result, we find that it is only the LO dipole part $s_D^{\rm LO}(\mathbf{p}, \mathbf{q}, \theta)$ multiplied by $Z_{\rm NLO}$ that contributes, and the C_2 and $C_{0,0}$ terms cancel. This exactly matches the NLO term in a small-ρ_d expansion of the effective range theory wavefunction renormalization, which is very reasonable because at this order we include no physics that is not present in the effective range expansion. At N2LO this will no longer be the case, as SD-mixing in the deuteron enters the calculation. The final NLO portion of the inelastic electric dipole structure function we therefore find as

$$S_D^{\rm NLO}(\mathbf{q}, \omega) = \rho_d \gamma |Z_{\rm LO}| \frac{M^3}{12\pi^2} \frac{(M\omega - \gamma^2 - q^2/4)^{3/2}}{(M\omega - q^2/4)^4} q^2 \,. \tag{4.43}$$

This result looks like Eq. (4.37) apart from a new multiplicative factor of $\rho_d \gamma$. Thus, the total result up to NLO we write $S_D^{\rm LO}(\mathbf{q}, \omega)[1 + \rho_d \gamma]$, which matches the small-ρ_d expansion of the wavefunction renormalization factor from effective range theory as previously mentioned. The result in Eq. (4.43) requires knowledge of the wavefunction renormalization factor up to NLO in $\mathcal{Q} \sim \rho_d \gamma$.

4.5 Wavefunction Renormalization

The two-point function Σ related to the two-point irreducible Green's function $G(\overline{E})$ is necessary for the determination of the wave-function renormalization factor and is given in Fig. 4.4. The renormalization factor ensures that the ingoing wave-function in an amplitude calculation has the same normalization as an ingoing deuteron wave-function. Chen, Rupak

and Savage [104] give the renormalization factor in general as

$$Z = i \left[\frac{1 + \frac{E_{\rm pole}}{2M}}{d\Sigma\left(\overline{E}\right)/dE} \right]_{\overline{E}\to -B} , \tag{4.44}$$

where $E_{\rm pole} = -B + \mathbf{p}^2/4M$ and $\overline{E} = E - p^2/4M$, and $\Sigma(\overline{E}) = \sum_{n=1}^{\infty} \Sigma_n(\overline{E})$ is an order-by-order expansion of Σ in the parameter $\mathcal{Q} \sim \rho_d/\mu$. The first bubble on the RHS of the equality in Fig. 4.4 gives

$$\Sigma_1(\overline{E}) = -i\frac{M}{4\pi}(\mu - \sqrt{-M\overline{E} - i\epsilon}) . \tag{4.45}$$

We have used a notation similar to that of Ref. [121], but the convention we use in Eq. (4.44) for the renormalization factor differs from that reference.

At NLO, there are two contributions. In Fig. 4.4, these are given by the second and third diagrams on the RHS of the equality. The square vertex in the second diagram on the RHS corresponds to an insertion of the C_2 vertex, while the solid dot in the third diagram corresponds to an insertion of the NLO part of C_0, or $C_{0,0}$. The dots indicate higher order corrections to the irreducible two-point function. The Feynman rule for the square vertex is $-i\frac{C_2}{8}[\mathbf{p}^2 + \mathbf{k}^2]$, where $\mathbf{p}$ is the relative momentum of the ingoing nucleons and $\mathbf{k}$ that of the outgoing nucleons. For the solid dot, the vertex rule is $-iC_{0,0}$. Using the general integral form of Eq. (C.4), we obtain the total NLO contribution

$$\Sigma_2(\overline{E}) = \frac{iC_2M^2}{16\pi^2}\left(M\overline{E}\right)\left(\mu - \sqrt{-M\overline{E} - i\epsilon}\right)^2 + \frac{iC_{0,0}M^2}{16\pi^2}\left(\mu - \sqrt{-M\overline{E} - i\epsilon}\right)^2 . \tag{4.46}$$

We calculate the derivative of the sum of Eqs. (4.45) and (4.46) with respect to E and take $\overline{E} \to -B$ for use in Eq. (4.44). This yields

$$\begin{aligned} \left.\frac{d\Sigma(\overline{E})}{dE}\right|_{\overline{E}\to -B} &= -\frac{iM^2}{8\pi\gamma} + \frac{i\rho_d M^2}{8\pi}\left[1 - \frac{\gamma}{\mu - \gamma}\right] + \frac{i\rho_d M^2\gamma}{8\pi(\mu-\gamma)} , \\ &= -\frac{iM^2}{8\pi\gamma} + \frac{i\rho_d M^2}{8\pi} , \end{aligned} \tag{4.47}$$

where $\Sigma(\overline{E}) = \Sigma_1(\overline{E}) + \Sigma_2(\overline{E})$. Inserting Eq. (4.47) into Eq. (4.44) and dropping $E_{\rm pole}/2M$ since $\gamma^2/2M^2 \approx 0.0011$, we find that up to NLO in ρ_d

$$Z = \frac{i}{-\frac{iM^2}{8\pi\gamma} + \frac{i\rho_d M^2}{8\pi}}\,, \tag{4.48}$$

$$\approx -\frac{8\pi\gamma}{M^2}\left[1 + \rho_d\gamma + \rho_d^2\gamma^2 + \cdots\right]\,, \tag{4.49}$$

where we expanded Eq. (4.48) in small ρ_d to obtain Eq. (4.49). In the EFT calculation, this result for the wave-function renormalization factor is plugged into $|Z|$ in Eq. (4.34). For now, we only include the leading term in Eq. (4.49) to obtain the LO result for the energy shift in EFT.

4.6 Additional Contributions

We next look at a few additional contributions beyond those from inelastic electric multipole parts of the structure function, after which we present the numerical results of our study. As discussed previously, Refs. [114, 122] perform a multipole decomposition of the structure function and from that include the leading electric dipole term, the Zemach related (inelastic) term, monopole term, quadrupole term and what they call an interference term δ_{D1D3}. Additionally, Coulomb distortion corrections, relativistic longitudinal and transverse corrections, and three different finite-nucleon-size corrections are detailed in Ref. [122]. The expressions in that source only have energy dependence in their structure function because of the particular nature of their approach, in which they have discretized the continuum such that all of the states are eigenstates of their Hamiltonian expressed in the harmonic oscillator basis.

Additionally, Ref. [115] includes what they call the spin-current interaction, which is related to the proton and neutron magnetic moments and allows for the spin-flip of the nucleons. They found that it does not contribute significantly in their approach, though in Ref. [48], Friar found that it was important to include these effects. Similarly, the authors of Ref. [114] calculated the contribution from spin-flip and found that this term, which they label δ_{M1}, is important for μ-D since the deuteron is a nucleus with total angular momentum

$J = 1$ in the ground state. This contribution was found to be less important in μ-^{4}He$^+$ than in μ-D [122]. The energy shift δ_{M1} is expressed in terms of the magnetic response function as

$$\delta_M = \frac{1}{3} m_r^3 \alpha^5 \left(\frac{g_p - g_n}{4 m_p} \right)^2 \int_{\omega_{\rm th}}^{\infty} d\omega \sqrt{\frac{\omega}{2 m_r}} S_{M1}(\omega) \,, \tag{4.50}$$

where m_p is the proton mass, $g_p = 5.586$, and $g_n = -3.826$. The magnetic dipole operator $M1$ is given by Pachucki in Ref. [123].

Another basic formula of interest in Ref. [114] is for the Coulomb distortion correction, which they label as δ_C.

$$\delta_C = -\frac{2\pi}{9} m_r^3 \alpha^6 \int_{\omega_{\rm th}}^{\infty} d\omega \frac{m_r}{\omega} \ln \frac{2 m_r \alpha^2}{\omega} S_{D1}(\omega) \,. \tag{4.51}$$

This equation incorporates the electric-dipole response function. This is also the only term that does not contribute at $O(\alpha^5)$, and is instead proportional to $\alpha^6 \ln \alpha$. Coulomb distortion is especially important at low photon momentum.

One other significant contribution to the TPE part of the nuclear polarization correction to the Lamb shift is due to the third *elastic* Zemach moment and Ref. [124] gives this Zemach term as

$$\delta_{\rm Zem}^A = -\frac{m_r^4 (Z\alpha)^5}{24} \langle r^3 \rangle_{(2)} \,, \tag{4.52}$$

where $\langle r^3 \rangle_{(2)}$ is the 3rd nuclear Zemach moment. Then, from Ref. [125] we find the third nuclear Zemach moment in muonic Hydrogen expressed as

$$\langle r^3 \rangle_{(2)} = \frac{48}{\pi} \int_0^{\infty} \frac{dq}{q^4} \left(G_{\rm E}^2(q^2) - 1 + q^2 \langle r^2 \rangle_p / 3 \right) \,. \tag{4.53}$$

This is somewhat of a simplified form developed by Pachucki [126]. In Eq. (4.53), the factor of 1 cancels against $G_E(0)$, and the $q^2 \langle r^2 \rangle_p / 3$ term cancels the first q^2-dependent term in a low q expansion of $G_E(q)$. One must take $\langle r^2 \rangle_p$, or for our purposes $\langle r^2 \rangle_d$, from experiments. This third Zemach moment is calculable in and provides a very significant correction to the Lamb shift in muonic atoms. This elastic Zemach term largely cancels against the inelastic one implicitly contained in our structure function calculation, and the cancellation is exact when point nucleons are assumed.

Some minor contributions also enter into the calculation of the total TPE contribution to the Lamb shift in muonic deuterium. One is SD mixing in the deuteron, and Ref. [115] found that including the D-wave part only adds a correction to the longitudinal part of the energy shift of around 1%. Another very small contribution comes from pion exchange in the deuteron. However, Ref. [47] found that the inclusion of meson exchange currents in the Paris potential only adds about a 1.3% correction to the very small transverse part of the energy shift in the Coulomb gauge, meaning that such effects would constitute a roughly 0.01% correction to our results. Thus, we do not take them into consideration.

4.7 Numerical Results

Here, we present our results for various nuclear polarization corrections to the 2S-2P energy shift due to TPE. In the results section of Ref. [114], the authors reproduce the experimental binding energy of the deuteron with their two different approaches (AV18 and χEFT). We use this same value for the deuteron binding energy here, which is 2.224573(2) MeV.

Here we provide our results for the energy shift in muonic deuterium up to NLO in $\mathcal{Q} \sim \rho_d \gamma^2/\mu$, where μ is the renormalization scale in our problem, which we choose to be the pion mass m_π. In the Coulomb gauge, the transverse and seagull terms do not yet contribute at this order and so are not included here. Terms that are calculable in our framework, but have not yet been calculated, are δ_{M1}, the elastic third Zemach moment contribution, that from SD-mixing in the deuteron, and the contributions from the transverse and seagull terms in Eq. (4.7).

The first two results we present are the shift due to dipole excitations and the shift due to all inelastic electric multipole excitations. We first plug the dipole structure function in Eq. (4.37) into Eq. (4.54) to obtain the contribution to the 2S-2P Lamb shift from dipole excitations. Then, to extract the full inelastic longitudinal contribution to the energy shift in the Coulomb gauge, we isolate the longitudinal part of Eq. (4.7):

$$\Delta\epsilon_{n0,L} = -8\alpha^2 R_{n0} |\phi_{n0}(0)|^2 \int_0^\infty dq \int_{\omega_{th}}^\infty d\omega \left[K_L(\omega, \mathbf{q}) S_L(\omega, \mathbf{q})\right] , \tag{4.54}$$

Table 4.1 – Energy Shift Results

energy shifts	≠EFT	Ref. [48]	≠EFT Total
$\delta_D^{(\mathrm{ERE,NR})}$	-1.925	-1.925	–
$\delta_D^{(\mathrm{ERE,REL})}$	-1.857	-1.888	–
$\delta_{D,\mathrm{LO}}^{(\mathrm{EFT,NR})}$	-1.139	–	-1.139
$\delta_{D,\mathrm{NLO}}^{(\mathrm{EFT,NR})}$	-0.465	–	-1.604
$\delta_{L,\mathrm{LO}}^{(\mathrm{EFT,NR})}$	-0.962	–	-0.962

All values in the table are given in units of meV. The top portion of the table compares our LO dipole contribution with the results of Ref. in the non-relativistic (NR) and relativistic case. Below that, we present the EFT results for the dipole contribution up to NLO. The bottom portion of the table contains the inelastic longitudinal contribution to the shift from all electric multipoles at LO.

We perform the integration of Eq. (4.54) numerically. If the dq-integral is carried out from $0 \to \infty$, this places a lower limit on the $d\omega$-integral coming from the requirement that the outgoing nucleons from the disintegrated deuteron in the structure function calculation have energy $E \geq 0$, i.e. are in the continuum. We find that $\omega_{th} = B + \mathbf{q}^2/4M$.

To compare our results for the energy shift due to an inelastic dipole transition from the deuteron ground state to a continuum state to previous zero-range literature, we set $|Z| = 8\pi\gamma/M^2(1-\gamma\rho_d)$, which is from *effective range theory*, to compare our results with the zero-range result of Ref. [48]. In that paper, Friar obtained a magnitude of the energy shift he labels $\Delta E_{\mathrm{pol}}^{\mathrm{C1}}$ of 1.925meV. To compare to this result, we set $R_{n0} = 1$ and use the non-relativistic kernel of Eq. (4.10) to obtain

$$\Delta\epsilon_{n0,D}^{(\mathrm{NR})} = -1.925\,\mathrm{meV}, \tag{4.55}$$

which is identical to the corresponding result of Friar in Ref. [48] and is listed as $\delta_D^{(\mathrm{ERE,NR})}$ in Table 4.1. Next, using the kernel of Eq. (4.9) for a fully relativistic muon, we obtain a value

$$\delta_{n0,D} = -1.857\,\mathrm{meV}. \tag{4.56}$$

This compares favorably with the result in Ref. [48], where Friar found, after including only one correction of relativistic origin, which he labels $\Delta E_{\mathrm{pol}}^{\text{sub-C1}}$, the corrected energy shift from

a dipole transition to be of magnitude 1.888 meV. The difference in signs of the two results is purely a matter of convention.

If we return to our EFT expansion and use the LO wavefunction renormalization in the calculation of the shift due to all inelastic electric multipole contributions, we find

$$\delta_{L,\mathrm{LO}}^{(\mathrm{NR})} = -0.9622\,\mathrm{meV}\,, \tag{4.57}$$

where this is the result of inserting the longitudinal structure function in Eq. (4.34) into Eq. (4.7) and integrating it with the non-relativistic kernel of Eq. (4.10). This does not include the elastic Zemach contribution. Further, the result in Eq. (4.57) cannot yet be compared to the result for $\delta_{\mathrm{pol}}^{A}$ in Ref. [114] because we have not added the other necessary corrections to it at present.

As an additional comparison, we note that a list of all contributions considered in Ref. [114] is given in their Table 3, and the dipole part therein is $\delta_{D1}^{(0)} = -1.907$ for the AV18 potential and $\delta_{D1}^{(0)} = -1.912$ for the chiral EFT potential N^{3}LO-EM, also using a fully relativistic integration kernel. Their result is larger than ours or Friar's for the dipole term with relativistic corrections. They give a total value for the polarization corrections as follows, including the value of $\delta_{\mathrm{pol}}^{N}$ for nucleon structure corrections from Ref. [127]:

$$\delta_{\mathrm{pol}}^{A} = -1.239 \pm 0.005\,\mathrm{meV}\,, \tag{4.58}$$

$$\delta_{\mathrm{Zem}} = -0.424 \pm 0.003\,\mathrm{meV}\,, \tag{4.59}$$

$$\delta_{\mathrm{pol}}^{N} = -0.027 \pm 0.002\,\mathrm{meV}\,, \tag{4.60}$$

giving a total two-photon exchange polarization contribution to the μD Lamb shift of [114]

$$\delta_{\mathrm{TPE}} = -1.690 \pm 0.020\,\mathrm{meV}\,. \tag{4.61}$$

Hernandez *et al.* take a quadrature sum of errors and include a $\sim 1\%$ uncertainty from atomic physics, as well as the spread in results from the nuclear potentials of $\sim 0.5\%$ and a 0.3% portion from the convergence of χEFT. Their results benefit the calculation of the deuteron charge radius from ongoing μD Lamb shift experiments. They have agreement to

about 0.6% with Pachucki in Ref. [123], but that agreement is partially accidental, since several of the individual terms differ by percentages larger than this.

4.8 Uncertainty Estimates

A major reason the $\not\pi$EFT method we use is helpful for this problem is that, in addition to having far fewer parameters than many other related polarization correction studies, it provides an excellent way to track uncertainties in the problem. However, at the time of writing, we have not yet analyzed the uncertainties in the calculations above. We would expect an error estimate on our LO results of approximately 70% based on a comparison of our LO EFT result for the dipole part to the non-relativistic ERE result for the same part of the energy shift and less than 20% at NLO.

The error estimates in Ref. [47] seem somewhat non-rigorous compared to what an EFT approach provides. It consists of accounting for the spread in the results of the various models used in this work, rather than a fundamental look at the uncertainties, like that of Hernandez *et al.* in Ref. [114]. Another recent estimate of the nuclear structure corrections given by Carlson *et al.* [127] has a rather large uncertainty compared to other modern results of $\sim 35\%$.

Leidemann and Rosenfelder [47] gave an early attempt to estimate the theoretical error in nuclear polarization of the deuteron by the muon using several of the NN potentials available at the time of their study. They found a potential dependence of less than 2%, but that may not be quite right, as this work did not include Coulomb distortion contributions. Uncertainty estimates were considered from a variety of sources in Ref. [114], which used modern potentials from chiral effective field theory (χEFT) [128, 129]. Additionally, Pachucki noted that the atomic physics contributions to uncertainty in the TPE calculations are $\sim 1\%$ [123]. After completing our calculations to N2LO, this is at the order of precision which we hope to achieve.

4.9 Conclusion of Nuclear Polarization Section

In this chapter, we have calculated the nuclear polarization corrections to the Lamb shift in muonic deuterium arising from two-photon exchange at LO in $\not\pi$EFT. We accomplished this by replacing the expression for the forward virtual Compton amplitude in Eq. (4.2) with the inelastic structure functions of the deuteron following the method of Ref. [46]. Working in the Coulomb gauge, we calculated the most significant of these contributions, which come from the longitudinal structure function. We compared our results for the energy shift due to inelastic electric dipole excitations of the deuteron to those of Ref. [48] and found excellent agreement.

In the future, we plan to extend these results to N2LO in the power counting parameter $\mathcal{Q} \sim \rho_d \gamma^2/\mu$. This will include relativistic corrections, S-D mixing in the deuteron, corrections due to a finite deuteron effective range ρ_d, and contributions from the transverse and seagull portions of the inelastic structure function. Additionally, this approach can be extended to the three-body problem, for example polarization corrections in muonic tritium and ^{3}He.

Chapter 5

Discussion

In this dissertation, we applied the ∉EFT to a homogeneous, balanced gas of ultracold fermions in two spin states, to the study of universal physics in the heteronuclear three-body problem, and to obtain nuclear polarization corrections to the 2S-2P Lamb shift in muonic deuterium. In each case, a separation of scales in the problem allows for a systematic expansion of the EFT to give results that increase in precision as higher orders in the EFT expansion are included.

For the ultracold Fermi gas in Ch. 2 the resulting finite range corrections are found to be important in the description of the large-momentum behavior of the momentum distribution of the gas. Range corrections and a finite intraspecies scattering length were not included in the heteronuclear system studied in Ch. 3, though this would be an interesting pursuit shedding light on the low-a region of experimental data. In that system, it was discovered that finite temperature effects obscure the S-wave universal physics severely in extremely mass-imbalanced gases, rendering them less suitable for the observation of Efimov features than previously thought. And in Ch. 4, previous results for the inelastic electric dipole portion of the structure function and the resulting two-photon-exchange correction to the Lamb shift were reproduced. Further, LO ∉EFT results for all electric-multipole contributions implicitly contained in our EFT structure function and the electric dipole part up to NLO in the deuteron effective range are provided. N2LO calculations are a necessary further application of this work and will provide additional insight into the yet-unsolved proton and deuteron radius puzzles.

Bibliography

[1] E. Braaten and H.-W. Hammer, Phys. Rev. A **67**, 042706 (2003). 1, 2, 6, 45

[2] E. Braaten and H.-W. Hammer, Phys. Rept. **428**, 259 (2006). 2, 48, 56

[3] V. Efimov, Phys. Lett. **33B**, 563 (1970). 2, 44

[4] D. S. Petrov and F. Werner, Phys. Rev. A **92**, 022704 (2015). 2, 57, 64, 67

[5] S. B. Emmons, D. Kang, B. Acharya, and L. Platter, Phys. Rev. A **96**, 032706 (2017). 2, 8, 59

[6] C. Ji, E. Braaten, D. R. Phillips, and L. Platter, Phys. Rev. **A92**, 030702 (2015). 2, 67

[7] B. Acharya, C. Ji, and L. Platter, Phys. Rev. A **94**, 032702 (2016), 3

[8] D. B. Kaplan, M. J. Savage, and M. B. Wise, Nucl. Phys. **B478**, 629 (1996). 3, 15, 16

[9] U. van Kolck, Nucl. Phys. **A645**, 273 (1999). 3, 15

[10] E. Ryberg, C. Forssén, H.-W. Hammer, and L. Platter, Phys. Rev. C **89**, 014325 (2014). 4

[11] K. G. Wilson, Phys. Rev. D **3**, 1818 (1971). 4

[12] D. B. Kaplan, M. J. Savage, and M. B. Wise, Phys. Lett. **B424**, 390 (1998). 4, 76, 111

[13] P. F. Bedaque, H.-W. Hammer, and U. van Kolck, Phys. Rev. Lett. **82**, 463 (1999). 4, 46, 48, 49, 50

[14] M. Inguscio, W. Ketterle, and C. Salomon, Proc. Int. Sch. Phys. Fermi **164**, pp.1 (2007). 5

[15] S. Tan, Annals of Physics **323**, 2952 (2008), ISSN 0003-4916. 5, 11, 20

[16] S. Tan, Annals of Physics **323**, 2971 (2008), ISSN 0003-4916. 5, 11, 20

[17] S. Tan, Annals of Physics **323**, 2987 (2008), ISSN 0003-4916. 5, 11, 12, 20, 21

[18] K. G. Wilson, Phys. Rev. **179**, 1499 (1969). 5, 12, 26

[19] L. P. Kadanoff, Phys. Rev. Lett. **23**, 1430 (1969). 5, 12, 26

[20] E. Braaten and L. Platter, Phys. Rev. Lett. **100**, 205301 (2008). 5, 12, 14, 22, 28, 36, 43

[21] E. Braaten, D. Kang, and L. Platter, Phys. Rev. A **78**, 053606 (2008). 5, 12, 22

[22] S. B. Emmons, D. Kang, and L. Platter, Phys. Rev. A **94**, 043615 (2016). 6

[23] P. Courteille, R. S. Freeland, D. J. Heinzen, F. A. van Abeelen, and B. J. Verhaar, Phys. Rev. Lett. **81**, 69 (1998). 6

[24] S. L. Cornish, N. R. Claussen, J. L. Roberts, E. A. Cornell, and C. E. Wieman, Phys. Rev. Lett. **85**, 1795 (2000). 6

[25] S. Inouye, M. R. Andrews, J. Stenger, H.-J. Miesner, D. Stamper-Kurn, and W. Ketterle, Nature **392**, 151 (1998). 6

[26] T. Kraemer, M. Mark, P. Waldburger, J. G. Danzl, C. Chin, B. Engeser, A. D. Lange, K. Pilch, A. Jaakkola, H.-C. Nägerl, et al., Nature **440** (2006). 7

[27] N. Gross, Z. Shotan, S. Kokkelmans, and L. Khaykovich, Phys. Rev. Lett. **103**, 163202 (2009). 7

[28] S. E. Pollack, D. Dries, and R. G. Hulet, Science **326**, 1683 (2009). 7

[29] N. Gross, Z. Shotan, S. Kokkelmans, and L. Khaykovich, Phys. Rev. Lett. **105**, 103203 (2010). 7

[30] T. B. Ottenstein, T. Lompe, M. Kohnen, A. N. Wenz, and S. Jochim, Physical Review Letters **101**, 203202 (pages 4) (2008). 8

[31] J. H. Huckans, J. R. Williams, E. L. Hazlett, R. W. Stites, and K. M. O'Hara, Phys. Rev. Lett. **102**, 165302 (2009). 8

[32] J. R. Williams, E. L. Hazlett, J. H. Huckans, R. W. Stites, Y. Zhang, and K. M. O'Hara, Phys. Rev. Lett. **103**, 130404 (pages 4) (2009). 8

[33] S. Floerchinger, R. Schmidt, and C. Wetterich, Phys. Rev. A **79**, 053633 (pages 5) (2009). 8

[34] P. Naidon and M. Ueda, Phys. Rev. Lett. **103**, 073203 (pages 4) (2009). 8

[35] E. Braaten, H.-W. Hammer, D. Kang, and L. Platter, Phys. Rev. Lett. **103**, 073202 (2009). 8

[36] E. Braaten, H.-W. Hammer, D. Kang, and L. Platter, Phys. Rev. A **81**, 013605 (2010). 8

[37] H.-W. Hammer, D. Kang, and L. Platter, Phys. Rev. A **82**, 022715 (2010). 8

[38] R. S. Bloom, M.-G. Hu, T. D. Cumby, and D. S. Jin, Phys. Rev. Lett. **111**, 105301 (2013). 8, 45, 57, 61, 62, 63, 64, 65

[39] E. Braaten, H.-W. Hammer, D. Kang, and L. Platter, Phys. Rev. A **78**, 043605 (2008). 8, 49, 54, 55, 58, 60

[40] K. Helfrich and H.-W. Hammer, J. Phys. **B44**, 215301 (2011). 8, 47, 55, 56

[41] K. Helfrich, H.-W. Hammer, and D. S. Petrov, Phys. Rev. A **81**, 042715 (2010),. 8, 47, 50, 52, 53, 57, 61, 62

[42] J. J. Krauth, K. Schuhmann, M. Abdou Ahmed, F. Amaro, P. Amaro, F. Biraben, J. M. R. Cardoso, M. L. Carvalho, D. S. Covita, A. Dax, et al., arXiv:1706.00696v2 (2017). 9, 68

[43] A. Beyer, L. Maisenbacher, A. Matveev, R. Pohl, K. Khabarova, A. Grinin, T. Lamour, D. C. Yost, T. W. Hänsch, N. Kolachevsky, et al., Science **358**, 79 (2017), ISSN 0036-8075. 9

[44] R. Pohl, F. Nez, T. Udem, A. Antognini, A. Beyer, H. Fleurbaey, A. Grinin, T. W. Hänsch, L. Julien, F. Kottmann, et al., Metrologia **54**, L1 (2017). 9, 68

[45] O. Hernandez, A. Ekström, N. N. Dinur, C. Ji, S. Bacca, and N. Barnea, Phys. Lett. B **778**, 377 (2018), ISSN 0370-2693. 9, 68, 70

[46] R. Rosenfelder, Nucl. Phys. A **393**, 301 (1983), ISSN 0375-9474. 10, 70, 71, 72, 93

[47] W. Leidemann and R. Rosenfelder, Phys. Rev. C **51**, 427 (1995). 10, 70, 71, 72, 73, 74, 79, 89, 92

[48] J. L. Friar, Phys. Rev. C **88**, 034003 (2013). 10, 70, 79, 87, 90, 93

[49] A. Galea, T. Zielinski, S. Gandolfi, and A. Gezerlis, Journal of Low Temperature Physics **189**, 451 (2017), ISSN 1573-7357. 11

[50] M.-I. Trappe, P. Grochowski, M. Brewczyk, and K. Rzazewski, Phys. Rev. A **93**, 023612 (2016). 11

[51] A. M. Polyakov, Soviet Physics–JETP **30**, 151 (1970). 12, 26

[52] F. Werner and Y. Castin, Phys. Rev. A **86**, 013626 (2012). 12, 21, 22, 43

[53] W. D. Goldberger and I. Z. Rothstein, Phys. Rev. A **85**, 013613 (2012). 12, 27

[54] Z. Yu, J. H. Thywissen, and S. Zhang, Phys. Rev. Lett. **115**, 135304 (2015). 19

[55] P. Zhang, S. Zhang, and Z. Yu, Phys. Rev. A **95**, 043609 (2017). 19

[56] J. Carlson, S. Gandolfi, K. E. Schmidt, and S. Zhang, Phys. Rev. A **84**, 061602 (2011). 19, 21, 25

[57] J. Carlson, S. Gandolfi, and A. Gezerlis, Prog. of Theor. and Exp. Phys. **2012**, 01A209 (2012). 19, 21, 24, 25, 43

[58] F. Werner, Phys. Rev. A **78**, 025601 (2008). 21

[59] E. Braaten, Lect. Notes Phys. **836**, 193 (2012). 23, 36

[60] G. B. Partridge, K. E. Strecker, R. I. Kamar, M. W. Jack, and R. G. Hulet, Phys. Rev. Lett. **95**, 020404 (2005). 24

[61] F. Werner, L. Tarruell, and Y. Castin, Eur. Phys. J. B **68**, 401 (2009). 24

[62] N. Navon, S. Nascimbène, F. Chevy, and C. Salomon, Science **328**, 729 (2010). 24

[63] E. D. Kuhnle, H. Hu, X.-J. Liu, P. Dyke, M. Mark, P. D. Drummond, P. Hannaford, and C. J. Vale, Phys. Rev. Lett. **105**, 070402 (2010). 24

[64] G. Veeravalli, E. Kuhnle, P. Dyke, and C. J. Vale, Phys. Rev. Lett. **101**, 250403 (2008). 24

[65] Y. Sagi, T. E. Drake, R. Paudel, and D. S. Jin, Phys. Rev. Lett. **109**, 220402 (2012). 24

[66] J. T. Stewart, J. P. Gaebler, T. E. Drake, and D. S. Jin, Phys. Rev. Lett. **104**, 235301 (2010). 24

[67] C. Lobo, I. Carusotto, S. Giorgini, A. Recati, and S. Stringari, Phys. Rev. Lett. **97**, 100405 (2006). 24

[68] R. Combescot, S. Giorgini, and S. Stringari, EPL **75**, 695 (2006). 24

[69] T. Abe and R. Seki, Phys. Rev. C **79**, 054003 (2009). 24

[70] S.-Q. Su, D. E. Sheehy, J. Moreno, and M. Jarrell, Phys. Rev. A **81**, 051604 (2010). 24

[71] J. E. Drut, T. A. Lähde, and T. Ten, Phys. Rev. Lett. **106**, 205302 (2011). 24

[72] S. Hoinka, M. Lingham, K. Fenech, H. Hu, C. J. Vale, J. E. Drut, and S. Gandolfi, Phys. Rev. Lett. **110**, 055305 (2013). 24

[73] J.-W. Chen and E. Nakano, Phys. Rev. A **75**, 043620 (2007). 24

[74] F. Palestini, A. Perali, P. Pieri, and G. C. Strinati, Phys. Rev. A **82**, 021605 (2010). 24

[75] K. Van Houcke, F. Werner, E. Kozik, N. Prokof'ev, and B. Svistunov, arXiv:1303.6245 (2013). 24

[76] S. Gandolfi, K. E. Schmidt, and J. Carlson, Phys. Rev. A **83**, 041601 (2011). 24

[77] J. Collins, *Renormalization* (Cambridge University Press, New York, 1986). 26

[78] Y. Nishida and D. T. Son, *Unitary Fermi Gas, epsilon Expansion, and Nonrelativistic Conformal Field Theories* (Springer Berlin Heidelberg, Berlin, Heidelberg, 2012), pp. 233–275. 43

[79] E. Braaten, D. Kang, and L. Platter, Phys. Rev. Lett. **106**, 153005 (2011). 43

[80] G. Barontini, C. Weber, F. Rabatti, J. Catani, G. Thalhammer, M. Inguscio, and F. Minardi, Phys. Rev. Lett. **103**, 043201 (2009). 44, 45

[81] E. Nielsen and J. H. Macek, Phys. Rev. Lett. **83**, 1566 (1999). 44

[82] V. Efimov, Nucl. Phys. A **210**, 157 (1973). 44, 48, 66

[83] H.-W. Hammer and L. Platter, Annu. Rev. Nucl. Part. Sci. **60**, 207 (2010). 44

[84] S.-K. Tung, K. Jiménez-García, J. Johansen, C. V. Parker, and C. Chin, Phys. Rev. Lett. **113**, 240402 (2014). 45

[85] R. Pires, J. Ulmanis, S. Häfner, M. Repp, A. Arias, E. D. Kuhnle, and M. Weidemüller, Phys. Rev. Lett. **112**, 250404 (2014). 45

[86] G. V. Skorniakov and K. A. Ter-Martirosian, Sov. Phys. JETP **4**, 648 (1957). 45

[87] P. F. Bedaque, H.-W. Hammer, and U. van Kolck, Nucl. Phys. A **646**, 444 (1999). 45, 49

[88] C. Ji, D. R. Phillips, and L. Platter, Annals Phys. **327**, 1803 (2012). 45, 67

[89] O. I. Kartavtsev and A. V. Malykh, JETP Letters **86**, 625 (2008), ISSN 1090-6487. 48

[90] H.-W. Hammer and T. Mehen, Nucl. Phys. A **690**, 535 (2001). 49

[91] J. H. Hetherington and L. H. Schick, Phys. Rev. **137**, B935 (1965). 49

[92] B. Acharya, C. Ji, and L. Platter, Phys. Rev. A **94**, 032702 (2016). 50, 62, 67

[93] E. Braaten, H. W. Hammer, and G. P. Lepage, Phys. Rev. **A95**, 012708 (2017). 51

[94] E. Braaten, H. W. Hammer, and G. P. Lepage, Phys. Rev. **D94**, 056006 (2016). 51

[95] B. D. Esry, C. H. Greene, and H. Suno, Phys. Rev. A **65**, 010705 (2001). 55

[96] J. Ulmanis, S. Häfner, R. Pires, F. Werner, D. S. Petrov, E. D. Kuhnle, and M. Weidemüller, Phys. Rev. A **93**, 022707 (2016). 57

[97] J. P. D'Incao and B. D. Esry, Phys. Rev. A **73**, 030702 (2006). 60, 65

[98] J. J. Zirbel, K.-K. Ni, S. Ospelkaus, J. P. D'Incao, C. E. Wieman, J. Ye, and D. S. Jin, Phys. Rev. Lett. **100**, 143201 (2008). 62

[99] Y. Wang, J. Wang, J. P. D'Incao, and C. H. Greene, Phys. Rev. Lett. **109**, 243201 (2012). 62

[100] L. J. Wacker, N. B. Jørgensen, D. Birkmose, N. Winter, M. Mikkelsen, J. Sherson, N. Zinner, and J. J. Arlt, Phys. Rev. Lett. **117**, 163201 (2016). 64

[101] R. A. W. Maier, M. Eisele, E. Tiemann, and C. Zimmermann, Phys. Rev. Lett. **115**, 043201 (2015). 64

[102] S. Knoop, F. Ferlaino, M. Mark, M. Berninger, H. Schobel, H. C. Nagerl, and R. Grimm, Nature Physics **5**, 227 (2009), ISSN 1745-2473. 66

[103] J. J. Krauth, M. Diepold, B. Franke, A. Antognini, F. Kottmann, and R. Pohl, Ann. Phys. **366**, 168 (2016), ISSN 0003-4916. 68, 69

[104] J.-W. Chen, G. Rupak, and M. J. Savage, Nuclear Physics A **653**, 386 (1999), ISSN 0375-9474. 68, 70, 75, 76, 80, 86

[105] S. Christlmeier and H. W. Griesshammer, Phys. Rev. **C77**, 064001 (2008). 68

[106] J.-W. Chen, G. Rupak, and M. J. Savage, Physics Letters B **464**, 1 (1999), ISSN 0370-2693. 68

[107] P. J. Mohr, B. N. Taylor, and D. B. Newell, Rev. Mod. Phys. **84**, 1527 (2012). 68

[108] P. J. Mohr, D. B. Newell, and B. N. Taylor, Rev. Mod. Phys. **88**, 035009 (2016). 68

[109] R. Pohl, F. Nez, L. M. P. Fernandes, F. D. Amaro, F. Biraben, J. M. R. Cardoso, D. S. Covita, A. Dax, S. Dhawan, M. Diepold, et al., Science **353**, 669 (2016), ISSN 0036-8075. 68

[110] J. Friar, Annals of Physics **122**, 151 (1979), ISSN 0003-4916. 69

[111] R. J. Hill and G. Paz, Phys. Rev. Lett. **107**, 160402 (2011). 69

[112] R. Pohl, Nature **466**, 213 (2010). 69

[113] E. Borie, Annals of Physics **327**, 733 (2012), ISSN 0003-4916. 69

[114] O. Hernandez, C. Ji, S. Bacca, N. N. Dinur, and N. Barnea, Physics Letters B **736**, 344 (2014), ISSN 0370-2693. 69, 70, 79, 87, 88, 89, 91, 92

[115] Y. Lu and R. Rosenfelder, Physics Letters B **319**, 7 (1993), ISSN 0370-2693. 70, 74, 79, 83, 87, 89

[116] F. Schmidt-Kaler, D. Leibfried, M. Weitz, and T. W. Hänsch, Phys. Rev. Lett. **70**, 2261 (1993). 70

[117] M. Weitz, A. Huber, F. Schmidt-Kaler, D. Leibfried, and T. W. Hänsch, Phys. Rev. Lett. **72**, 328 (1994). 70

[118] Y. Fukushima, M. Yahiro, and M. Kamimura, Phys. Rev. A **46**, 6894 (1992). 70

[119] V. A. Babenko and N. M. Petrov, Physics of Atomic Nuclei **66**, 1319 (2003). 80

[120] R. Rosenfelder, Annals of Physics **128**, 188 (1980), ISSN 0003-4916. 81, 82

[121] D. B. Kaplan, M. J. Savage, and M. B. Wise, Phys. Rev. **C59**, 617 (1999). 86

[122] C. Ji, N. Nevo Dinur, S. Bacca, and N. Barnea, Phys. Rev. Lett. **111**, 143402 (2013). 87, 88

[123] K. Pachucki, Phys. Rev. Lett. **106**, 193007 (2011). 88, 92

[124] N. N. Dinur, C. Ji, S. Bacca, and N. Barnea, Physics Letters B **755**, 380 (2016), ISSN 0370-2693. 88

[125] J. L. Friar and I. Sick, Phys. Rev. A **72**, 040502 (2005). 88

[126] K. Pachucki, Phys. Rev. A **60**, 3593 (1999). 88

[127] C. E. Carlson, M. Gorchtein, and M. Vanderhaeghen, Phys. Rev. A **89**, 022504 (2014). 91, 92

[128] R. Machleidt and D. Entem, Physics Reports **503**, 1 (2011), ISSN 0370-1573. 92

[129] E. Epelbaum, H.-W. Hammer, and U.-G. Meissner, Rev. Mod. Phys. **81**, 1773 (2009). 92

[130] E. Braaten, M. Kusunoki, and D. Zhang, Annals Phys. **323**, 1770 (2008). 106

[131] D. B. Kaplan, M. J. Savage, and M. B. Wise, Nucl. Phys. B **534**, 329 (1998). 111

[132] M. J. Savage, K. A. Scaldeferri, and M. B. Wise, Nuclear Physics A **652**, 273 (1999), ISSN 0375-9474. 112

Appendices

A Vertex Factors and Loop Integrals for the OPE

When calculating the two-body scattering amplitude in Ch. 2, one encounters the loop diagrams shown in Fig. 2.2 leading to the integrals labeled $\mathcal{I}_{2n}(E,\Lambda)$ given as

$$\begin{aligned}
\mathcal{I}_{2n}(E,\Lambda) &= \int_q \frac{i\boldsymbol{q}^{2n}}{q_0 - \frac{\boldsymbol{q}^2}{2m} + i\epsilon} \frac{i}{E - q_0 - \frac{\boldsymbol{q}^2}{2m} + i\epsilon} \\
&= -\frac{im\Lambda^{2n+1}}{2(2n+1)\pi^2} + mE\,\mathcal{I}_{2n-2}(E,\Lambda)\,, \qquad \text{(A.1)} \\
\mathcal{I}_0(E,\Lambda) &= -\frac{im}{2\pi^2}\left(\Lambda + \frac{\sqrt{mE}}{2}\left[i\pi + \ln\left(\tfrac{\Lambda-\sqrt{mE}}{\Lambda+\sqrt{mE}}\right)\right]\right) \\
&\approx -\frac{im}{2\pi^2}\Big(\Lambda + \frac{i\pi}{2}\sqrt{mE} - \frac{mE}{\Lambda} + \cdots\Big)\,, \qquad \text{(A.2)} \\
\mathcal{I}_2(E,\Lambda) &\approx -\frac{im}{2\pi^2}\Big(\frac{\Lambda^3}{3} + mE\Lambda + \frac{i\pi}{2}(mE)^{3/2} - \frac{(mE)^2}{\Lambda} + \cdots\Big)\,, \qquad \text{(A.3)}
\end{aligned}$$

where the integral symbol $\int_q = \int \frac{d^4q}{(2\pi)^4}$. The energy E is assumed to be greater than zero because the OPE matching is carried out above the two-body binding threshold . The result, which is valid above and below the threshold, is contained in Ref. [130]. Even powers of $\boldsymbol{q}$ arise in the numerator of $\mathcal{I}_{2n}(E,\Lambda)$ because of the attachment of part of the momentum-dependent, off-shell amplitude to a loop diagram.

One-body operator loop diagrams are also explained in this Appendix. Depending upon the operator at hand in a calculation, a different vertex factor in the loop integral must be used. Table A.1 contains the one-body vertex factors needed in this work. Each of these factors and each of the two-body-operator vertex factors may be derived by placing the definition of the nonrelativistic fermion field in the operators listed in Eq. (2.38) and taking any given spatial derivatives for a given operator.

Table A.1 – One-body Vertex Factors

Δ	3	4	5	6
$v_{1,\Delta}(\boldsymbol{p})$	1	$2ip_i$	$-4p_ip_j$	$-8ip_ip_jp_k$

Vertex factors for 1-body operators of $\Delta = 3..6$.

Table A.2 – Two-body Vertex Factors

Δ	4	5	6
$v_{2,\Delta}(p)$	$1/2$	$2ip_i$	$-4\delta_{ij}p_ip_j$

Vertex factors for two-body operators of dimensions $\Delta = 4..6$. For the total vertex factor, one must use $v_{2,\Delta}(q,l) = v_{2,\Delta}(q)+v_{2,\Delta}(l)$, where q and l are the vertex's ingoing and outgoing momentum, respectively. The δ_{ij} comes from the use of ∇^2 rather than $\partial_i\partial_j$ in $\mathcal{O}_{2,6}$.

The integral $\mathcal{I}_{2n}^{(1,\Delta)}$ containing the vertext factors of Table A.1 is from the last diagram in Fig. 2.6 and is given by

$$\begin{aligned}\mathcal{I}_{2n}^{(1,\Delta)}(E) &= \int_q \frac{i^2\boldsymbol{q}^{2n}\, v_{1,\Delta}(\boldsymbol{q})}{[E-q_0-\frac{\boldsymbol{q}^2}{2m}+i\epsilon]^2}\frac{i}{q_0-\frac{\boldsymbol{q}^2}{2m}+i\epsilon} \\ &= -i\frac{d}{dE}\left[\int_q \frac{i\boldsymbol{q}^{2n}\, v_{1,\Delta}(\boldsymbol{q})}{E-q_0-\frac{\boldsymbol{q}^2}{2m}+i\epsilon}\frac{i}{q_0-\frac{\boldsymbol{q}^2}{2m}+i\epsilon}\right]. \end{aligned} \tag{A.4}$$

The subscript $2n$ in $\mathcal{I}_{2n}^{(1,\Delta)}$ denotes the number of powers of $\boldsymbol{q}$ contained in the integrand's numerator due to the attachment of the off-shell amplitude. The superscript $(1,\Delta)$ indicates that the integral corresponds to the insertion of a one-body operator with dimension Δ into the relevant loop diagram. A couple of useful examples are obtained by inserting the vertex factors of Table A.1 into Eq. (A.4), and these are

$$\mathcal{I}_{2n}^{(1,3)}(E) = -i\frac{d\,\mathcal{I}_{2n}(E)}{dE}\,, \tag{A.5}$$

$$\mathcal{I}_{2n}^{(1,5)}(E) = i\frac{4\delta_{ij}}{3}\frac{d\,\mathcal{I}_{2n+2}(E)}{dE}\,, \tag{A.6}$$

where $\mathcal{I}_{2n}^{(1,\Delta)}(E) = 0$ for $\Delta = 4$, 6 since the integrand for those two dimensions is odd in $\boldsymbol{q}$. Through the use of $\mathcal{I}_{2n}$ written in Eq. (A.1), explicit expressions for the various $\mathcal{I}_{2n}^{(1,\Delta)}$ are obtained.

The integrals $\mathcal{I}_{2n}^{(2,\Delta)}$ for two-body operator insertions are useful in the diagrammatic calculations of Fig. 2.7. These are

$$\mathcal{I}_{2n}^{(2,\Delta)}(E) = \int_q \frac{i\boldsymbol{q}^{2n}\, v_{2,\Delta}(\boldsymbol{q})}{q_0-\frac{\boldsymbol{q}^2}{2m}+i\epsilon}\frac{i}{E-q_0-\frac{\boldsymbol{q}^2}{2m}+i\epsilon}\,. \tag{A.7}$$

Plugging in the vertex factors seen in Table A.2 into Eq. (A.7) gives the following results:

$$\mathcal{I}_{2n}^{(2,4)}(E) = \frac{\mathcal{I}_{2n}(E)}{2}\,, \tag{A.8}$$

$$\mathcal{I}_{2n}^{(2,6)}(E) = -\frac{4\delta_{ij}}{3}\mathcal{I}_{2n+2}(E)\,, \tag{A.9}$$

where the odd powers of $\Delta \geq 5$ don't contribute here for similar reasons as even dimensions did not contribute for one-body operators. The even loop-momentum powers in the integrals come once again from the attachment of the part of the off-shell amplitude with momentum-dependence to the loop diagrams. Further powers of momentum enter into the numerator of Eq. (A.7) from the inclusion of the vertex factors of Table A.2.

Some additional integrals which are needed for the nonlocal operator diagrammatic calculations composing the LHS of the momentum distribution are

$$\mathcal{I}_{\rho,2n}(E) = \int_q \frac{i^2 \boldsymbol{q}^{2n} e^{i\boldsymbol{q}\cdot\boldsymbol{r}}}{[q_0 - \frac{\boldsymbol{q}^2}{2m} + i\epsilon]^2} \frac{i}{E - q_0 - \frac{\boldsymbol{q}^2}{2m} + i\epsilon}\,, \tag{A.10}$$

$$\mathcal{I}_{\rho,0}(E) = -\frac{im^2}{8\pi\sqrt{mE}} e^{i\sqrt{mE}\,r} + O(1/\Lambda^3)\,,$$

$$\mathcal{I}_{\rho,2}(E) = -\frac{im^2[\sqrt{mE} - 2i/r]}{8\pi} e^{i\sqrt{mE}\,r} + O(1/\Lambda)\,.$$

B Phase Space Factors

In this work, we calculated the three-body recombination rate by relating it to the inelastic A_2D scattering cross section $\sigma_{A_2D}^{(\text{inelastic})}$ defined as

$$\sigma_{A_2D}^{(\text{inelastic})} = \frac{1}{2v_{A_2D}} \left|\mathcal{A}_{A_2D,A_1A_2A_2}\right|^2 \Phi_3 \,, \tag{B.1}$$

where $\mathcal{A}_{A_2D,A_1A_2A_2}$ denotes the amplitude for a transition from an A_2D state to three unbound atoms. The relative velocity of the atom A_2 relative to the diatomic molecule is given by $v_{A_2D} = k_E/\mu_{A_2D}$, where k_E is again $\sqrt{2\mu_{A_2D}(E+E_D)}$, and Φ_3 is the flux factor corresponding to the three-body phase space. We have included a symmetry factor of 2 in the total cross section expression of Eq. (B.1) because there are two identical particles in the final state.

The recombination rate can K_3 can then be written as

$$K_3 = \left|\mathcal{A}_{A_2D,A_1A_2A_2}\right| \Phi_2 = 2v_{A_2D}\frac{\Phi_2}{\Phi_3}\sigma_{A_2D}^{(\text{inelastic})} \,. \tag{B.2}$$

We then rewrite the inelastic cross section in terms of the total and elastic cross sections:

$$\begin{aligned}
\sigma_{A_2D}^{(\text{inelastic})} =& \sigma_{A_2D}^{(\text{tot})} - \sigma_{A_2D}^{(\text{elastic})} \,, \\
=& (2L+1)\left[\frac{2\mu_{A_2D}}{k_E}\text{Im}\mathcal{A}_L(k_E,k_E;E) - \left|\mathcal{A}_L(k_E,k_E;E)\right|^2\right] \,, \\
=& (2L+1)\frac{\pi}{k_E^2}\left[1 - \left|e^{2i\delta_{A_2D}^{(L)}(E)}\right|^2\right] \,,
\end{aligned} \tag{B.3}$$

where Eq. (3.2) was utilized in order to arrive at the final expression here for scattering in a particular partial wave of orbital angular momentum L. We have thus related the recombination rate to the phase shift (i.e. the S matrix element) of Eq. (3.16) up to a normalization factor determined by Φ_2/Φ_3.

The relevant two-body phase space factor Φ_2 is

$$\begin{aligned}\Phi_2 =& \int \frac{d^3p_A}{(2\pi)^3}\frac{d^3p_D}{(2\pi)^3}(2\pi)^3\delta^{(3)}(p_A+p_D)2\pi\delta\left(E-\frac{p_A^2}{2m_2}-\frac{p_D^2}{2(m_1+m_2)}+E_D\right),\\ =&\frac{\mu_{A_2D}k_E}{\pi}\,.\end{aligned} \tag{B.4}$$

The three-atom phase-space factor for the outgoing three-atom state is

$$\begin{aligned}\Phi_3 =& \int \prod_{i=1}^{3}\frac{d^3p_i}{(2\pi)^3}\delta^{(3)}(\mathbf{p}_1+\mathbf{p}_2+\mathbf{p}_3)2\pi\delta\left(E-\frac{p_1^2}{2m_1}-\frac{p_2^2}{2m_2}-\frac{p_3^2}{2m_2}\right),\\ =&\frac{(\mu\,\mu_{A_2D})^{3/2}}{8\pi^2}E^2\,,\end{aligned} \tag{B.5}$$

where the $\mathbf{p}_i$, with $i=1,2,3$, denote the momenta of each of the three final-state atoms. Combining these phase-space factors in Eq. (B.2) gives the final result

$$K_3^{(L)} = \frac{16\pi^2}{(\mu\,\mu_{A_2D})^{3/2}E^2}(2L+1)\left[1-|e^{2i\delta_{A_2D}^{(L)}}|^2\right]\,. \tag{B.6}$$

The substitution $E = x^2/2\mu a^2$ then leads to Eq. (3.16) in Ch. 3.

C Integrals with PDS

In this Appendix we compile the necessary loop integrals carried out using the *power divergence subtraction* (PDS) renormalization scheme for use in Ch. 4. This method for integral regularization, or the rendering finite of otherwise divergent integrals, and renormalization was first developed in Refs. [12, 131]. A loop integral with two propagators and $2n$ powers of loop momentum in the numerator of the integrand is written in this method as

$$\mathcal{I}_n = -i\left(\frac{\mu}{2}\right)^{4-D}\int\frac{d^Dq}{(2\pi)^D}\mathbf{q}^{2n}\frac{i}{E-q_0-\mathbf{q}^2/2M+i\epsilon}\frac{i}{q_0-\mathbf{q}^2/2M+i\epsilon}\,, \tag{C.1}$$

$$= -M(ME)^n(-ME-i\epsilon)^{\frac{D-3}{2}}\Gamma\left(\frac{3-D}{2}\right)\frac{(\mu/2)^{4-D}}{(4\pi)^{(D-1)/2}}\,, \tag{C.2}$$

where E is the ingoing two-body energy, and μ is the renormalization scale in the problem, such as the pion mass. The q_0 integral in Eq. (C.1) is performed with the usual complex contour technique. There is a pole at $q_0 = -\mathbf{q}^2/2m + i\epsilon$, and we carry out the integral using the formula

$$\oint f(z)dz = 2\pi i \times \frac{1}{(n-1)!}\lim_{z\to z_0}\left[\frac{\partial^{n-1}}{\partial z^{n-1}}\big((z-z_0)^n f(z)\big)\right], \tag{C.3}$$

where n gives the order of the complex pole. This integral result has a pole in dimension $D = 3$ which would be a linear divergence in a momentum-cutoff regularization scheme as detailed in App. A. In the PDS method, the pole is subtracted through the introduction of a counterterm labeled $\delta\mathcal{I}_n$. After adding the counterterm, the resulting set of integrals which we use in this work is

$$\mathcal{I}_n \to^{PDS}_{D\to 4} -(ME)^n\left(\frac{M}{4\pi}\right)\left(\mu-\sqrt{-ME-i\epsilon}\right)\,. \tag{C.4}$$

More generally for the $n = 0$ case, we may write

$$\begin{aligned}\mathcal{I}_0 \propto & \left(\frac{\mu}{2}\right)^{4-D} \int \frac{d^{(D-1)}q}{(2\pi)^{(D-1)}} \left(\frac{1}{\mathbf{q}^2 + a^2}\right) \\ =& (\sqrt{a^2})^{D-3} \Gamma\left(\frac{3-D}{2}\right) \frac{(\mu/2)^{4-D}}{(4\pi)^{(D-1)/2}}\,, \\ \to & \left(\frac{1}{4\pi}\right)(\mu - \sqrt{a^2})\,, \end{aligned} \tag{C.5}$$

where a counterterm was added following the PDS prescription to obtain Eq. (C.5) [132]. A similar equation may be derived for $n = 1$ in Eq. (C.1).

Vita

Samuel Emmons grew up in Illinois and Wisconsin. He attended the University of Wisconsin-Eau Claire (UWEC), where he obtained a Bachelor of Music degree in Piano Performance. At UWEC, he also majored in physics. It was in music school that he met his wife, Sarah Emmons. Sam and Sarah still enjoy performing music in a variety of venues. In 2010, Sam attended a conference near Knoxville, TN, and this sparked his interest in the University of Tennessee-Knoxville, where he obtained his Ph. D. in theoretical physics. Upon completion of his degree, he was hired to join the mathematics and physics department at Carson-Newman University in Jefferson City, TN, as an assistant professor of physics. Sam and Sarah enjoy living in, and being involved in, the community in Knoxville and the surrounding region.